DEVELOPMENT OF A NEAR-FIELD TERAHERTZ MICROSCOPE FOR BREAST CANCER DIAGNOSTICS

M. GRACE TRIMBOLI
Bachelor of Science, University of Lethbridge, 2012

A Thesis
Submitted to the School of Graduate Studies
of the University of Lethbridge
in Partial Fulfillment of the
Requirements for the Degree

MASTER OF SCIENCE

Department of Physics and Astronomy
University of Lethbridge
LETHBRIDGE, ALBERTA, CANADA

DEVELOPMENT OF A NEAR-FIELD TERAHERTZ MICROSCOPE FOR BREAST CANCER DIAGNOSTICS

M. GRACE TRIMBOLI

Date of Defence: April 28, 2015

Dr. David A. Naylor Supervisor	Professor	Ph.D.
Dr. Adriana Predoi-Cross Thesis Examination Committee Member	Professor	Ph.D.
Dr. Roy M. Golsteyn Thesis Examination Committee Member	Associate Professor	Ph.D.
Dr. Steve N. Patitsas Chair, Thesis Examination Committee	Associate Professor	Ph.D.

Dedication

To my family.

None of this would be possible

without you.

Abstract

Due to the sensitivity of teraHertz radiation to differentiating cancerous and healthy tissue, a teraHertz imaging microscope was developed for cancer diagnostics. The subject of this thesis is the design, assembly and verification of such a system. An optical knife-edge test was developed for beam profile determination at both optical and teraHertz frequencies. While waiting for the plasmonic lens to be fabricated an optical analogue imaging system was developed to evaluate the microscope design and software development. The design of the optical and teraHertz imaging systems included a two-axis translation stage with PSO option for sample translation and data collection during stage motion. Through analysis of THz images, verification of sub-wavelength resolution and sensitivity for differentiation of tissue types was determined. Imaging of cancerous samples was not possible at this time, the data presented are samples of rat brain tissue used to verify the system's capability for margin determination.

Acknowledgments

This project has been an extremely rewarding opportunity, during which I have been blessed to be mentored and encouraged by a great man. Through all the ups and downs, from illness to welcoming my baby boy into the world, Dr. David Naylor has been understanding and supportive, even while encouraging me to reach for the stars and never loose sight that anything is possible. I believe the motto 'It takes a family to raise a Grad student' is exemplified by the open and nurturing atmosphere which he fosters within the group. I will never be able to express my gratitude for all that he has done. Thank you!

I would like to thank my committee, Dr. Adriana Predoi-Cross and Dr. Roy Golstyen, for their unwavering support, words of encouragement and understanding throughout this project.

Thank you to Dr. Ken Vos for taking a chance and giving me the opportunity to work with him during my undergraduate degree. His encouragement and support for many years, all the times that he helped me with homework and lent a listening ear, have led me to where I am today.

Special thanks goes to our industrial partner, Blue Sky Spectroscopy Inc., for doing all the initial fabrication and design and allowing us to copy their design, use their software, and borrow components without reservation.

I have been privileged to, throughout most of my post secondary education, to work with my friend and college Tanner Heggie, who has always been there to talk to, explain concepts and encourage as we have learned together. Nowhere is this more significant than in the work that he has done to contribute to the contents of this thesis. Thank you.

This project would not have been possible without the involvement of many people:

Sudhakar Gunuganti, who accomplished much of the background work, the CAD design of the imaging system and most of the teraHertz imaging: Brad Gom, who was propound knowledge and background support made everything run more smoothly: Gregory Tompkins, who was always ready to help with wiring and hardware and always had an interesting (if controversial) topic to discuss: Geoff Minor, who was always willing to fabricate any pieces of hardware required to make this project possible and who was always happy to see me. Particular thanks goes to Dr. Jeff Dunn and Dr. Doug Demetric, and their staff, from the University of Calgary for their patience with all our delays and fast action in providing samples for imaging. Thanks to Ying Wu, from the Dunn Lab, for patiently teaching me how to section and mount samples.

This project has received support from the University of Lethbridge InSPIRE grant, the Natural Sciences and Engineering Research Council of Canada, and Alberta Innovates Technology Futures. In addition, the fabrication of the plasmonic lens was funded by a grant from CMC Microsystems, and particular thanks goes to Dr. Evgueni Bordatchev from NRC Automotive and Surface Transportation for taking such care with every lens milled for us.

As my family knows, this degree came with many obstacles to be overcome, most of which I could not have surmounted alone. My immense gratitude goes to my wonderful husband, Michael Trimboli, who knew when he married me that this was inevitable and has whole-heartedly supported me since. Thanks also goes to Frank and Heather Trimboli, Laura and Ron Couch, Angela and Jon Couch, Cathy Couch, Sabrina Couch, and Teresa and Dave Couch for their love, confidence and child care. All my family and friends deserve thanks for always lending a listening ear or a helping hand, and always believing in me.

I would also like to thank my aunt Barb Priestlay and my cousin Leanne Parnetta, whose battles with breast cancer have given me the drive and desire to go into this field of research.

Contents

List of Tables

List of Figures

Chapter 1

Introduction

Breast cancer is the most commonly diagnosed cancer in women throughout the world [10]. Over a million women are diagnosed, and nearly half a million die from the disease, each year [10]. Early detection and effective treatment are the best means of ensuring the survival of the patient and minimizing cost of care. The typical process of breast cancer screening begins with a mammogram. If cancer is suspected then the patient is referred for a biopsy, in which a small sample of the suspicious region is removed for further analysis. The excised biopsy sample is then typically examined by a pathologist using optical microscopy to determine the presence of cancer, as well as its type and severity.

If a diagnosis of breast cancer is given, breast conserving surgery or mastectomy, depending on the extent of the disease, may be recommended, with the former becoming most common [11]. During either procedure the surgeon removes all palpable (ie. what can be felt) tumour and a margin of healthy tissue to ensure that all cancerous tissue has been excised. Subsequently, the excised tissue is analysed to determine if the margin was sufficient to remove all cancerous tissue. If the surgeon was unsuccessful in removing all of the tumour a second surgery may be required causing additional risk and stress for the patient and cost for the hospital.

There are many possible means to improve this scenario, for example, mammography utilizes X-rays, which are high energy photons capable of inducing mutations. On the other hand, optical microscopy, which is non-ionizing, requires time consuming staining of samples before cellular features become discernible. Both techniques require a trained pro-

fessional to analyse the data and determine the presence and severity of the disease, which makes diagnosis dependent upon the skill of the technician or pathologist [11]. A recent editorial, March 17 2015, in The Journal of the American Medical Association reported on the dependence of correct diagnosis of breast cancer upon the expertise of the diagnosing pathologist [12]. In this editorial it was reported that the concordance of diagnosis of 115 pathologists was less than 50% for breast biopsy samples with atypia which represent approximately 10% of the diagnosed cancer cases. The diagnostic concordance for invasive cancer, ductal carcinoma in situ and benign lesions without atypia is 96%, 84% and 87%, respectively [12]. If a method of detecting cancer could be developed which did not require staining, was non-ionizing and could be automated so as not to necessitate interpretation, then it will represent a significant advance in the field. Recent measurements at teraHertz (THz) frequencies suggest that observations at these wavelengths may fulfil these requirements [6].

The region of the electromagnetic spectrum between microwave and infra-red has been called the THz 'gap' [13]. This title refers to the difficulty that exists in generating and detecting radiation in this frequency range. In general all imaging techniques consist of a source, a lens and a detector. It is only recently that THz sources and detectors have become available to investigate the properties of materials at these frequencies. Unfortunately for potential THz imaging applications the available sources are relatively weak and the detectors insensitive, also, lenses of the type required for microscopic imaging do not generally exist [14].

The interaction of THz radiation with tissues has been shown to be very sensitive to water, which has led to studies investigating its applicability in medical imaging techniques [15]. Due to its sensitivity to water, however, THz radiation has a small penetration depth into human tissues which precludes it use in non-invasive imaging techniques [15]. Chapter 3 discusses THz imaging in more detail. Studies have shown that THz radiation has a different absorption coefficient for cancerous tissue than healthy, which has been shown

for multiple types of cancer over a broad range of THz frequencies [6, 16–19]. Whereas the origin of this contrast remains unknown, THz imaging holds much promise for applications in medical diagnostics, which is the topic of my thesis.

By taking advantage of the significant difference in the absorption coefficients of cancerous and healthy breast tissue between 0.3 - 0.4 THz an imaging technique can be developed that can detect the presence of cancer in a sample [6]. There are still significant obstacles that must be overcome to bring THz imaging diagnostics to realization. The primary obstacle to THz imaging is spatial resolution. Lord Rayleigh's criterion states that the resolution obtainable for an imaging system is the order of the wavelength of the light used [20]. Thus, for the wavelength corresponding to the frequency range given above, the spatial resolution possible is around 900 μm, which is insufficient to resolve a cancer cell with a diameter of between 10-100 μm [21]. Spatial resolution can be improved by the addition of a sub-wavelength aperture that brings the attainable resolution to the order of the diameter of the aperture, rather than the wavelength of light used [22]. Unfortunately, transmission through a sub-wavelength aperture is very small, which has made increasing the resolution in this way difficult [23]. One method to increase the transmission through a sub-wavelength aperture is to use a plasmonic lens, discussed further in Chapters 3 and 4.

Recent reports of enhanced transmission through sub-wavelength structures, first discovered by Ebbesen *et al.*, in 1998, has led to the development of plasmonics lenses [24]. One type of plasmonic lens consists of a sub-wavelength aperture surrounded by surface structures that allow for the formation of surface plasmon polaritons [25]. Surface plasmon polaritons, when excited in phase, cause constructive interference leading to enhanced electric field a the aperture of the Bullseye plasmonic lens resulting in enhanced transmission through the aperture [1]. Further discussion of plasmonic lenses is found in Chapter 4.

By using a plasmonic lens designed for the correct THz frequency this imaging technique can be designed to be sensitive to different tissue types and have increased resolution which will make it more widely applicable. Chiu *et al.*, reported on a similar technique

which involved the use of a plasmonic lens to increase transmission and improve spatial resolution for breast cancer imaging [16]. Their initial apparatus required a substantial amount of time, approximately 3000 seconds, to acquire an image of a 1 cm x 1 cm area [16]. In subsequent articles by this group, they have reported that they acquired an image with the same dimensions in 60 seconds [26]. While this is a significant improvement, investigation into further improving and developing this technique is the subject of this thesis.

The work presented by Chiu *et al.*, in their 2009 and subsequent papers was taken as the starting point for the research presented in this work [16]. Our group has developed a THz imaging apparatus which has been optimized for imaging at 0.325 THz. A fast moving two-axis stage was acquired and mated with controllers which allow data acquisition while the stage is in motion. This allows an image of 1 cm x 1 cm area to be acquired in less than 20 seconds. Two versions of the imaging apparatus were created. The first was made to test the abilities of the two-axis stage, to acquire images taken with visible light and develop the software required for THz imaging. The final apparatus was designed specifically for THz imaging. These apparatti are described in greater detail in Chapters 6 and 8.

Chapter 2

Cancer Statistics

2.1 Introduction

Cancer is one of the most commonly diagnosed diseases in the world, affecting millions of new patients and their families each year [10]. In Canada, it is expected that 41% of women and 45% of men will develop cancer during their lifetimes [27]. For women, the most common cancer diagnosis is of breast cancer [10]. Early detection and judicious treatment are considered to be the best way to treat the disease and reduce morbidity. The gold standard in breast cancer detection is mammography, though other techniques can also be used in conjunction. After a positive mammogram, a biopsy sample is required to confirm the diagnosis using optical microscopy. If cancer is confirmed, and sufficiently progressed, breast conserving surgery or mastectomy may be required to prevent loss of life and speed the healing process. Samples taken through biopsy or during surgery must be sectioned, prepared and examined with optical microscopy [28]. Staining of the sample is required before cellular features are visible in the optical microscopy technique that will allow for cancer diagnosis. The speed and imaging requirements dictate the type of sectioning and stains that will be used for sample preparation. This Chapter will discuss the incidence of breast cancer, the different techniques used in detection and diagnosis, sample retrieval and preparation and the possibility of misdiagnosis.

2.2 Cancer Statistics

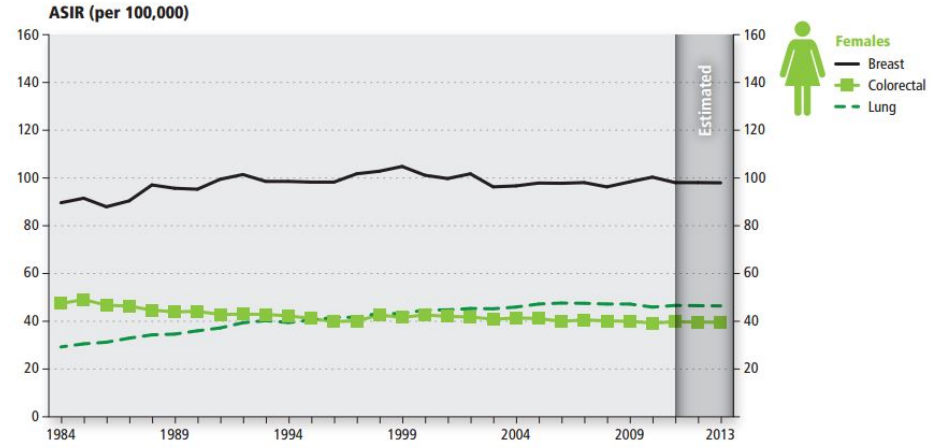

(a)

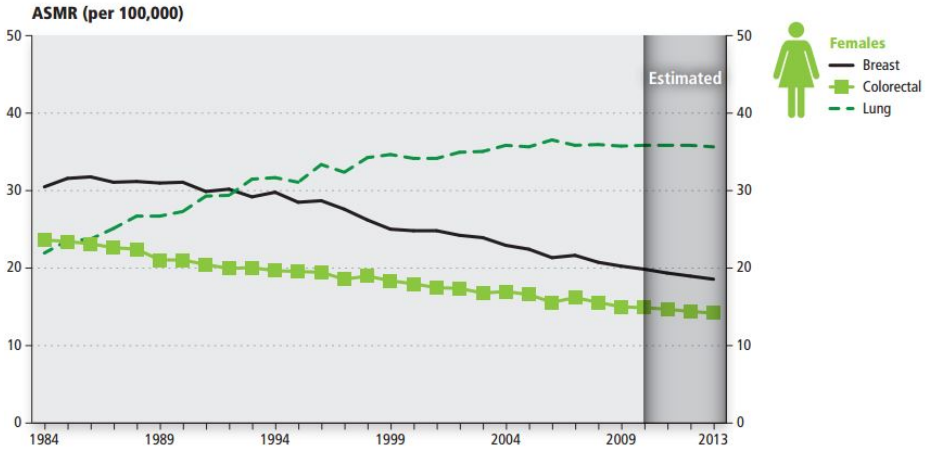

(b)

Figure 2.1: (a) Incidence rate of breast cancer, colorectal cancer, and lung cancer in Canada over the last 3 decades [3]. (b) Death rate of breast cancer, colorectal cancer, and lung cancer in Canada over the last 3 decades [3].

Breast cancer is the most commonly diagnosed cancer among women throughout the world with an estimated 1.67 million new breast cancer cases diagnosed in 2012 [10]. After lung cancer, breast cancer is the most common cause of cancer death in women, claiming an estimated 198,000 lives in 2012, worldwide [10]. In Canada, breast cancer is also the most commonly diagnosed cancer for women with 24,600 new cases in 2014 [3]. One in

nine Canadian women will develop breast cancer in their life time and one in twenty-nine will die as a result of the disease [3]. In 2014, 5,000 women died from breast cancer in Canada [3]. These statistics show that there is an average of 65 women diagnosed with breast cancer and 14 women die due to the disease each day in Canada [3].

As Figure 2.1 shows, while the incidence rate of breast cancer diagnosis has remained relatively constant, the incidence of deaths in Canada due to breast cancer has dropped significantly [3]. This change can be attributed to improvements in screening techniques and treatment regimens.

2.3 Common Breast Cancer Detection Techniques

Early detection and effective screening techniques have contributed to the decrease in deaths due to breast cancer in Canada over the last 30 years, see Figure 2.1. Breast cancer screening is first done using non-invasive techniques, such as mammography or ultrasound [28]. Diagnosis is then confirmed by using optical microscopy on samples taken by biopsy or during surgery.

2.3.1 Non-invasive Techniques

Mammography

First approved for use in the USA in 1969, mammography is considered to be the gold standard for breast cancer detection, although it employs X-rays for imaging, which are high energy and thus can cause ionization in tissues [11]. The Canadian Cancer Society recommends that all women between the age of 50 and 69 have a mammogram every two years [29]. Conventional mammography is conducted by compressing the breast in between two plates in order to make the breast as flat as possible [11]. X-ray images are taken of the flattened breast from different angles from center to side [11]. Due to the short wavelength of the X-rays used to take the images, the radiation can travel unimpeded through the soft tissue of the breast and be detected at the imaging plate [11]. Denser tissue in the breast

cause the X-rays to scatter in other directions or be absorbed by the tissue itself [11]. The absorption and scattering effects of X-rays by dense tissues in their path cause these areas to be seen as white regions in a mammography image, while less dense tissues appear dark, or black, in the image [11]. Figure 2.2 shows three different mammography images. The left image is an image of a normal breast, the middle image is a breast with a benign cyst and the right is an image of a breast with a malignant tumour.

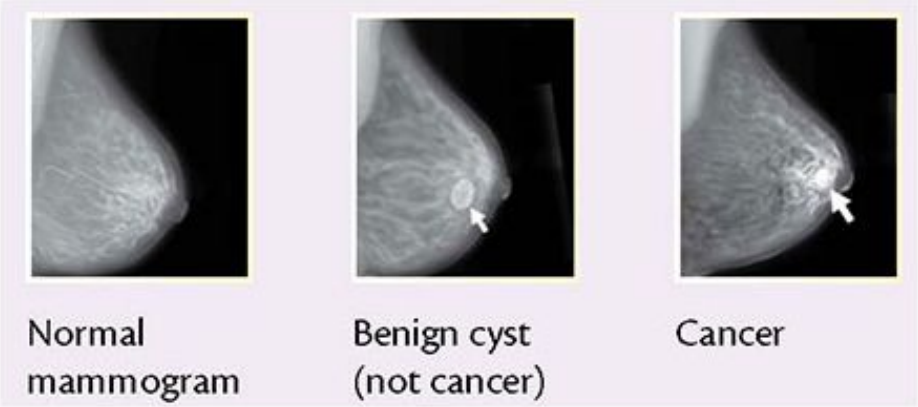

Figure 2.2: Comparison of mammographic images of a normal breast, a breast with a benign cyst, and a breast with a cancerous lesion [4].

Several factors impact the effectiveness of mammography for breast cancer detection. Some of these include: the age of the patient, the general density of the breast tissue being imaged, the quality of the image taken, and the experience of the radiologist performing the test [11]. Frequent screening can be used as a tool to mitigate the impact of some of these factors and allow for greater sensitivity and specificity results for the patient [11]. For example, yearly screening can result in mammography sensitivity of 71 - 96% and specificity of 94 - 97% [11]. This allows the radiologist to compare images from the current test with previous ones to identify changes [11]

Sonography

Sonography, otherwise referred to as ultrasound, is an imaging technique that is often used in conjunction with mammography to confirm the presence of cancer in a patient [11]. Ultrasound uses high frequency sound waves reflecting off tissues and structures inside of the body to create an image [11]. Unlike mammography, sonography does not use any harmful radiation in the process of image acquisition and is, therefore, considered safe to use when a mammogram may not be, such as when the patient is pregnant. This technique, is not used for routine breast cancer screening because it is not able to identify certain early signs of breast cancer [11].

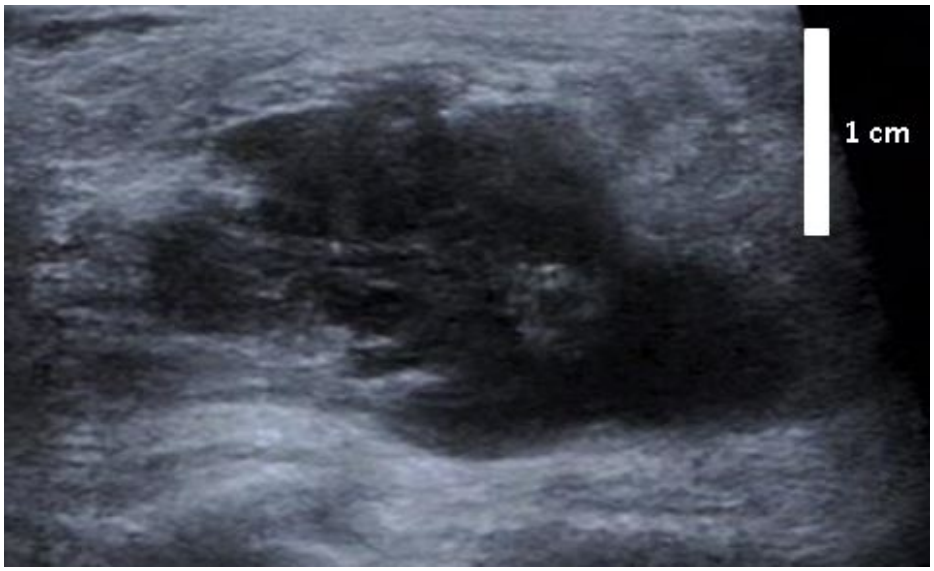

Figure 2.3: Sonography image of a malignant mass in the left breast [5].

2.4 Tissue Extraction and Optical Microscopy

To obtain a diagnosis of breast cancer a tissue sample must be examined. There are two main ways in which a sample of the relevant tissue can be obtained: biopsy and surgery [28]. Biopsy is the method most commonly used, with two main techniques depending on the size of sample needed. Samples are also taken during a surgical procedure to allow for post procedural margin confirmation (checking that the surgery removed all cancerous tissue

along with a safe margin of healthy tissue). This thesis only deals with tissues obtained during biopsy.

2.4.1 Biopsy

Fine-needle aspiration biopsy involves the use of a very fine needle to draw a small amount of tissue out of a region of interest in a patient for further analysis [30]. Core-needle biopsy involves a much larger needle which is hollow and equipped with a cutting mechanism so that a core of tissue from the suspicious region can be obtained [31]. In general multiple samples are taken with either procedure to ensure proper diagnosis. Both of these techniques are often accomplished while guided by ultrasound imaging to ensure that the correct area is probed.

2.4.2 Surgery

Tissue samples can also be obtained via surgical means. If the patient has already been diagnosed with breast cancer and breast conserving surgery or mastectomy is recommended then the tissue that is taken during surgery will require analysis to determine if the procedure was successful [28]. This is part of verifying if the margin taken by the surgeon was sufficient to remove all cancerous tissue.

2.4.3 Optical Microscopy

In optical microscopy, a previously obtained sample is embedded or frozen, sectioned, mounted on a slide, stained and examined through an optical microscope. A pathologist then determines if cancer is present in the sample and its type. This technique has excellent resolution and requires inexpensive equipment, however, it is time consuming due to the steps required to prepare the sample for analysis, and diagnosis may depend upon the expertise of the pathologist [12, 32]. Taking into account the time required to prepare the sample for sectioning and staining and then the time for examination, results from this technique can take from hours to several days to acquire [32, 33]. Staining is required since

the cellular features that allow for determination of the presence and type of cancer are not differentiable without them [32]. Also, like mammograms, optical microscopy is subject to the skill of the pathologists making the determination, which varies according to their experience, speciality and education.

2.5 Sample Preparation

Once a sample is taken, whether during a biopsy or surgery the sample must be prepared and mounted for imaging. There are three types of preparation that can be used depending on what the sample is needed for once it is prepared. These preparation techniques are: frozen, paraffin embedded and resin embedded [32]. Frozen and paraffin embedded will be discussed below. Resin embedded is only used when the sample either needs to be preserved indefinitely or must be incredibly rigid for the mounting process. Frozen or paraffin embedded samples are most common. After the sample is prepared either by the frozen section or the paraffin embedding method it must be stained with the proper contrast solutions before examination using optical microscopy [32].

2.5.1 Frozen Section

Frozen sectioning is the fastest and easiest way to prepare a sample, though it can cause damage to the cells if done incorrectly. Tissue taken must be preserved by freezing, generally done using a cryo-preservative solution of liquid nitrogen, as soon as possible after removal to limit protein degradation [32]. Frozen section tissue can be cut to a thickness of between 2 - 15 mm, though 5 - 8 mm is optimal [32]. These samples must be stored at -80^{o}C to preserve the sample.

2.5.2 Paraffin Embedding

Paraffin embedding first requires that all the water in the tissue be replaced by paraffin before it is embedded inside a block of paraffin wax. Through a process of immersing the sample in alcohol, to dehydrate the tissue, xylene, to clear the sample, and paraffin, the

sample is infiltrated with paraffin wax. The full method for paraffin embedding can be found in [34]. Paraffin embedded samples can be sliced as thin as 4 μm and as thick as the sectioning machine will allow, though it is more common for the samples to be sliced 7 - 8 μm thick and can be cut reliably as high as 20 μm [35]. This process takes a minimum of several hours, though typically it is accomplished over a day or two, compared with frozen sectioning which is typically done in minutes [32]

2.5.3 Staining

All samples must be stained before they can be examined by a pathologist using optical microscopy. There are many different stains that can be used, but hematoxylin and eosin (H & E) is generally used in preparation for cancer detection [32]. H & E staining is a multi-step process which involves the use of hematoxylin to stain the nucleus and cytoplasmic RNA dark blue or purple and eosin to stain the proteins a bright orange-pink [36]. Staining a single sample takes a minimum of 75 mins [37].

2.6 Incorrect Diagnosis

Most women are aware that breast cancer screening comes with some inherent risks [38]. In addition to the potentially harmful effects of X-rays on human tissue and the risk of infection after biopsy, there is also the chance of an incorrect test result [38]. These incorrect results fall into one of three categories, falsely reporting the presence or absence of cancer when the opposite is actually true and incorrectly diagnosing the type or severity of the disease. False diagnosis of the presence or absence of cancer is known as a false positive or negative result, while a diagnosis of the wrong type of cancer is known as a misdiagnosis [12, 38].

False Negative

A false negative test result is one that says that the individual does not have cancer when the disease is actually present [38]. The result being that other tests are thought to be unnec-

essary and the would be patient goes home free of concerns. As a result of the false negative the woman may decide to forego further investigation even if symptoms start to appear. The cancer remains, however, and when it is discovered the patient's chances of survival have severely fallen because the delay in detection and treatment of the disease [39]. Many factors, including higher density breast tissue, size of the tumour, and skill of the radiologist, can influence a woman's likelihood of receiving a false positive test result [11, 40].

False Positive

Unlike a false negative, a false positive result brings the women back for additional tests that are unnecessary. Approximately 10% of mammography results are incorrect and 90% of those are false positives [11]. False positive results are also influenced by the density of breast tissue, the size of the tumour and the skill of the radiologist [11, 40]. This means that 1 out of every 10 scans can give a false positive result [11].

Misdiagnosis

Misdiagnosis is, perhaps, the most concerning since this diagnosis comes after having additional testing to confirm the original positive mammogram result. The rates of misdiagnosis has been understudied, which means that the dependence of diagnosis on expertise and training is not well understood [12]. In a recent editorial in the Journal of the American Medical Association, a study of the discordance of cancer diagnosis was discussed. This study was two staged, including 3 expert breast pathologists which analysed and diagnosed 240 breast samples independently and 115 pathologists, chosen as a representative sub-set of the population of pathologists in 8 US states, which analysed and diagnosed a subset of 60 samples [12]. It was found that the overall concordance of diagnosis for different types of samples was 96% for invasive cancer, 87% for benign lesions without atypia, 84% for ductal carcinoma in situ and 48% for atypia, see [12] for the full discussion. These results show that, for cancers which exhibit atypia ($\sim$10% of cases), the diagnosis is as accurate as the flip of a coin [12].

Development of an imaging system which exploits tissue properties to differentiate between cancerous and healthy tissues, regardless of expression of atypical features, removing the dependence of diagnosis upon the skill of the pathologist has the potential for significantly decreasing the incidence of misdiagnosed cancers.

Chapter 3

TeraHertz Imaging

3.1 Introduction

The impetus for developing a THz imaging system has been presented in Chapter 1. Correct diagnosis and complete removal of cancerous tissue during surgery is expected to result in both longer life expectancy and lower health care costs [11]. THz imaging offers several advantages over other imaging techniques; it is none ionizing, it is sensitive to cancerous tissues and does not require the sample to be stained [14]. THz imaging, however, generally has poor spatial resolution, due to its longer wavelength, and so requires a sub-wavelength imaging technique to improve spatial resolution.

3.2 TeraHertz Radiation

Exploring the electromagnetic spectrum broadly breaks down into two experimental techniques, one in which the radiation ($\sim$10 THz and above) is generated by optical methods and the other where radiation ($\sim$100 GHz and below) is generated by electronic methods [14]. Between these regions of the electromagnetic spectrum, about 0.1 - 10 THz, is the 'THz gap', a region where neither method can easily produce radiation [13]. Since THz radiation is so difficult to generate, sources are relatively weak and are not mass produced which makes them expensive.

THz radiation is low energy, which makes it a safer imaging frequency than X-rays, although this becomes less of a concern when not applied to human *in vivo* imaging. Also, THz radiation has been shown to be sensitive to cancerous tissues and is readily absorbed

by water [6]. Due to both of these factors, THz imaging for medical applications is an open field of study. It is this absorption by water which results in its penetration depth in human tissues of only a few millimetres, unlike X-rays which can pass through tissues unimpeded (ignoring scattering) [15].

Since the THz region is thought of as between 0.1 and 10 THz, it corresponds to wavelengths of between 0.3 cm - 30 μm [13]. These long wavelengths limit the potential spatial resolution of THz imaging [20]. The use of a sub-wavelength aperture to allow for sub-wavelength spatial resolution is required for THz imaging to become a useful cancer diagnostic technique [41].

3.3 TeraHertz Imaging

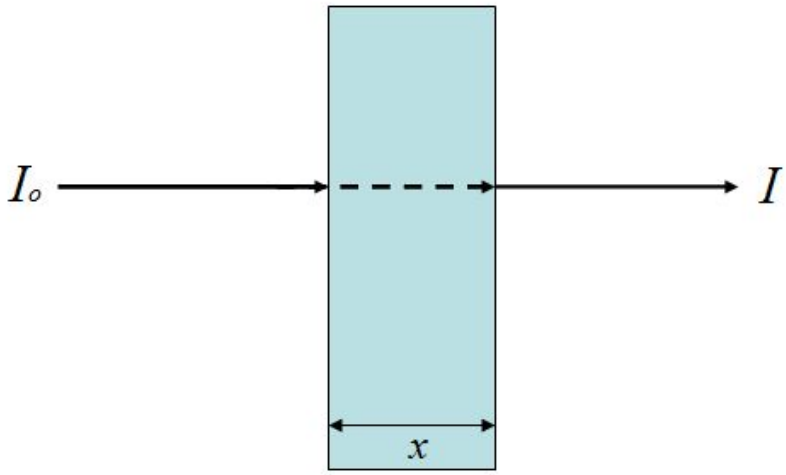

Figure 3.1: Illustration of the Beer-Lambert Law

When neglecting losses due to reflections at the interface, teraHertz imaging can be described by the application of the Beer-Lambert law

$$I = I_0 e^{-\alpha x} \tag{3.1}$$

where I_0 is the incident intensity, I is the final intensity, x is the thickness of the sample and α is the absorption coefficient [20]. Sample thickness and the absorption coefficient of the tissue determine the final intensity of the radiation transmitted through the material. The absorption coefficient defines the distance into the material that radiation can penetrate before its intensity falls to $1/e$ times its original intensity. This is an inherent property of the material and depends upon the wavelength of the light. For example, consider two different materials with absorption coefficients, α_1 =9 mm^{-1} and α_2 =11.3 mm^{-1}, and let there be two pieces of each with thickness of 10 and 30 μm [6]. These values were chosen because they are representative of healthy and cancerous tissue, as will be shown in Figure 3.2. The change of intensity between the samples, when thickness is held constant, can be written as

$$\frac{\Delta I_{10}}{I_0} = \frac{I_1 - I_2}{I_0} = e^{-\alpha_1 x_{10}} - e^{-\alpha_2 x_{10}} \tag{3.2}$$

or

$$\frac{\Delta I_{30}}{I_0} = \frac{I_1 - I_2}{I_0} = e^{-\alpha_1 x_{30}} - e^{-\alpha_2 x_{30}} \tag{3.3}$$

which, for our example, gives

$$\frac{\Delta I_{10}}{I_0} = e^{-9(mm^{-1})10(\mu m)} - e^{-11.3(mm^{-1})10(\mu m)} = 0.021 \tag{3.4}$$

or

$$\frac{\Delta I_{30}}{I_0} = e^{-9(mm^{-1})30(\mu m)} - e^{-11.3(mm^{-1})30(\mu m)} = 0.051 \tag{3.5}$$

When holding the absorption coefficient constant, we can find the change in intensity for different material thickness.

$$\frac{\Delta I_1}{I_0} = \frac{I_{10} - I_{30}}{I_0} = e^{-\alpha_1 x_{10}} - e^{-\alpha_1 x_{30}} = e^{-9(mm^{-1})10(\mu m)} - e^{-9(mm^{-1})30(\mu m)} = 0.151 \tag{3.6}$$

or

$$\frac{\Delta I_2}{I_0} = \frac{I_{10} - I_{30}}{I_0} = e^{-\alpha_2 x_{10}} - e^{-\alpha_2 x_{30}} = e^{-11.3(mm^{-1})10(\mu m)} - e^{-11.3(mm^{-1})30(\mu m)} = 0.181 \tag{3.7}$$

This example shows how both the absorption coefficient and the thickness of the material affect the final intensity of the radiation collected during THz transmission imaging as defined by equation 3.1. It naturally follows that greater sensitivity in α can be achieved by imaging through a thicker sample.

In tissue imaging, however, there is a maximum sample thickness possible based on the tissue preparation technique used, as is discussed in Section 2.5 [32, 35]. These restrictions lead to a need for sufficiently sensitive detectors to differentiate one tissue type compared with another. For cancer imaging, the required sensitivity is shown in Figure 3.3. Since the absorption coefficient is the main factor which allows for THz imaging, using a method that takes advantage of the greatest difference between absorption coefficients of tissues allows for greater difference in the relative signals.

3.4 TeraHertz and Cancer

THz radiation has been found to be particularly sensitive to the presence of cancerous tissue, though the origin of this contrast is not well understood. Cancer detection with THz imaging has successfully been accomplished for skin, breast, liver and colo-rectal cancers [6,16–19]. Ashworth *et al.*, reported that the absorption coefficients of fatty, fibrous (healthy) and cancerous breast tissues was found to be the greatest in the range of 0.15 to 0.6 THz, these were found to be 2.5-5.2 mm^{-1}, 6.8-12.3 mm^{-1} and 7.9-15.2 mm^{-1} respectively [6].

3.4.1 Water and Other Sources of Contrast

THz radiation is sensitive to the presence of cancer in a sample, as can be seen from the difference in their absorption coefficients. The source of this contrast has been attributed,

by some authors, to the increased presence of water in cancerous tissue [42, 43]. Further investigation of paraffin embedded tissue samples has also revealed other potential contributors to this difference [19].

Cancerous tissue has been shown to have higher concentrations of water in NMR studies [42]. Since water has a rotational mode close to the THz range, it has been thought that the higher concentration of water is the cause of the higher absorption coefficient attributed to cancerous breast tissue [43]. THz radiation also excited the vibrational modes in the weak bonds between water molecules, lending more credence to this explanation [44]. The effects of water on the contrast between healthy and cancerous tissue can be further studied by examining frozen sectioned samples, see Section 2.5, where the water remains in the sample during imaging.

On the other hand, as discussed in Section 2.5, paraffin embedding removes the water content of the tissue and replaces it with paraffin wax [34]. The continued differential between tumour and healthy tissue after paraffin embedding shows that water alone cannot be the only source of contrast for THz imaging [19]. According to Wahaia *et al.*,, some possible sources of contrast are increased vasculature, low oxygen, pH, glucose and lipid levels in the tumour (alone or in combination), increased cell density, and the presence of certain proteins [45]. Investigation into these and other contrast sources is an open field of study.

3.5 Imaging Techniques

THz imaging is separated into time-domain or frequency-domain techniques. Time-domain techniques include both time-domain spectroscopy and imaging, which can provide broad-band information about the material under study [14]. Frequency-domain imaging is less commonly used and provides frequency specific information, which can take advantage of specific properties of the material for its imaging [46]. Due to its inherent lower spatial resolution, frequency-domain imaging is generally performed in the near-field, which will

be discussed further in Section 3.5.2.

3.5.1 Time-Domain Imaging

THz imaging in the time-domain is separated into two types: THz time-domain spectroscopy (THz-TDS) and THz pulsed imaging (THz-TPI) [14]. Both explore low-frequency torsional and vibrational motions of molecular systems, though they generate different information [13]. THz-TDS can generate information about both the absorption coefficient and refractive index of the material [47]. THz-TPI generates far-field images through analysis of information collected by THz-TDS means over a spatial area.

THz-TDS uses a THz emitter, usually a femto-second laser, which triggers an ultrafast change in the polarization of a non-linear material, e.g. zinc telluride, resulting in the generation of THz radiation [47]. Since the pulses emitted from the laser must be under 100 fs, the resulting THz radiation is broadband, e.g. 0.1-5 THz for some systems [47]. The THz detector used for this type of imaging is sensitive to the electric field which allows for both phase and amplitude information to be obtained, enabling the absorption coefficient and refractive index of the material to be determined [47]. A THz-TDS review is found elsewhere [48].

3.5.2 Frequency-Domain Imaging

Frequency-domain imaging is a technique based upon absorption spectroscopy. This allows frequency specific properties of tissue samples to be used as part of the imaging technique. Since THz radiation corresponds to wavelengths several orders of magnitude longer than optical or X-ray radiation, THz frequency-domain imaging has been difficult to develop with sufficient spatial resolution to be useful in cancer detection [16]. The introduction of a sub-wavelength aperture can increase the resolution to the order of the diameter of the aperture and brings the technique into the 'near-field'.

Frequency Choice

Since frequency-domain imaging can take advantage of frequency specific properties of different tissues, it is important to choose the optimal frequency for imaging. Figure 3.2 shows Ashworth *et al.*'s results from 2007 [6, 15, 49].

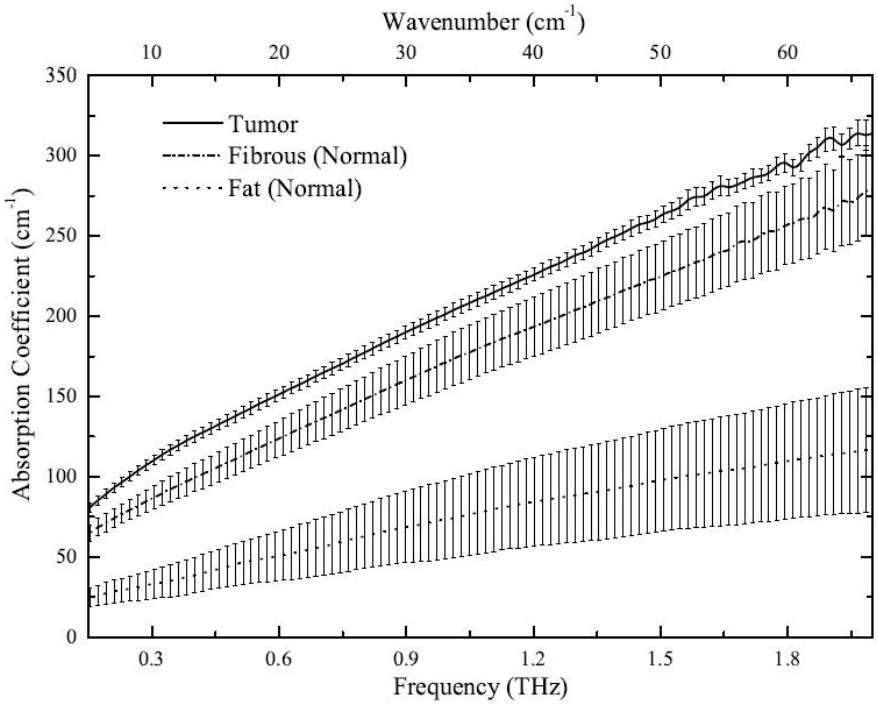

Figure 3.2: Absorption coefficient of fatty breast tissue, fibrous breast tissue and breast tumour over the range 0.15 - 2 THz. [6]

For our research we used a THz source with a frequency range between 0.32 - 0.33 THz, which limited our frequency choice to within this range. We chose to image at a frequency of 0.325 THz, which corresponds to absorption coefficients of approximately 2.34 - 4.11 mm^{-1} for fatty tissue, 7.8 - 9.15 mm^{-1} for fibrous (normal) breast tissue and 10.4 - 11.5 mm^{-1} for cancerous breast tissue [6, 49]. Figure 3.3 shows how the observed intensity changes depending on the type of tissue being imaged.

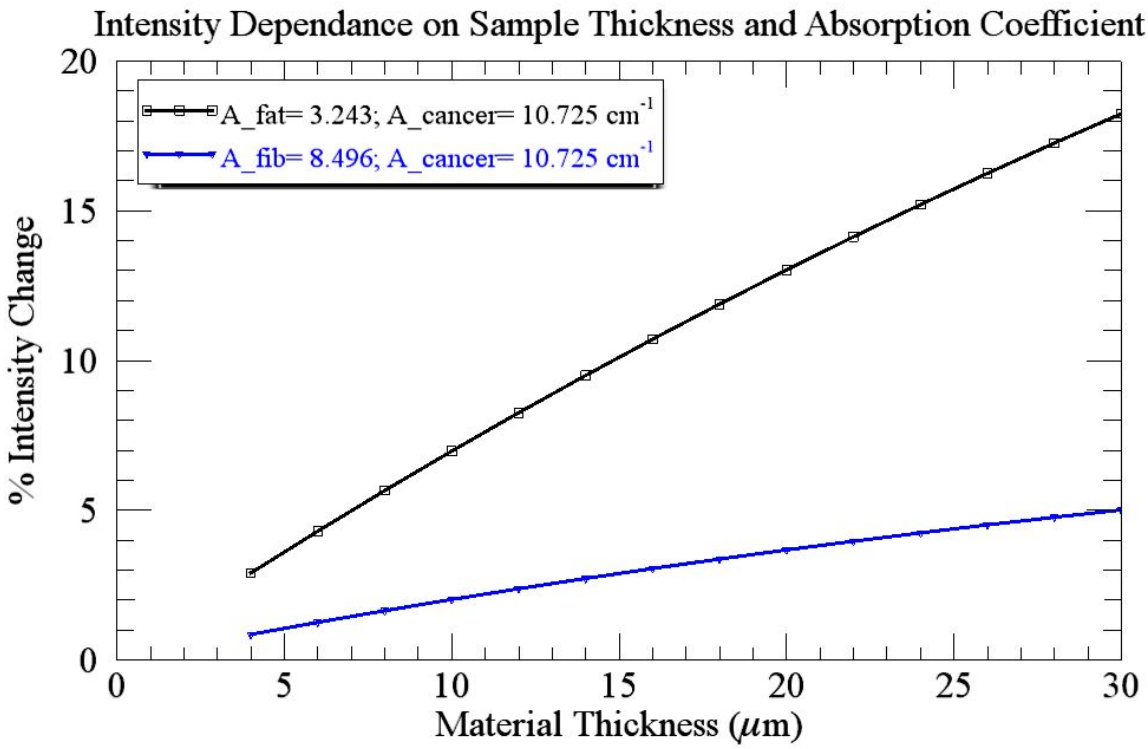

Figure 3.3: The percent change in intensity, according to $e^{-\alpha_1 x_s} - e^{-\alpha_2 x_s}$ where x_s is the sample thickness and α_1 and α_2 are the absorption coefficients of fatty and cancerous (top line) or fibrous and cancerous (bottom line) tissue. Each line shows how the imaging specificity of the system is dependent on both the different tissues being imaged and the thickness of the sample.

Resolution

There is one significant drawback to using a frequency-domain approach to THz imaging. While the long wavelength of THz radiation reduces the scatter off biological tissues, diffraction effect cause the resolution of the image to be impacted [13]. Classically, the best resolution possible is that of the wavelength of the radiation used to image [20]. This means that the best resolution that is possible while imaging with 0.325 THz is $\sim$ 1 mm. Since human cells are between 10 - 100 μm, which is 10 - 100 times smaller than the wavelength of 0.3 THz radiation, effective THz imaging of human tissue with a single frequency will

require a means of improving the spatial resolution [21]. One way to increase the resolution is to use a sub-wavelength aperture such that the resolution becomes a function of the radius of the aperture rather than of the wavelength of the light.

Using Plasmonic Lenses

Although using a sub-wavelength aperture can improve the spatial resolution for THz imaging, the intensity of the radiation is reduced significantly, making imaging very difficult. According to Bethe, the power, related to the intensity, of the radiation through a sub-wavelength aperture is proportional to r^6/λ^4 where λ is the wavelength and r is the radius of the aperture [23]. In 1998, Ebbesen *et al.* reported on extraordinary transmission of visible light through sub-wavelength hole arrays, which has lead to rapid growth in the field of plasmonics, in which manipulation of surface plasmon polaritions can lead to enhanced transmission that is independent of wavelength [24]. Structures that allow these surface plasmon polaritons to form and propagate and provide a means of enhancing transmission and improve spatial resolution are known as plasmonic lenses. This subject will be discussed more fully in Chapter 4.

Previous Results

In 2009, Chiu *et al.* reported on their work using THz near-field imaging to image breast cancer samples [16]. Their apparatus also used a plasmonic lens to increase spatial resolution tuned to a frequency of 0.312 THz. In this and subsequent articles, this group has reported a 100% specificity rate in their imaging trials [16,26,46,50]. In addition to imaging human breast cancer samples *ex vivo*, they were able to image breast cancer tissue when grown under the skin of laboratory mice [46], successfully image cancerous liver [51] and, most recently, colon tissues [52]. This experiment showed the potential of THz imaging to detect the presence of cancer earlier in it development than other imaging techniques, showing the potential of THz near-field imaging in margin determination [46].

3.5.3 Slide Material Considerations

Typically, tissue samples are mounted on glass slides approximately 75 mm long, 25 mm wide and 1 mm thick. Although most glass is transparent in the visible, they are not necessarily transparent at THz frequencies. For THz frequencies, standard glass microscope slides and cover-slips have an absorption coefficient in the range 0.6 - 0.9 mm^{-1}, which contributes an additional loss of intensity [53]. Other materials, such as quartz and particular plastics, have low absorption coefficients in the THz range, but are not as easily used (lacking required long-range flatness) for sample mounting [54].

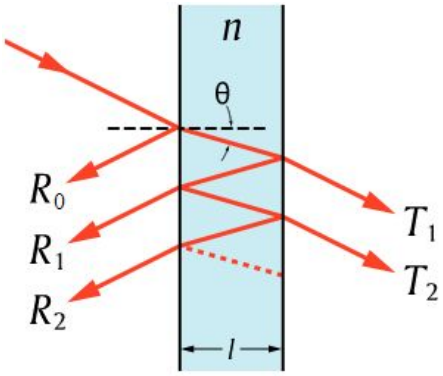

Figure 3.4: Example of multiple reflections

The absorption of the glass is not the only drawback to using a standard slide for sample mounting. Reflections which occur at the surface of the slide due to difference in refractive indices of the materials can become a problem when the optical thickness of the slide is an integer multiple of the half wavelength ($\lambda/2$) [20]. Since $\sim$ 0.325 THz corresponds to $\sim$ 1 mm, the slide's thickness can allow for interference effects when multiple reflections are present, see Figure 3.4. One way to eliminate this obstacle is to mount the sample on a thinner substrate, *ie.* a microscope cover-slip ($\sim$150 μm thick). By using a thin substrate as provided by a cover-slip, the effect of interference fringes can be minimized.

Chapter 4

Plasmonics

4.1 Introduction

In optics, one of the key specifications of any imaging system is spatial resolution which is proportional to the wavelength of the light used and inversely proportional to the limiting aperture [20]. Human cells, including cancerous cells, are typically 10 - 100 μm in diameter [21]. Developing an imaging technique to detect this scale of size is trivial in the visible where the wavelength is a fraction of the required spatial resolution. This becomes increasingly important as the wavelength increases. THz radiation has a wavelength of 0.3 - 30 mm, corresponding to 0.1 - 10 THz, which results in a spatial resolution that is 10 - 100 times worse than required for single cell detection [13, 21].

As explained in Chapter 3, THz radiation is sensitive to the presence of cancerous tissue due to the difference in the absorption coefficients of fatty, healthy and cancerous tissues [6]. In order to utilize the significant difference between the absorption coefficients of healthy and cancerous tissues seen around 0.325 THz ($\lambda \sim 1$ mm) a method for increasing the spatial resolution is required [49]. While resolving single cells in the THz is challenging, our goal is to provide sufficient spatial resolution for margin determination. To improve the spatial resolution, near-field imaging using a sub-wavelength aperture is performed [22]. In this configuration, the spatial resolution becomes a function of the aperture size rather than the wavelength [22]. Use of a sub-wavelength aperture, however, results in a significant decrease in transmitted radiation [22]. According to Bethe, the transmitted power is proportional to r^6/λ^4, where r is the radius of the aperture and λ is the wavelength

of light [23]. Since THz sources are relatively weak, and detectors insensitive, this poses a substantial obstacle for THz imaging applications [14]. For a THz imaging technique to be effective for cancer diagnostics increased transmission through a sub-wavelength aperture is necessary. This requirement has led to active research into methods of increasing the transmission.

In 1998, Ebbesen *et al.*, reported on extraordinary transmission of visible light through a sub-wavelength hole array [24]. This extraordinary transmission was achieved by coupling light with electrons near the surface of a metal-dielectric interface in order to form surface plasmon polariton waves (SPPs). These SPPs provide a mechanism for greater transmission efficiency through a sub-wavelength aperture, which becomes increasingly important at longer wavelengths. The field of plasmonics is currently a very active area of research, whose goal is to create geometrical designs which enhance the transmission of light through sub-wavelength apertures [41, 55].

4.2 Light through tiny holes

To understand the significance of Ebbesen's discovery, let us first look at Bethe's treatment of the situation of light through a sub-wavelength aperture, published in 1944 [23]. Bethe looked at the idealized situation of an opaque, perfectly conducting, infinitely thin screen in which there was one circular sub-wavelength aperture. In his paper, Bethe found that the transmission efficiency, or the transmitted power normalized to aperture area, through such an aperture can be shown as

$$\frac{P}{A} = \frac{64k^4r^4}{27\pi^2} \qquad (\mathrm{Wm}^{-2}) \quad (4.1)$$

where $k = 2\pi/\lambda$, $A = \pi r^2$, r is the radius of the aperture and λ is the wavelength of the light [23].

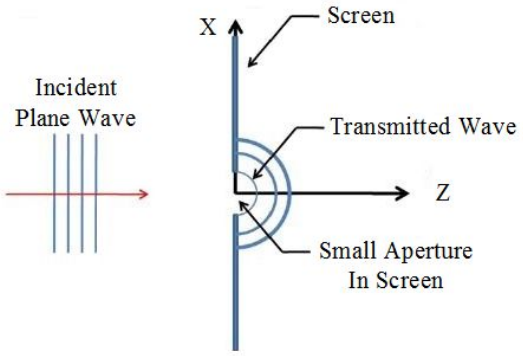

Figure 4.1: Diffraction of incident light through a small hole. The resulting wave radiates spherically from the hole. The radiant flux from the spherical wave-front rapidly decays as $1/z^2$ [7].

Solving for the power through the hole one can restate equation 4.1 in this way:

$$P = \frac{64(\frac{2\pi}{\lambda})^4 r^4}{27\pi^2} A = \frac{64 \cdot 16\pi^4 r^4}{27\lambda^4 \pi^2} \pi r^2 \quad \text{(W)} \quad (4.2)$$

$$P = \frac{64 \cdot 16\pi^2 r^6}{27\lambda^4} \propto \frac{r^6}{\lambda^4}. \quad (4.3)$$

Equation 4.3 shows that the power of the resulting beam drops rapidly as r becomes smaller than λ. For example if the λ_1 is 1.0 mm and λ_2 is 2.0 mm with an aperture radius of 0.3 mm we can find the difference in the power through the aperture by using equation 4.3.

$$\frac{64 \cdot 16\pi^2 (0.3)^6}{27(1.0)^4} = 0.273 \quad \text{(W)} \quad (4.4)$$

$$\frac{64 \cdot 16\pi^2 (0.3)^6}{27(2.0)^4} = 0.017 \quad \text{(W)} \quad (4.5)$$

By doubling the wavelength, the power through the aperture is decreased by 16 times, as expected. Similarly, if we hold the wavelength constant at 1 mm and change the aperture

radius from 0.3 to 0.2 mm, we can illustrate the effect of hole size on the power output.

$$\frac{64 \cdot 16\pi^2 (0.3)^6}{27(1.0)^4} = 0.273 \quad \text{(W)} \quad (4.6)$$

$$\frac{64 \cdot 16\pi^2 (0.2)^6}{27(1.0)^4} = 0.024 \quad \text{(W)} \quad (4.7)$$

By decreasing the aperture radius from 0.3 mm to 0.2 mm, the power output has been decreased to less than 10% of the original power transmitted.

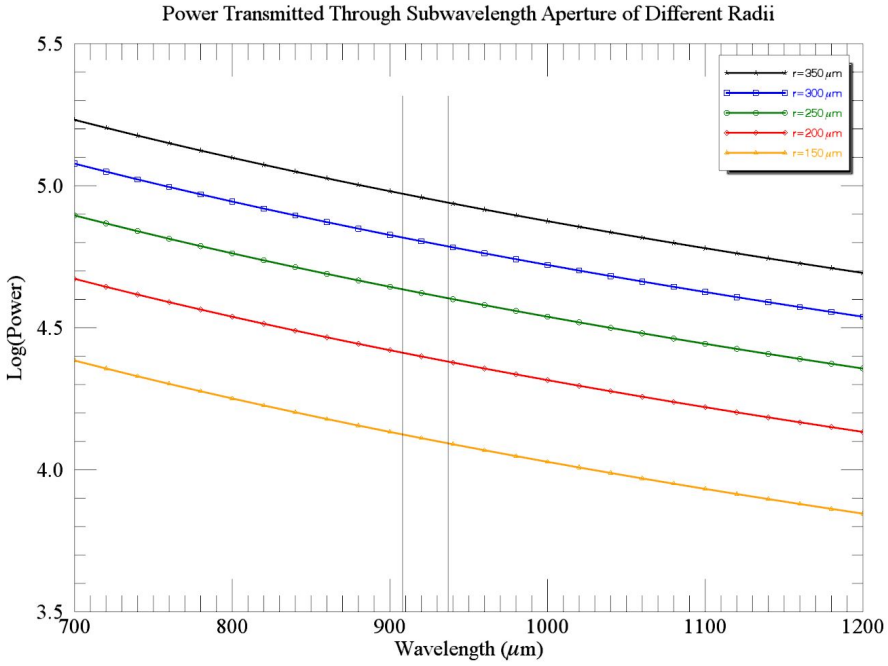

Figure 4.2: Transmitted power through a 350, 300, 250, 200, and 150 μm aperture in the Bethe limit. Power, as calculated using Equation 4.3, is plotted on a log scale and wavelengths range from 700 μm to 1200 μm, which includes the region of the THz range of interest(shown between vertical lines).

Figure 4.2 shows the transmitted power through a sub-wavelength aperture derived using equation 4.3. This range of apertures and wavelengths was chosen because it covers the range of interest of this experiment. Our research focuses on imaging with 0.325 THz radiation, with a wavelength of approximately 900 μm, through an aperture of either 200

or 300 μm.

4.3 Surface Plasmon Polaritons

Until 1998, Bethe's relations for transmission efficiency through sub-wavelength apertures was thought to be the best possible. This changed when Ebbesen *et al.*, reported on achieving extraordinary transmission through an array of sub-wavelength holes in the surface of a metal [24]. This extraordinary transmission was measured to be orders of magnitude greater than what was classically predicted [24]. Upon further inquiry, surface plasmons were discovered to be the mechanism which caused this extraordinary transmission [56]. Surface plasmons result from the collective charge oscillation of free electrons at the boundary of a metal dielectric interface [41]. When a surface plasmon couples with incident electromagnetic radiation, it forms a surface plasmon polariton which provides the mechanism for greater transmission through an aperture [57].

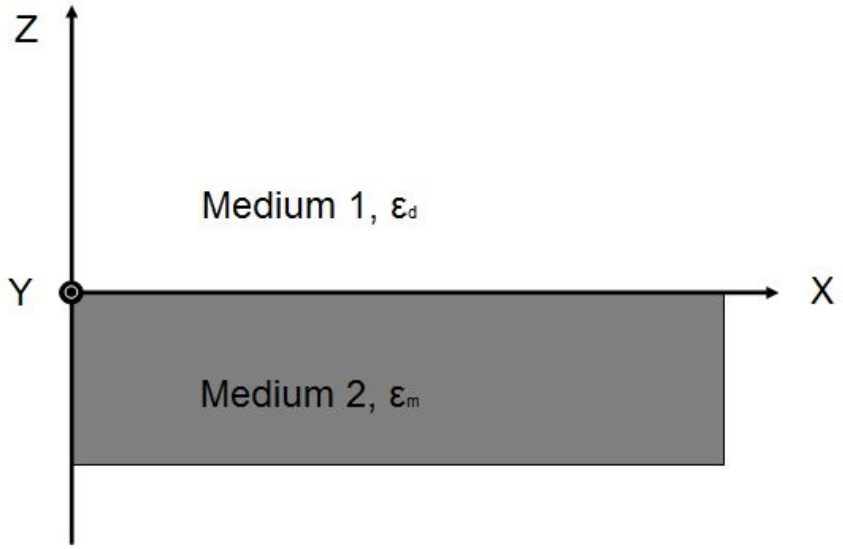

Figure 4.3: Diagram of the interface between two media. Medium 1 is a dielectric and medium 2 is a thin metal film.

For the purpose of this discussion, the interface will consist of a thin metal film and a

dielectric (ie. air); all lattice effects in the metal will be ignored. The dielectric constant of such a metal depends upon the wavelength of the oscillations of the free electrons and can be expressed as

$$\varepsilon(\omega) = 1 - \frac{\omega_p^2}{\omega^2} \tag{4.8}$$

where ω is the frequency, $\omega_p = \sqrt{Ne^2/m_0}$ is the bulk plasma, or volume, frequency of the free electrons in the metal, N is the number of free electrons, e is the electron charge and m_0 is the electron mass [7, 58]. Since SPPs can only form at an interface where

$$\frac{k_{dz}}{k_{mz}} = -\frac{\varepsilon_d}{\varepsilon_m} \tag{4.9}$$

is true, the interface must be between a metal and dielectric. At visible frequencies the choice of metal plays a significant role because the complex permittivity of the metal results in damping of the surface plasmon as it propagates. The situation is greatly simplified at THz frequencies since all metals behave as perfect electrical conductors [1].

4.3.1 Dispersion Relation

Due to a difference in the momenta of surface plasmons and incident radiation, SPPs do not form at the boundary of every metal-dielectric interface [41]. Typically a geometrical structure is required to match the momentum difference. The momenta of the surface plasmon and incident radiation are related according to

$$k_{sp} = k_0 \sqrt{\frac{\varepsilon_d \varepsilon_m}{\varepsilon_d + \varepsilon_m}} \tag{4.10}$$

where k_{sp} is the wave vector of the surface plasmon, $k_0 = \omega/c$ is the wave vector of the incident light and ε_d and ε_m are the permittivity of the dielectric and metal respectively [57]. This relation can be illustrated through a dispersion curve, see Figure 4.4.

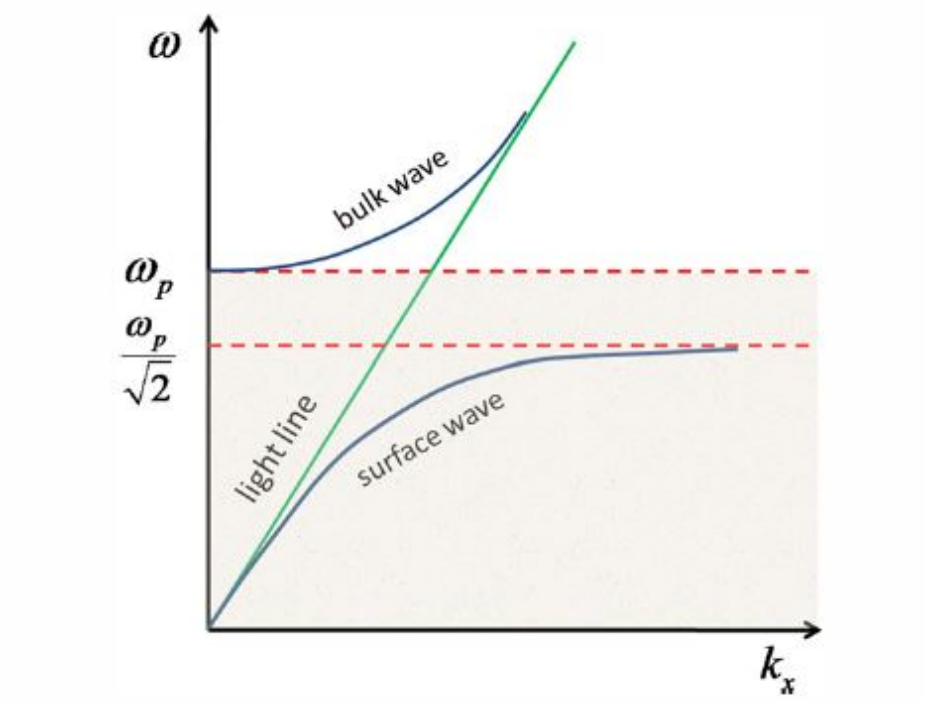

Figure 4.4: Plot of dispersion curve showing bulk wave propagation in metal above ω_p, the SPP resonance frequency $\omega_{sp} = \omega_p/\sqrt{2}$ and the surface wave propagation in the frequency interval $0 < \omega < \omega_{sp}$ [7].

From Figure 4.4, we can see that the surface plasmons have a longer wave-vector than incident light of the same frequency. This is the cause for the difference in the momenta of the two waves. In order for SPPs to form, this momentum difference must be bridged by an external mechanism, such as surface structures on the metal surface [7].

4.3.2 Skin Depth and Propagation Length

Skin Depth

SPPs are surface waves which are bound to the interface between a metal and dielectric. The distance that the wave can penetrate into either medium is known as the skin depth [59]. For SPPs, the skin depth can be written

$$\delta = \frac{1}{Im(k_{zm})} = \left(\frac{c}{\omega}\right)\sqrt{\frac{2}{\varepsilon_{im}}} = \left(\frac{1}{k_0}\right)\sqrt{\frac{2}{\varepsilon_{im}}} \tag{4.11}$$

where $Im(k_{zm})$ is the imaginary part of the wave-vector and ε_{im} is the imaginary component of the complex permittivity of the metal. From this we find that the skin depth into the metal depends on the imaginary permittivity of the metal; likewise, the skin depth into the dielectric depends on the imaginary component of the complex permittivity of the dielectric.

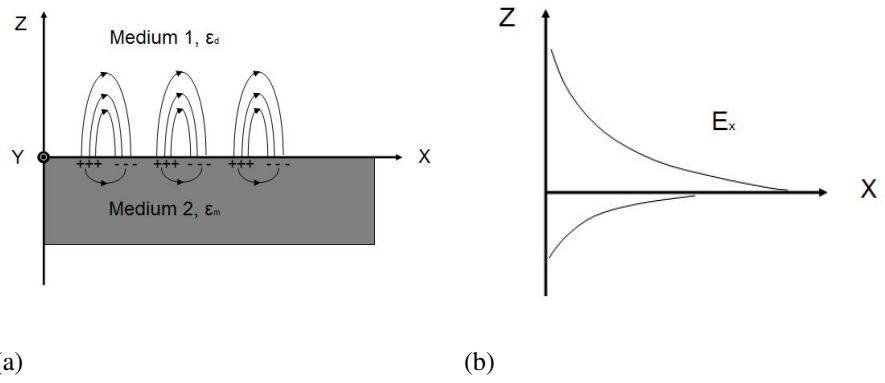

(a) (b)

Figure 4.5: Left: illustration of the skin depth of SPP in both the dielectric and the metal surfaces. The SPP can penetrate much further into the dielectric than into the metal. Right: plot of the decay of the SPP in each of the materials.

Figure 4.5 (a) shows how the skin depth changes depending on which side of the interface the wave is penetrating and (b) how it decays within that material. For wavelengths corresponding to THz frequencies, the skin depth in the metal approaches zero since the metal is essentially a perfect electrical conductor, see Table 4.1 [1]. Due to this, SPPs are bound to the surface of the metal, allowing for propagation only across the interface.

Propagation Length

The distance that the SPP can propagate along the metal dielectric interface is called the propagation length. This dictates the distance from the aperture that radiation can be collected, in order to potentially further increase the transmission through the aperture [59]. For SPPs the propagation length is defined as

$$L_x = \frac{1}{2k_x''} = \left(\frac{1}{k_0}\right)\frac{\varepsilon_d''}{\varepsilon_m^{3/2}} \tag{4.12}$$

	λ (m)	δ_m (m)	δ_d (m)	L (m)
Visible SPPs	$6.33\text{x}10^{-7}$	$3.00\text{x}10^{-8} \approx 10^{-2}\lambda$	$3.00\text{x}10^{-7} \approx 0.5\lambda$	$1.00\text{x}10^{-5} \approx 16\lambda$
THz SPPs	$9.22\text{x}10^{-4}$	$1.35\text{x}10^{-7} \approx 10^{-4}\lambda$	$3.00\text{x}10^{-1} \approx 10^{2}\lambda$	$3.30\text{x}10^{2} \approx 10^{5}\lambda$

Table 4.1: A comparison of the skin depth into the metal, δ_m, and dielectric, δ_d, and propagation length, L, of SPP at visible and THz wavelengths on a Au-air interface [1].

where k_x is the x component of the SPP wave-vector and " indicate the imaginary part. When the interface is between a metal and air (ε_{air}=1) this relation can be simplified to be

$$L_x = \left(\frac{1}{k_0}\right)\frac{1}{\varepsilon_m^{3/2}} \tag{4.13}$$

which means that the metal is the contributing factor that defines the distance of SPP propagation. In the visible, SPPs do not propagate far on most metals, resulting in gold and silver being the most common choices for SPP generation. In the THz regime, however, ε_m is very large, 5-6 orders of magnitude larger than in the visible, resulting in extremely long propagation lengths [1].

Table 4.1 shows a comparison of the skin depths and propagation lengths for SPPs at a single frequency in both the visible and THz regimes. As can be seen, the skin depth into the metal is two orders of magnitude smaller in the THz than in the visible with respect to the wavelength. Also, the propagation length is significantly larger in the THz than in the visible.

4.3.3 Conservation of Momentum and Satisfying the Boundary Conditions

From the dispersion relation, Equation 4.10, it can be seen that the momentum of a surface plasmon, $\hbar k_{sp}$, does not equal the momentum of free light, $\hbar k_0$. As a result, SPPs cannot be formed without a mechanism to match the momenta of the two waves [57]. As is seen in Figure 4.4, the SPPs lie on the larger wave vector side of the light line ($k_0 = \frac{\omega}{c}$), meaning that they have a larger wave vector than that of free electromagnetic waves. As a result, SPPs are not created on a surface without specific conditions being present to provide

the necessary matching term to conserve momentum. These conditions are essential to allow the coupling of electromagnetic waves with surface plasmons to form SPPs. The main way in which the difference in the momenta of the surface plasmon and the incident light is overcome is the use of a Bragg grating. See appendix A or [1, 57] for more information.

4.4 Plasmonic Lens

As noted previously, when imaging in the THz a mechanism to improve the spatial resolution is necessary. In addition, a method to enhance the transmission through sub-wavelength apertures is essential to the success of an imaging application. A plasmonic lens is a device which meets these requirements. One type of plasmonic lens, known as a Bullseye lens, employs concentric rings which form a two dimensional Bragg grating, necessary for momentum matching, around a sub-wavelength aperture [1, 57]. The Bragg grating allows for SPPs to form and propagate across the surface of the metal, facilitating extraordinary transmission through the sub-wavelength aperture [1].

The radius, spacing, width and depth of the rings and distance from the aperture of the first ring all impact the performance of the lens [60]. It is possible to adjust the lens design to a particular wavelength. In the visible, the material properties of the metal dictate the propagation length of SPPs. As noted above, since most metals act like perfect electrical conductors in the THz range the choice of material is relatively unimportant [1]. In addition, the side of the lens that the rings are on create different effects in the lens' performance. Rings that are facing the incident radiation lead to increased transmission, while rings on the output side of the lens act to confine the exiting beam.

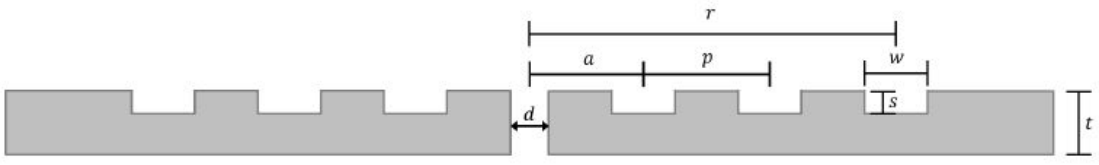

Figure 4.6: Cross-sectional diagram showing the definition of lens design parameters.

Research into optimal Bullseye lens designs has been focused in the visible region of the electromagnetic spectrum. In 2010, Mahboub *et al.*, reported on theoretical and experimental investigation of the optimal design for a Bullseye lens [60]. They discovered simple scale laws which can be used as "rules of thumb" for the design of a plasmonic lens for visible wavelengths.

$$\lambda \approx 1.1p \qquad \frac{w}{p} \approx 0.5 \qquad \frac{s}{w} \approx 0.4 \qquad \frac{s}{p} \approx 0.2 \tag{4.14}$$

where λ is the wavelength, p is the period of the grooves, w is the width of the grooves and s is the depth of the grooves. Work done within our group has been able to theoretically extend these simple relations into the THz region to determine equivalent "rules of thumb" for THz plasmonic lens design [1]. These were determined to be

$$\lambda \approx 1.041p \qquad \frac{w}{p} \approx 0.5 \qquad \frac{s}{w} \approx 0.3 \qquad \frac{s}{p} \approx 0.14 \tag{4.15}$$

Figure 4.6 shows a side view of a plasmonic lens with grooves on one side to define the design variables [1].

4.4.1 Design of Plasmonic Lens for THz Imaging Apparatus

The design and testing of the plasmonic lens used for this project was the subject of another student's thesis: Heggie, 2014 [1].

The plasmonic lens that was designed for this project was made out of copper and then coated in gold. The plasmonic lens was fabricated by Dr. E. Bordatchev from NRC Automotive and Surface Transportation and was funded by CMC Microsystems [61]. Figure 4.7 shows the design of the plasmonic lens [1]. The initial lens had grooves only on one side and was designed to enhance transmission of 0.325 THz radiation when oriented such that the light was incident on the grooves. The enhanced transmission of the lens as designed gave a theoretical gain factor of 55, while the theoretical transmission of the lens

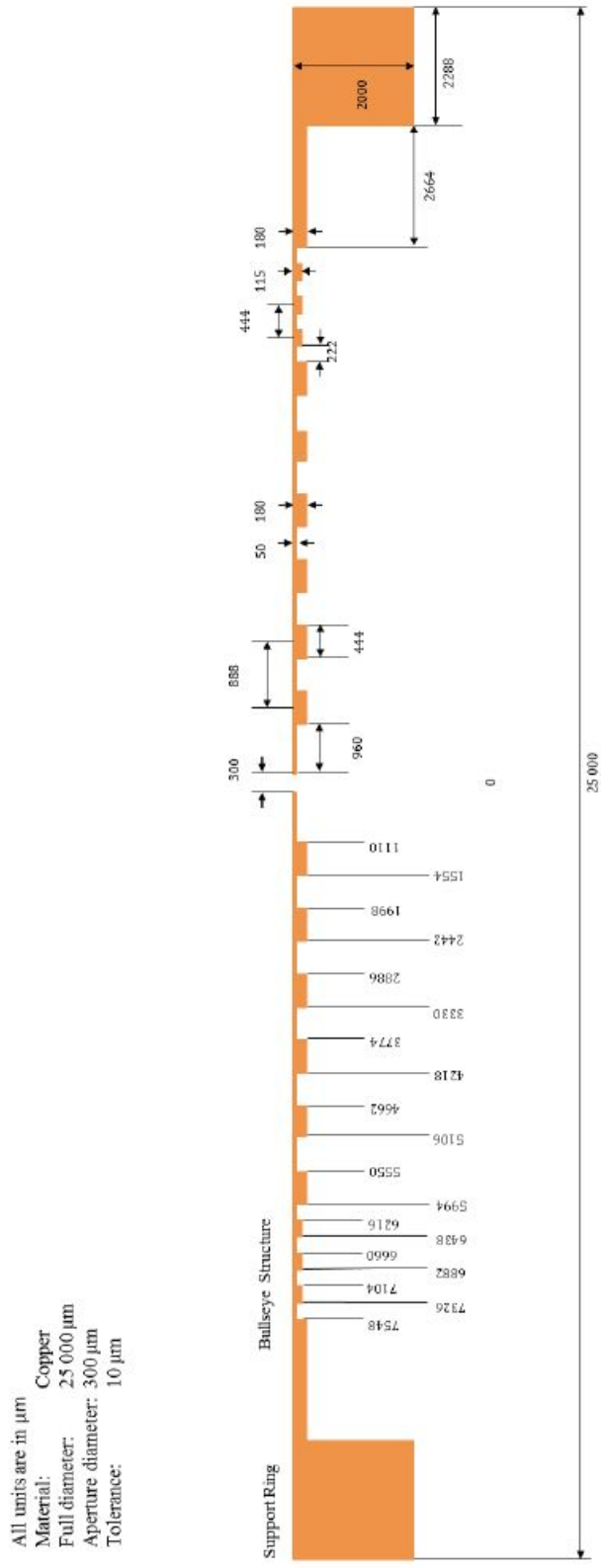

Figure 4.7: Schematic showing the design of one of the plasmonic lenses used in my thesis (cross-sectional view).

Parameter	Designed Value (μm)	Fabricated Value (μm)	Difference (μm)
Aperture Diameter	200	198.9	1.1
Aperture Thickness	20	20	–
Period	888	884	4
Width	444	442	2
Depth	130	124.3$\pm$0.6	5.7
First Ridge Pos.	1332	1331	1

Table 4.2: Comparison of the design and fabricated values for the plasmonic lens to shown accuracy of fabrication method.

as fabricated was about 48, see Figure 4.9. This difference is due to the differences in the specifications of the design when compared with the fabricated lens. A comparison of the design and fabrication specifications are given in Table 4.2.

Figure 4.8: Image of fabricated plasmonic lens.

As can be seen from Table 4.2, the difference between the specifications of the theoretical design and fabricated lens are small having a maximum variance of 5.7 μm. Even these small differences can, however, effect the performance of the plasmonic lens, as can be seen in Figure 4.9. Using the optical set-up for the knife-edge test, see Chapter 5, the transmission of the plasmonic lens was tested. Although the transmission of the lens is not as high as was predicted, it still manages to produce enhanced transmission by a factor of 38.

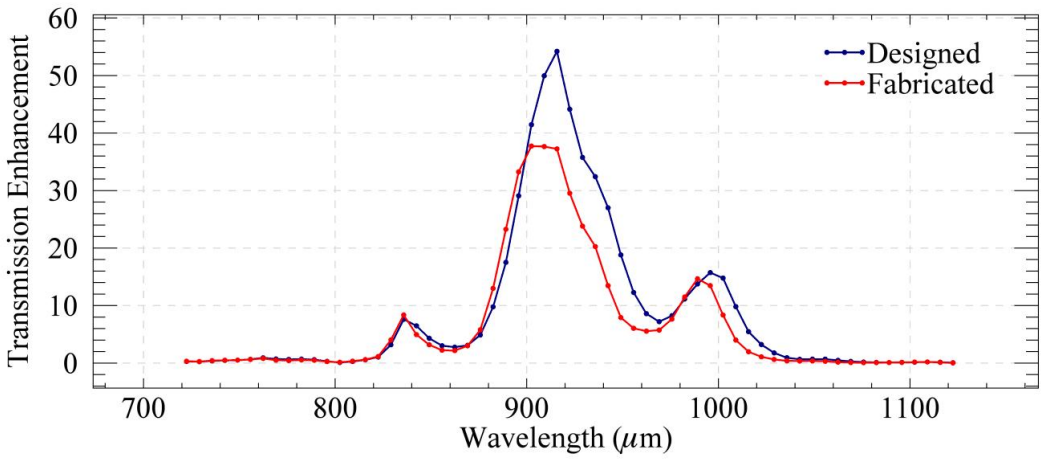

Figure 4.9: Simulated transmission enhancements of the designed and fabricated bullseye with the structural parameters given in Table 4.2.

Chapter 5

Knife-edge Test

5.1 Introduction

Verification of any instrument is required before it can be used for scientific purposes. The Thz microscope is described in detail in Chapters 6 and 8; in its simplest form, consists of a source, a defining aperture, a stage and a detector. To attain sub-wavelength imaging a plasmonic lens is required which operates on principles presented in Chapter 4. Once fabricated the performance of the plasmonic lens can be assessed using the Foucault, or knife-edge, test (KET) [62]. This test uses a sharp edged blade to determine the effect of the light going through the lens and allows location of aberrations in the lens or the beam shape to be determined.

5.2 Background

The KET was first developed and used in 1858 by Leon Foucault to test for aberrations in optical lenses and mirrors and is most useful for detecting transverse aberrations [62,63]. Flawed optics result in distorted images which could subsequently be mis-interpreted. By employing the KET in an iterative study of the aberration the lens makers would polish the part of the surface with the flaw to improve the quality of the lens.

5.3 Original technique

Testing for these aberrations involves moving a knife laterally through the focus of a beam produced by the optic in question [63]. The image, or shadow pattern, formed is

carefully observed to determine the presence of aberrations [62]. For a perfect lens or mirror, the shadow created by the knife-edge will appear straight as it moves across the light beam [62]. The shadow will appear to move in the same direction as the knife edge if the blade is positioned behind the focus of the optic, and in the opposite direction if it is in front of the focus [64]. Figure 5.1 illustrates this.

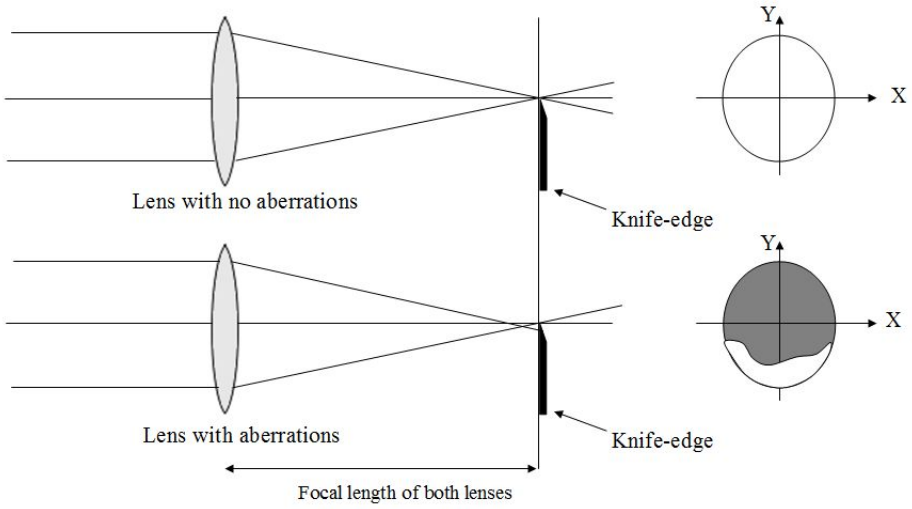

Figure 5.1: Diagram of the image resulting from a knife edge being placed in the beam at the focus for a lens with and without an aberration.

In the case of a lens with a spherical aberration, the shadow cast by the knife edge will appear distorted due to flaws causing light rays to move toward different foci, as shown in 5.1 [62]. As can be seen, the different ways the knife shadow deforms provide information on the type of aberration affecting the lens/mirror. Passing the knife edge through the light from different directions can allow the flaw to be accurately located for later removal. This method was particularly useful because of the ease which it lends to testing and retesting optics and the speed of obtaining results [63].

In our case, we use the KET not to measure component aberrations but rather to establish the intensity distribution and divergence of the THz beam incident on the plasmonic lens. The spatial parameters of the beam must be well known in order to design an imaging

system which will optimally couple THz radiation with the plasmonic lens. The KET can also be used to confirm extraordinary transmission by the plasmonic lens. In addition, the KET can provide a way to measure the intensity profile of the radiation beam output by the plasmonic lens that has structures on the output side, thus giving information about the beam size, intensity distribution, and divergence of the radiation used for imaging.

5.4 Optical Knife-Edge Test

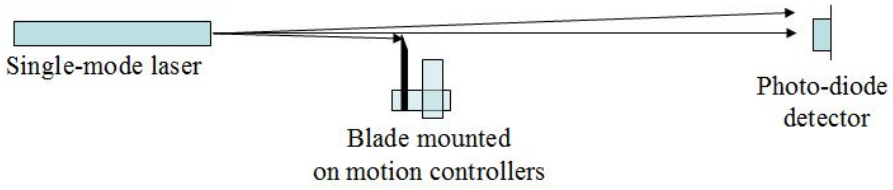

Figure 5.2: Schematic diagram of the optical KET setup.

Sensitive THz detector arrays are cryogenic based, operating at $\sim$50 mK, have complex read out electronics and are prohibitively expensive [65]. For these reasons, our THz imaging apparatus is designed to operate with a single source and detector. The initial THz imaging design uses a room temperature detector, with the intent of incorporating a cryogenic detector in future designs to increase the system sensitivity [66]. The use of a plasmonic lens in our THz microscope allows sub-wavelength imaging of tissue with THz radiation [20]. To interpret the images obtained with the THz microscope, the beam profile of the plasmonic lens must be well understood.

While waiting for the plasmonic lens to be fabricated, an optical testing apparatus was developed allowing the KET to be validated at visible wavelengths using an optical laser. Our apparatus for testing the KET at visible wavelengths made use of a single-mode frequency stabilized Helium-Neon laser, which is known to produce a well defined Gaussian beam profile, with a well known divergence [67]. Prior to discussing the procedure and results of this test, it instructive to introduce Gaussian beams.

5.4.1 Gaussian Beams

The optical source used to verify that the KET can be used in this capacity was a single mode laser, which by definition produces a Gaussian beam. This means that the beam exhibits a Gaussian intensity profile. Complete derivations can be found in [68]. Mathematically the beam profile can be represented as

$$I(r,z) = I_0[\frac{w_0}{w(z)}]^2 e^{-\frac{2r^2}{w^2(z)}} \tag{5.1}$$

where I is the intensity distribution, I_0 is the maximum intensity of the beam, and $r = \sqrt{x^2+y^2}$ is the radial distance from the axis of propagation. The beam radius, $w(z)$, is defined as the radial distance from the axis of propagation where the intensity of the beam falls to $1/e$ of its maximum intensity. The beam radius,

$$w(z) = w_0\sqrt{1+\left(\frac{z}{z_R}\right)^2} \tag{5.2}$$

also depends upon w_0 and z_R. w_0 is known as the beam waist, which means that it is the minimum cross-sectional radius of the beam. The spot size, which depends upon the beam waist, is defined to be $2w_0$. The Rayleigh range, z_R, is the distance from the focal point of the beam where the radius increases by a factor of $\sqrt{2}$ and the cross-sectional area increases to twice its minimum value, this is also defined as

$$z_R = \frac{\pi w_0^2}{\lambda} \tag{5.3}$$

The depth of focus, b, depends on the Rayleigh range and is defined as $2w_R$, and defines the portion of the beam that is planar.

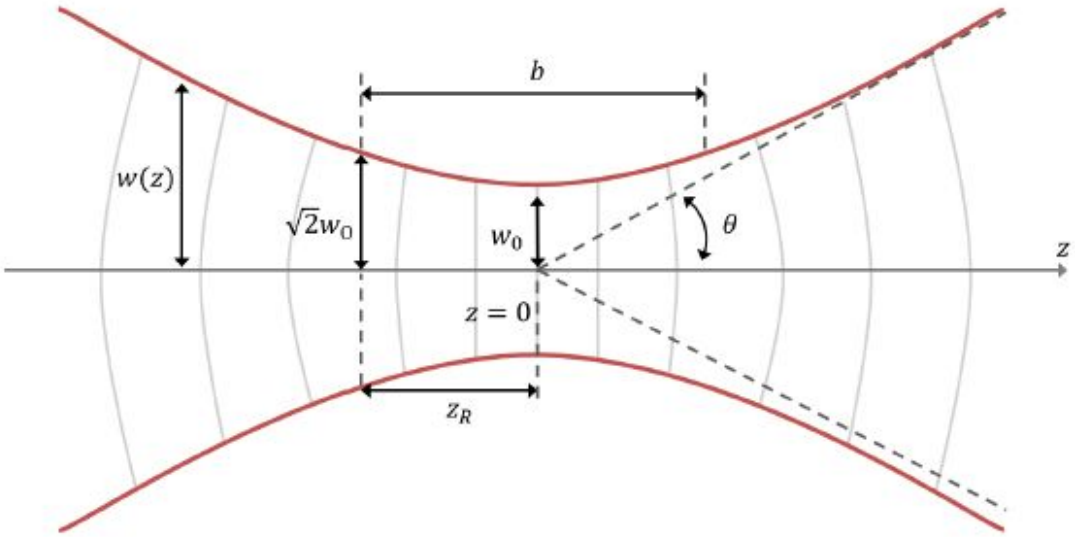

Figure 5.3: Diagram showing the parameters of a Gaussian beam and how they define the beam [1].

At distances much greater than the Rayleigh range, $z >> z_R$, the beam radius can be approximated to be

$$w(z) = \theta z \tag{5.4}$$

where θ is the divergence half-angle of the linearly diverging beam. The divergence half-angle can also be expressed

$$\theta = \frac{w_0}{z_R} = \frac{\lambda}{\pi w_0} \tag{5.5}$$

which is proportional to the wavelength of the light and inversely proportional to the beam waist. The wave front of the Gaussian beam is curved, where

$$R(z) = z + \frac{z_R^2}{z} \tag{5.6}$$

defines the curve of the front, except at the beam waist where the wave front is planar [69].

5.4.2 Apparatus

A Spectra-Physics Stabilized Helium-Neon Laser- Model 117A, which is a single-mode laser, was used to validate the KET [67]. This single-mode laser, with its well-known Gaussian beam profile, was the ideal source to evaluate the instrumentation of the KET. The apparatus used to complete these tests, see Fig. 5.4, required a optical laser, an optical detector, a razor blade and three (though only two were utilized) piezoelectric motorized translation stages.

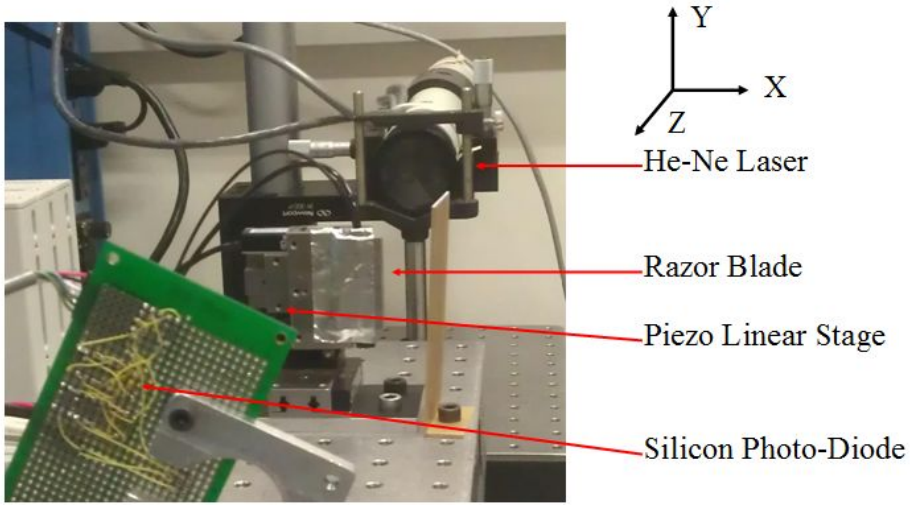

Figure 5.4: Optical set-up for the KET showing the four main components of the system: Helium-Neon laser, razor blade mounted on piezo linear stages and silicon photo-diode detector.

The Helium-Neon laser can either be used in a frequency stabilized or intensity stabilized mode. The frequency stabilizing mode keeps the frequency of the laser stable to within $\pm 2-3$ MHz over an extended period of time (hours-days). In this mode, the intensity of the beam is allowed to vary within $\pm$ 1% [67]. In the intensity stabilizing mode, the intensity of the beam is held constant to within $\pm$ 0.1%, but allows the frequency of the beam to fluctuate within about $\pm$ 5 MHz within one hour [67]. The intensity stabilizing mode was used during this experiment. The original beam diameter was given to be 0.5 mm and the beam divergence was 1.8 mrad [67].

The optical detector used was a Thorlabs FDS100 silicon photo-diode [70]. This detector had a range of 350 - 1100 nm, with its peak wavelength at 980 nm [70]. The rise and fall times of the detector were 10 ns [70].

To precisely control the position of the knife-edge as it traversed the laser beam, it was mounted on three Newport piezoelectric motor driven linear stages, model AG-LS25-27, though only two were used for motion [71]. These translation stages have a resolution of 0.2 μm, a maximum displacement of 27 mm and a maximum speed of 0.5 mm/s [71]. Attached to the linear stages was the razor blade with which the beam was cut. These three linear stages provided the ability to move the knife-edge through the beam at different distances from the source and allowed one slice across the beam to be accomplished in approximately 30 seconds.

5.4.3 Technique and Analysis

The KET was performed by translating a razor blade across the laser beam. Data were recorded as the knife blade was translated perpendicular to the beam (x,y) resulting in an error function profile, or 'S' curve [72]. Additional measurements could then be taken at various distances (z) from the laser to provide further information about beam divergence.

For our purposes, the knife-edge test is useful in experimentally determining a light beam's profile, divergence and focus. In verifying the applicability of this method, we used a known light source, an optical laser, and measured the intensity of the beam as a knife edge was moved across it. The intensity could then be plotted as a function of blade position generating the 'S' curve, see Figure 5.5 for the theoretical error function curve and Figure 5.6 for the experimental curve. The error function is defined as

$$erf(x) = \frac{2}{\sqrt{\pi}} \int_0^x e^{-t^2} dt \tag{5.7}$$

which differentiates to a Gaussian function [72].

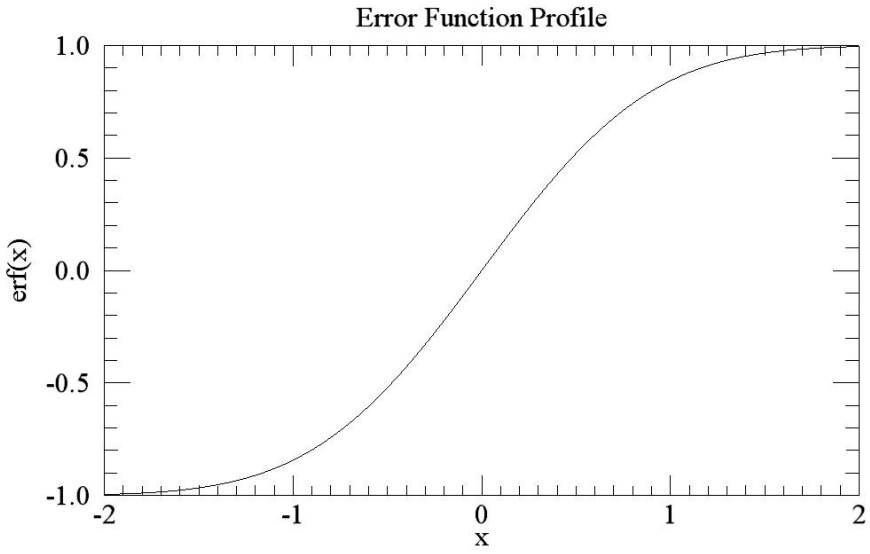

Figure 5.5: Example of the error function, 'S', curve. Plot was created using Equation 5.7.

Taking the first derivative of the intensity data gives a plot of a cross-section of the beam shape. As expected, the beam shape of this laser has a Gaussian profile. The right plot in Figure 5.6 shows the raw data (black) fitted with a Gaussian curve (blue). The agreement between the two is evident. Beam radius can be found by determining the full width at half maximum (FWHM) of the experimental Gaussian data. FWHM is $2\sqrt{2ln2}\sigma$.

The beam divergence was found by taking data with the razor blade a different distances from the laser source. Intensity and first derivative plots were found at each distance, see Figure 5.7. From the different derivative curves the FWHM was obtained and plotted against the distance from the source of the razor blade, see Figure 5.8. As can be seen, the slope of each intensity curve decreases as the knife edge is moved away from the laser. This corresponds to the widening of the Gaussian curves and shows that the beam is diverging. Fig. 5.7 shows the raw data, without averaging.

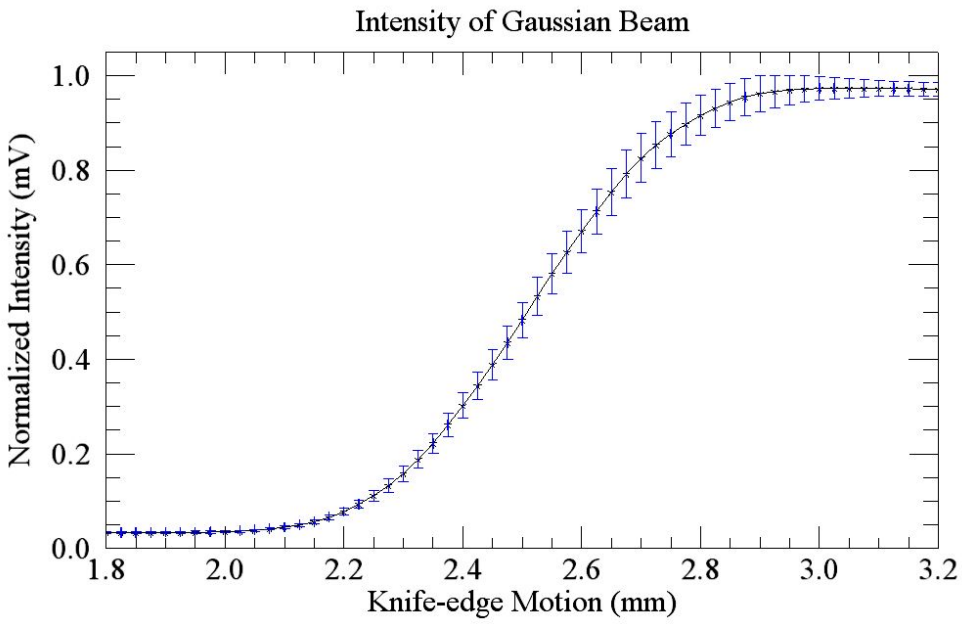

(a)

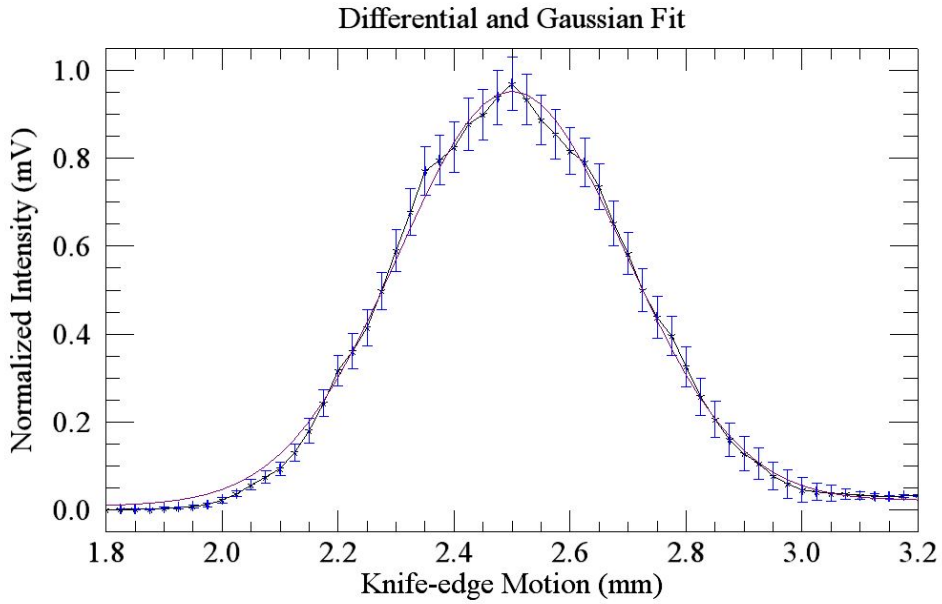

(b)

Figure 5.6: Plots of data taken at z = 26.2 cm from the laser, cut in x, showing beam intensity as a function of blade position (a) and first derivative (b), with the expected Gaussian shape. Black is the real normalized data and blue is the best-fit Gaussian curve. It can be seen that the measured beam profile is well described by a Gaussian profile. Error bars represent +/- one standard deviation. Error in position is insignificant on these plots.

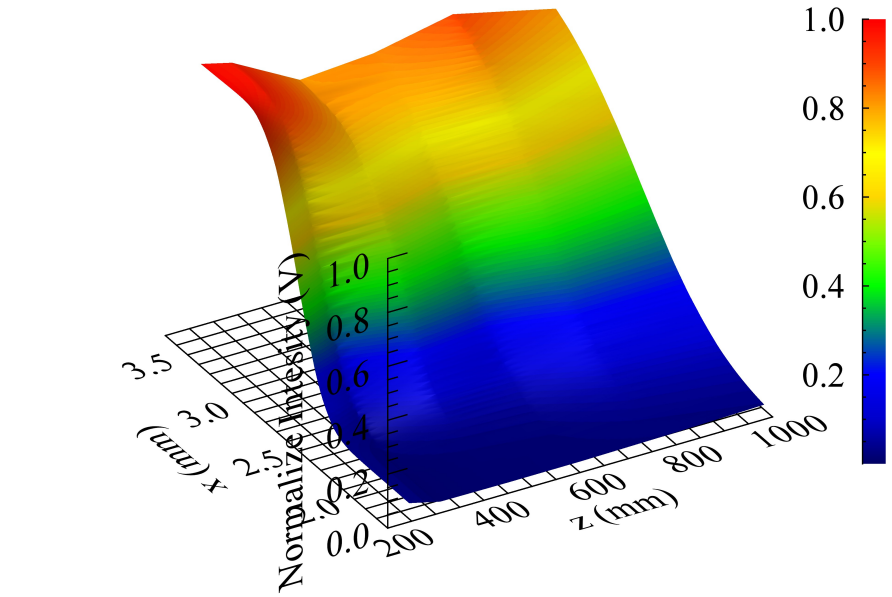

(a)

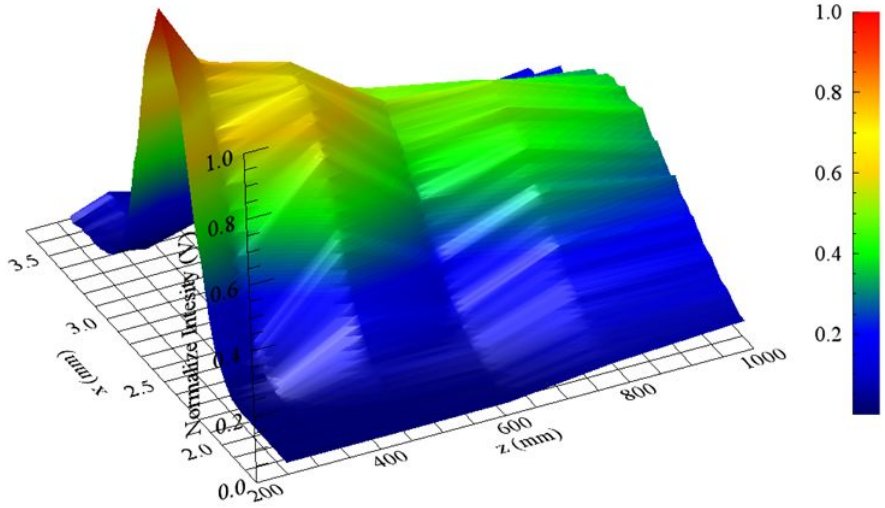

(b)

Figure 5.7: Normalized intensity (a) and Gaussian (b) profiles of the beam for increasing distances from the laser. As the beam diverges the signal to noise in the measurement decreases, leading to the noise seen in the broader beam.

A value for the beam divergence can be found by determining the slope of a plot of

the change in FWHM, for first derivative data, or slopes, for intensity data, with distance. Fig. 5.8 shows that the relationship between the width (FWHM) of the beam profile and the distance from the source is linear. From the fitting the FWHM values found for the beam profiles taken at each position, shown in Figure 5.8, the divergence of the laser beam was found to be 1.02 ± 0.2 mrad.The beam divergence of a typical single-mode laser is 1.8 mrad [67].

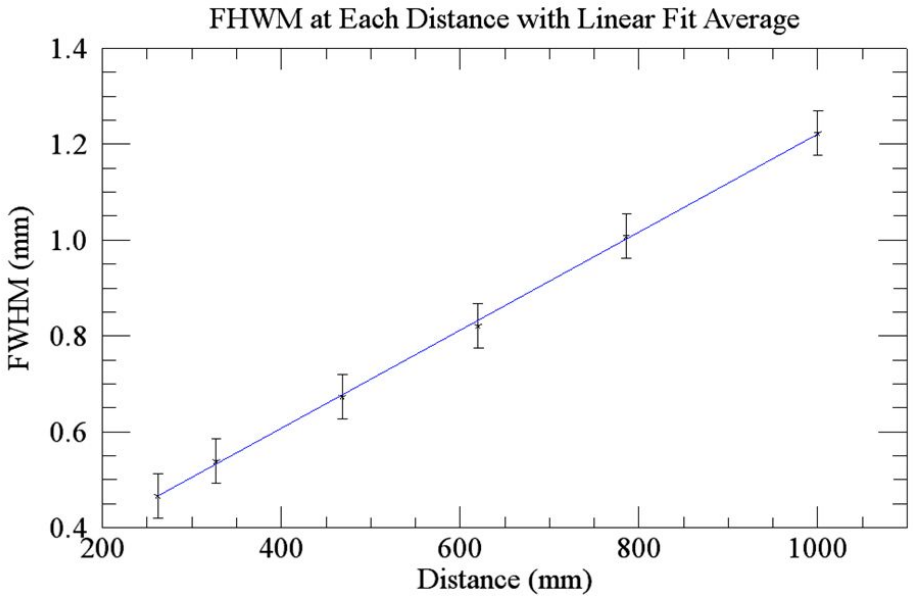

Figure 5.8: The measured FWHM at the six distances in Figure 5.7 plotted against distance shows a linear trend from which the divergence of the laser can be determined.

5.5 TeraHertz Knife-Edge Test

After the KET had been verified in the optical, it was modified for use in the THz regime to measure and confirm the modelled performance of the plasmonic lens. Transmission through the plasmonic lens had been modelled but still needed to be confirmed experimentally. The requirements for the THz set up were much more strict than had been necessary in the visible to ensure reliable results. For example, due to the optical properties of most materials in the THz (all surfaces acted like mirrors) causing reflections and, potentially, resonance within the apparatus. In addition, the beam is not visible to the eye,

diverges significantly and is not purely Gaussian in shape, making alignment and focusing significantly more difficult. Testing of plasmonic lenses with the KET was part of Tanner Heggie's thesis [1].

5.5.1 Components and Set-up

The THz set up included a THz line source, four 90^o off-axis parabolic mirrors, a knife-edge mounted on the same piezo-electric stages, and a detector. The THz source was a Virginia Diodes, Inc. line source transmitter with a frequency bandwidth of 0.32 - 0.33 THz (908 - 937 μm) [73]. The source produces a beam which is predominantly Gaussian and is horizontally polarized with a maximum power of 10 mW. The source was modulated and the signal detected by a lock-in amplifier to increase the sensitivity of the measurements [1]. The details of the source are provided in Appendix B.

The same type of knife edge, as used in the optical format, was used here and it was mounted on the same piezoelectric stages to allow for precise motion. The detector used is a zero-biased GaAs Schottky diode with an optical noise-equivalent power of 2.9 pW/$\sqrt{Hz}$ which accepts horizontally polarized light [73]. When the incident power on the detector is sufficiently small (0 - 10 μW) the response of the diode is linear [73]. The details of the detector are provided in Appendix B.

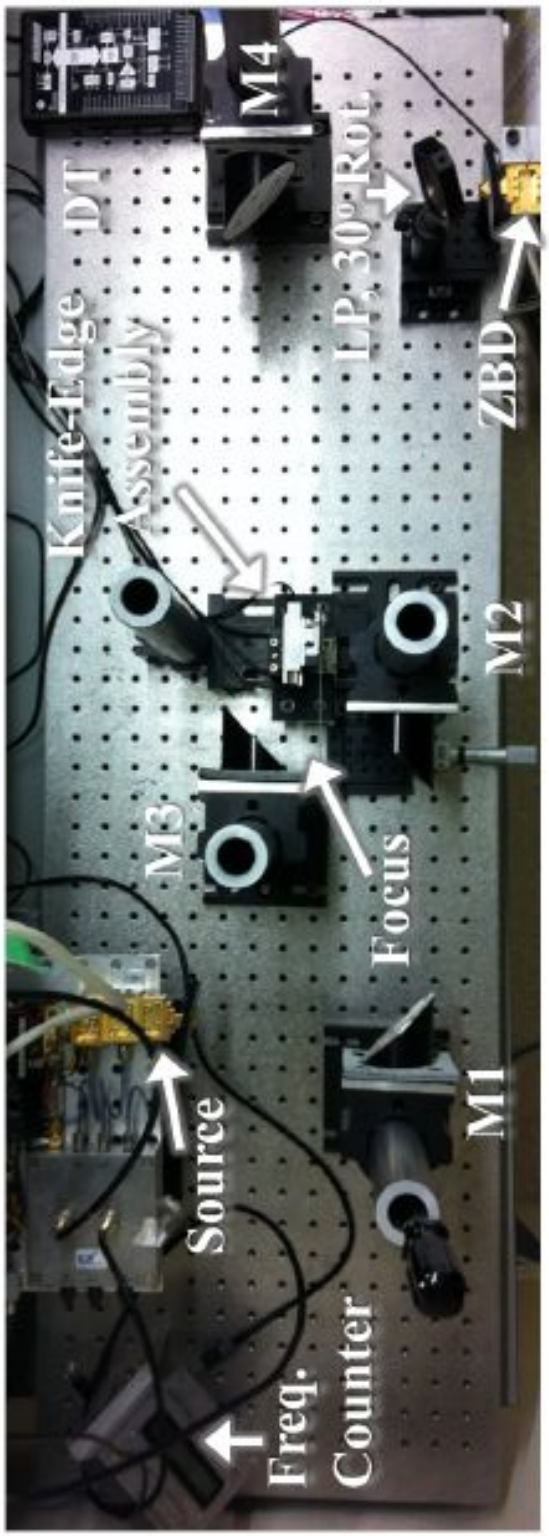

Figure 5.9: Eop down view of the THz KET testbed. [1]

5.5.2 Results

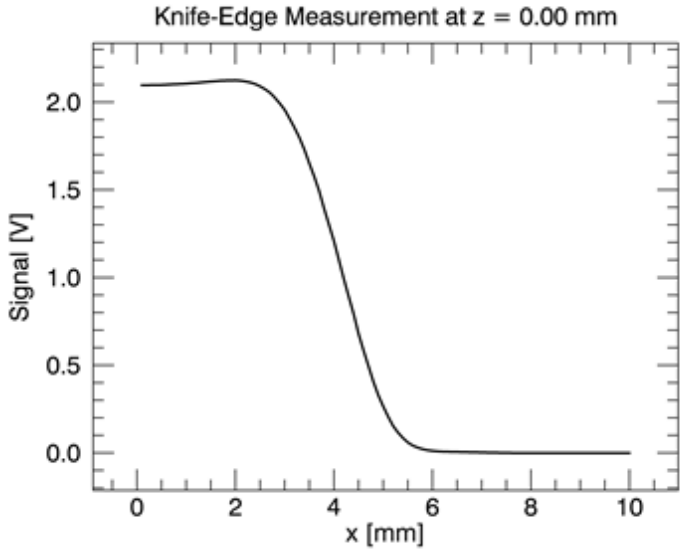

(a)

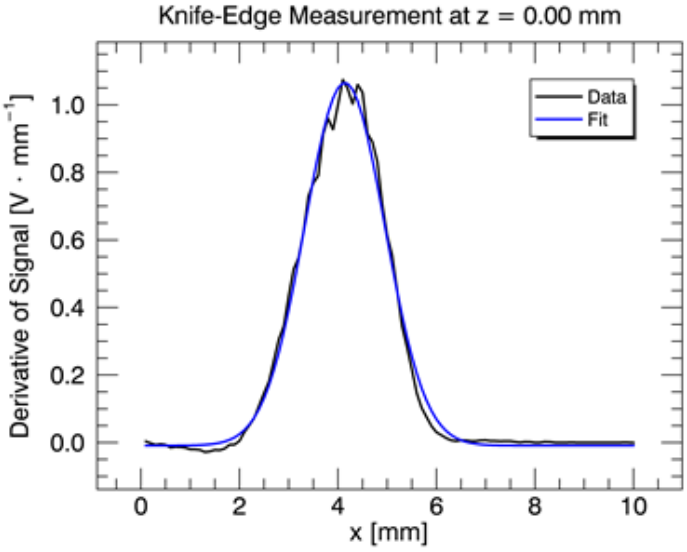

(b)

Figure 5.10: (a) Shows the raw intensity profile for the THz beam. (b) Shows the beam profile achieved by taking the first derivative of (a). From (b) we can see that the THz profile is primarily Gaussian and agrees well with theory [1]

Like the optical KET, the original data from the THz KET is an intensity or 'S' curve, see figures 5.10(a) and 5.11(a). Taking the first derivative gives the beam shape at the point where the knife cut, see Figure 5.10(b). When all the data from sweeps of the blade at different points in the beam are combined one can determine how the shape of the beam changes with distance. From Figure 5.11(b) we can find the focus of the beam, since it corresponds to the most intense point in the sweep and the narrowest point in the beam. This also gives greater understanding of the profile of the transmitted beam from the plasmonic lens.

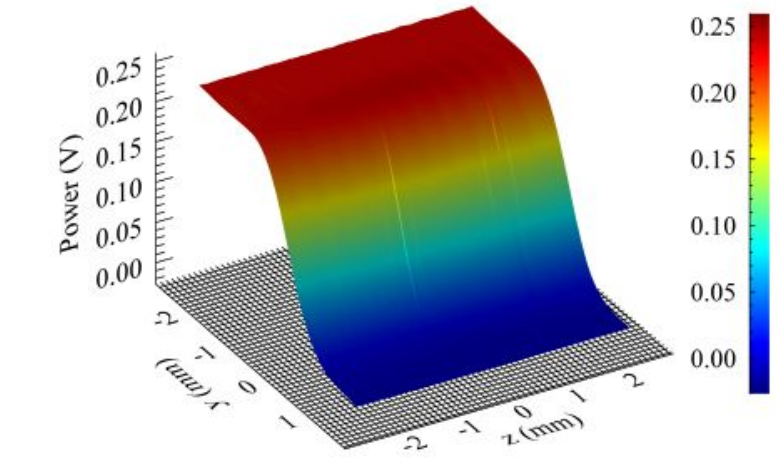

(a)

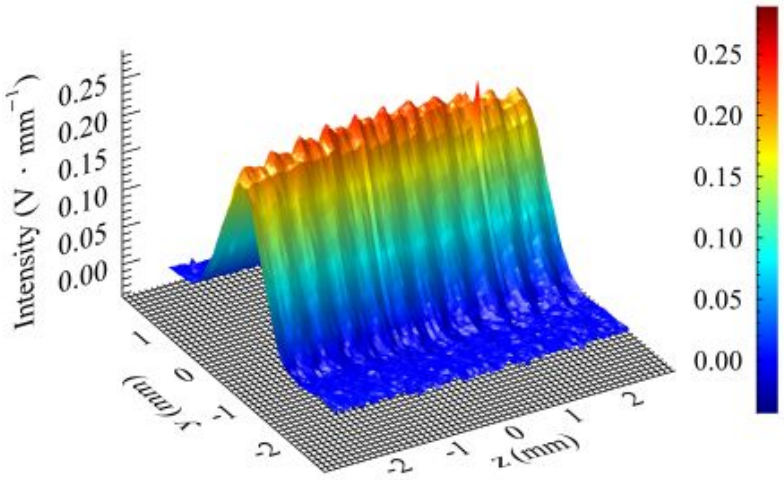

(b)

Figure 5.11: THz data acquired by means of the KET. (a) shows the original 'S' curve and (b) the Gaussian beam shape after the data were differentiated. [1]

It can be seen that the curves shown in Figures 5.6 and 5.10 have the same initial 'S' curve, which then differentiates to show the Gaussian profile of the beam. While Figure 5.7 shows the divergence of the optical laser, the results seen in Figure 5.11 show the beam as it is re-focused by the optics in the apparatus. The focus of the beam was determined in this way, although fringing due to internal resonance within the system must be taken into account [1].

Chapter 6

Optical Image Acquisition

6.1 Introduction

As discussed in Chapter 3, THz radiation at around 0.3 THz exhibit the greatest differential between the absorption coefficients of healthy and cancerous breast tissue [6]. In general, spatial resolution is the order of the wavelength of light, as shown in Chapter 3 THz imaging has low spatial resolution ($\sim$ 1 mm); to be useful in cancer diagnosis, however, a significant improvement is required. One method of improving spatial resolution is using a Bullseye plasmonic lens, see Chapter 4. Using such a lens leads to spatial resolution on the order of the diameter of the aperture and extraordinary transmission through the aperture [22, 23].

In 2009 Chiu *et al.*, reported on using a THz microscope with a plasmonic lens to image samples and differentiate breast cancer from healthy tissue [16]. Our goal was to extend the work of Chiu *et al.*, and, using the expertise within the Astronomical Instrumentation Group (AIG) in THz technology and precision metrology, develop a faster scanning, more sensitive THz imaging apparatus for use in cancer diagnostics.

Since the design, fabrication and testing of the plasmonic lens took some time, an optical analogue of the THz imaging system was constructed for troubleshooting and software development. The optical imaging system was designed to work with a single detector and a pin hole light source, since the THz system would also, by necessity, utilize a single detector. In this configuration, shown schematically in Figure 6.1(a), the sample must be moved to allow a multi-pixel image to be formed, see Section 6.2.1. Analysis of the optical

data acquired with this system is discussed in Chapter 7. All software was developed using Interactive Display Language (IDL) and was designed for use with both the optical and THz systems [74]. This chapter describes the design, assembly and use the optical analogue of the THz imaging system. Unless otherwise stated, the work presented is my own, where others have contributed specific reference will be given.

6.2 Optical Apparatus Design

In their 2009 paper, Chiu *et al.*, took a time of 3000 sec (50 min) to scan a 10 mm x 10 mm sample with a step size of 100 μm [16, 50]. By 2011, improvements to their system allowed them to image the same sample area in 180 sec (3 min) [50] and further improvements reduced that time to 60 seconds in 2013 [26]. The THz imaging system was designed to acquire images of the same sample area with the same step size and be capable of the resolution and sensitivity required to differentiate cancerous and non-cancerous tissues. To validate the performance of the stage for THz imaging, optical images were acquired with a resolution of 10 μm, vastly exceeding the THz resolution requirement.

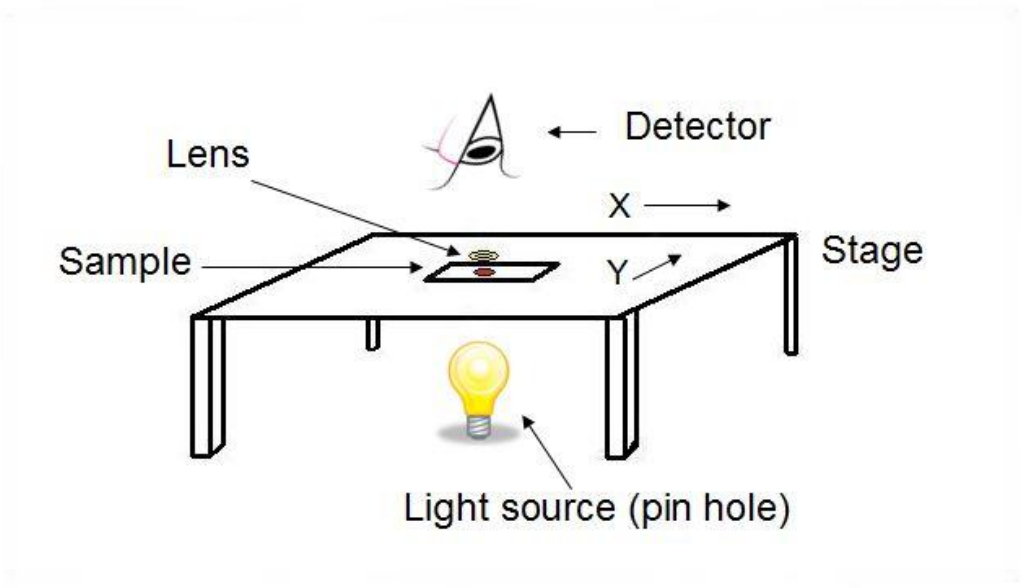

(a)

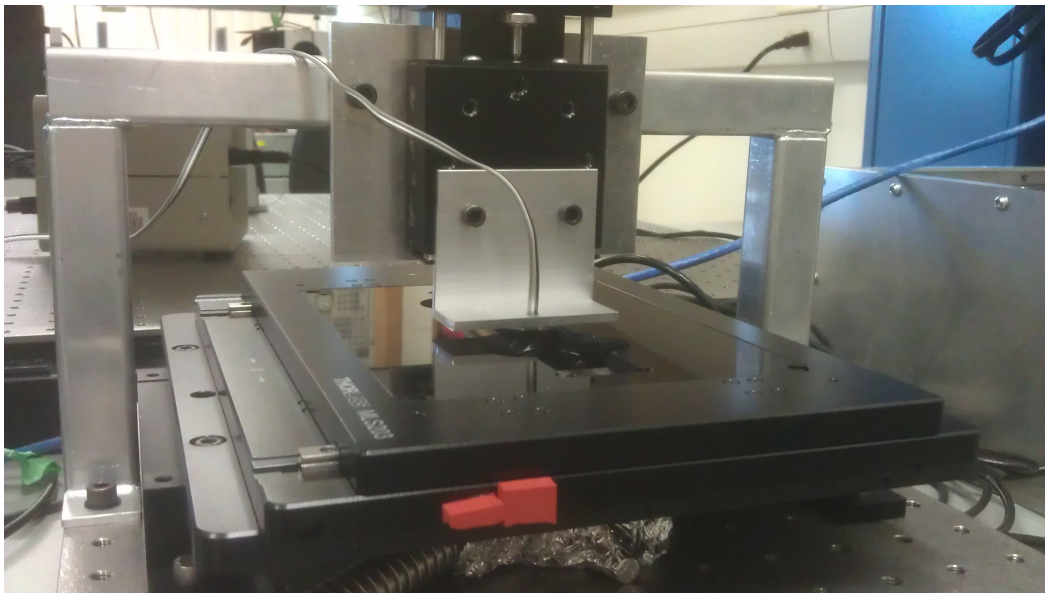

(b)

Figure 6.1: (a) Schematic of an optical imaging system. (b) Image of the optical light source, detector and X-Y stage. The light source is mounted on a micrometer bolted to an aluminium bridge.

6.2.1 Stage and Controller

(a)

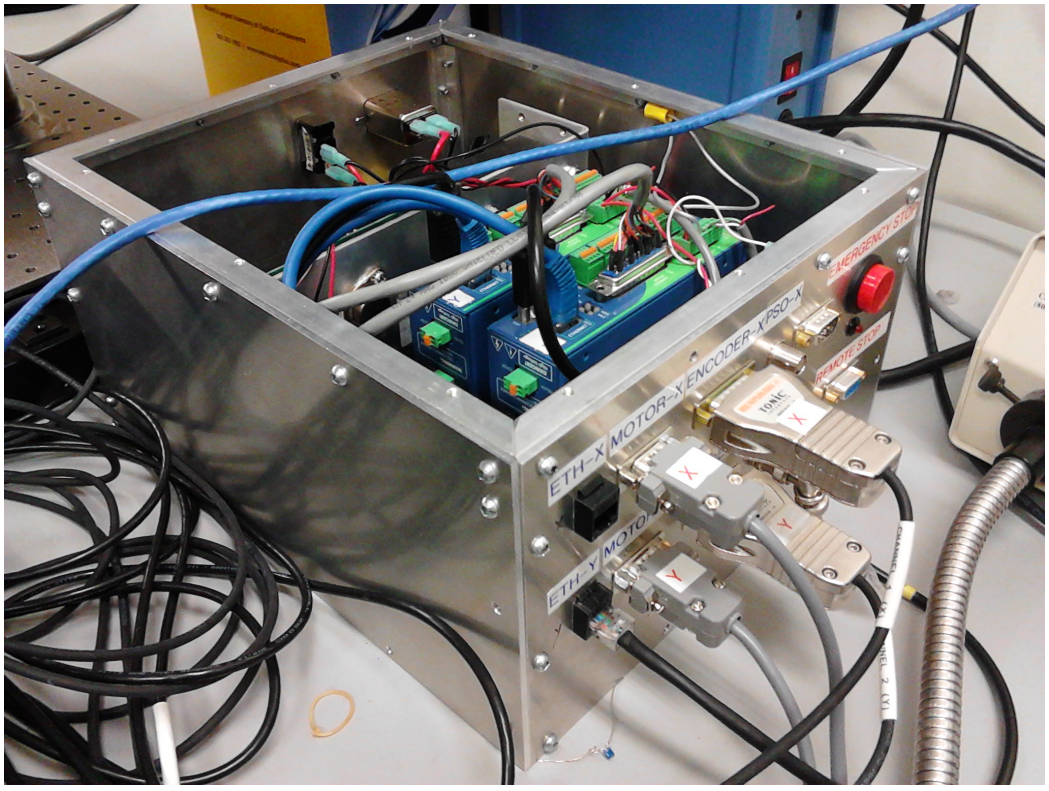

(b)

Figure 6.2: (a) View of Thorlabs two-axis stage. (b) View of the custom connections and set up for the Soloist controllers.

It was recognized early in the project that one of the largest improvements that could be made to the design of the Chiu *et al.*, imaging system was to improve the performance of a rapid scanning stage. In general, microscope stages are not designed for fast and precise point-to-point motion and data collection. The AIG has significant expertise, however, in designing and building single-axis systems which satisfy these requirements in their research in interferometry [65,66]. While a commercial solution for the two-axis translation stage that would meet the system's mechanical requirements was identified in the Thorlabs MLS203 x-y translation stage, upon further study it was found that the Thorlabs controller did not allow for pulse triggered data acquisition while the stage is in motion [75].

The interferometers developed by the AIG are based upon the Aerotech motion control product line in which a variety of single axis mechanical stages are controlled by a single controller called the Soloist [76]. The Soloist motion controller is an extremely flexible controller that can be programmed to drive a broad range of stages and produce a pulse at user selectable intervals of stage displacement, called pulse synchronized output (PSO) [77]. The PSO option allows for rapid data collection with precise spatial position information attached to each data point taken.

Unfortunately, because the stage and controller are manufactured by two different companies, interfacing them voided the warranties on both. Our industrial partner, Bluesky Spectroscopy Inc. was able to successfully integrate the Thorlabs stage with two Aerotech Soloist controllers, one for each axis. While I was not involved with this process, this involved determining the pole spacing of the linear motor and the resolution of the linear encoder on the MLS203.

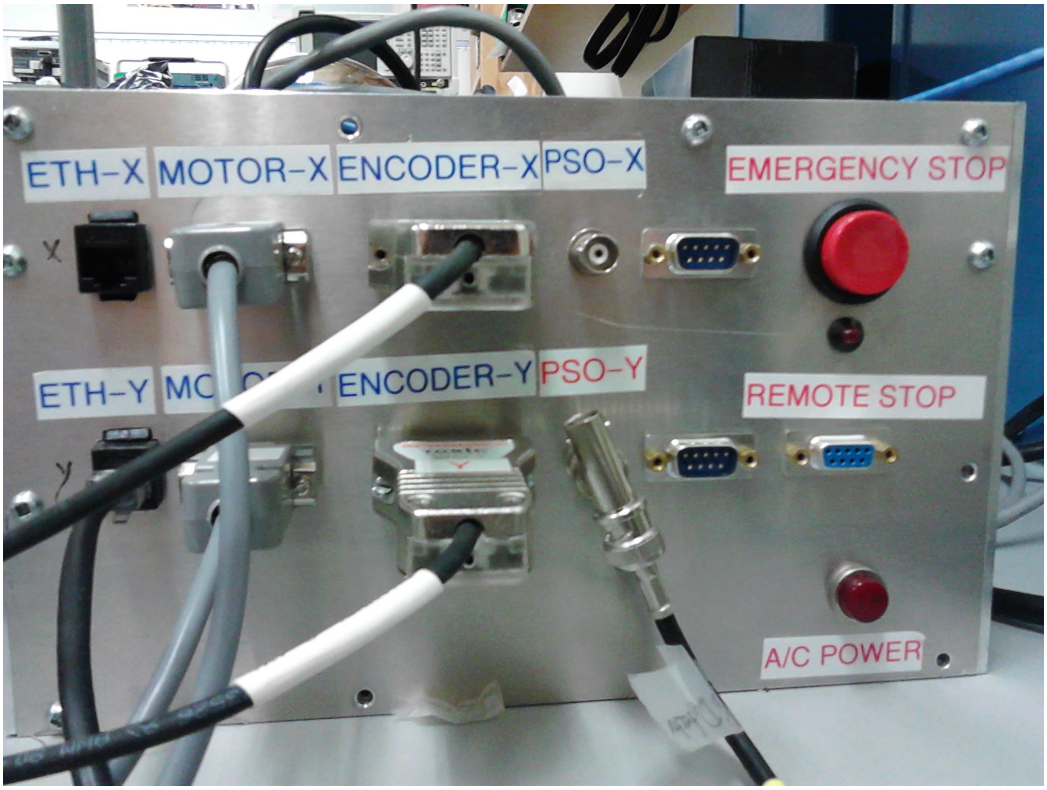

Figure 6.3: View of the custom connections and set up for the Soloist controllers. The PSO of only one Soloist controller was in use at any time.

Since the Soloist controllers and the MLS203 stage were integrated in-house, all the connections had to be custom designed. Figure 6.3 shows the custom connections that were built to connect the controllers with the stage. In addition to the motor and encoder, connections were required to run each axis of the stage, a port to allow for the PSO option to trigger sampling of the detected signal, as well as an emergency stop button as an added safety feature.

6.2.2 Slide Holder

As discussed in Chapter 3, to achieve sub-wavelength resolution imaging at THz frequencies requires the use of a plasmonic lens, see Section 4.4 for design specifications. To obtain maximum resolution, imaging with the plasmonic lens must be accomplished in the 'near field' (less than one wavelength between lens and sample). At 0.325 THz, this

distance is less than 1 mm. Due to this proximity requirement, it is essential that the slide be mounted and moved without any risk of coming in contact with the lens and that the illumination be from above the sample.

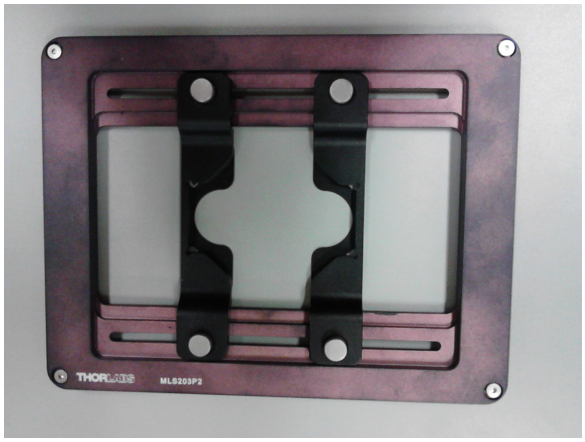

Figure 6.4: Original Thorlabs stage MLS203 slide holder. Note the knobs which protrude above the surface of the slide holder.

The Thorlabs stage came equipped with a adjustable slide holder, shown in Figure 6.4. Although this slide holder allowed for versatility of position and size of slide, it did not permit the lens to be mounted sufficiently close to the sample for our purposes. To resolve this issue, I designed a new slide holder that would be useful for both optical and THz imaging applications.

As discussed in Chapter 2, typically tissue samples are mounted on standard microscope slides. These slides are made from glass and are 75 mm by 25 mm in length and breadth and are about 1 mm thick [32]. Section 3.5.3 discusses the drawbacks associated with mounting samples on a standard microscope slide for THz imaging. A potential way to mitigate these problems is to mount the sample onto a cover slip, rather than a slide. Cover slips are designed to fit within the surface area of a slide to protect the sample from external contamination after mounting has taken place. The cover slips that I was working with were approximately 50 mm long and 25 mm wide with a thickness of 150 μm, though dimensions vary depending upon application.

Since all the samples prepared for imaging are mounted on either standard slides or cover slips with these approximate dimensions, I designed a slide and cover slip holder to be used with the Thorlabs stage. The slide holder was designed such that the slide or cover slip would be flush with the surface, leaving no protrusions. The THz imaging apparatus is designed to illuminate the sample from above and to allow a spacing of $\sim 250\ \mu$m between the slide holder and the lens, which allows for the added sample thickness (10 - 30 μm). Importantly, the design of the slide holder utilizes the range of motion of the X-Y translation stage allowing the sample to be changed without moving the plasmonic lens. The holder also has cut-outs to allow the slide to be easily removed. The slide holder was fabricated out of black acrylic, chosen for its low mass, to the specifications found in Figure 6.5.

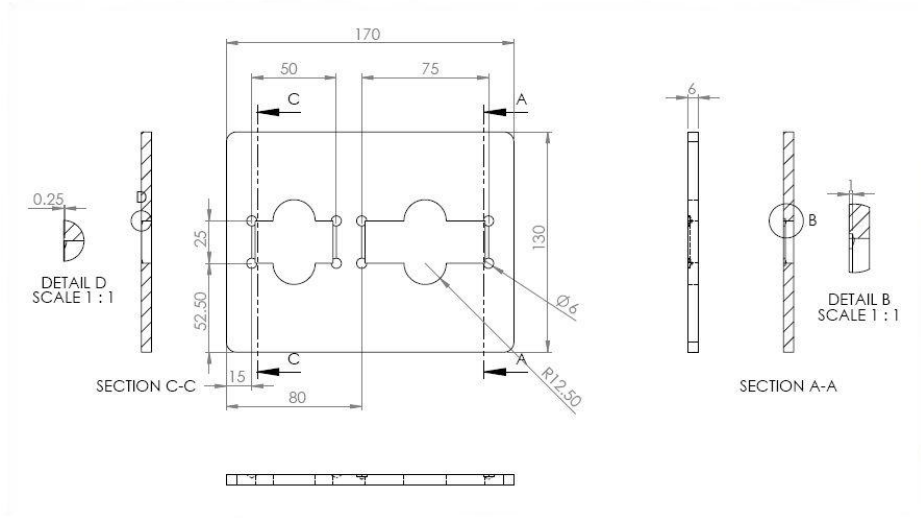

(a)

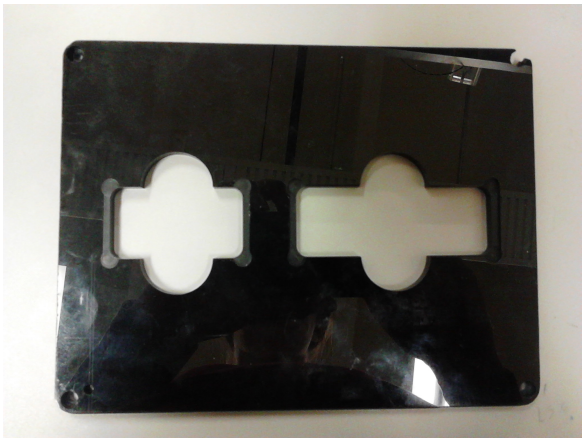

(b)

Figure 6.5: (a) Design for the new slide holder. (b) View of the fabricated slide holder. Note that the custom slide holder is designed to mount a 1 mm thick slide on right side and a 150 μm slide cover on the left side.

6.2.3 Optical Imaging Hardware Components

Light Source By experimenting with different light sources, which included Lambertian, LED and pinhole, we found that the pinhole produced the clearest images. For this reason the optical imaging system used a fibre optic illuminator, model IL-88-FOI, covered by a pinhole as the light source and defining aperture, seen in Figure 6.6. This was placed

underneath the translation stage and simulated the use of a point source. The brightness of the source was adjustable.

Figure 6.6: Image of the light filament ring underneath the stage prior to being masked with the pinhole cover.

Detector An optical detector was mounted above the X-Y translation stage, itself mounted on a linear micro-adjustable stage which was attached to a bridge made of 1 inch square aluminium tubing designed specifically for this purpose, seen in Figure 6.7. The detector was a TSL 250 series silicon photo diode optical sensor made by Texas Instruments [78]. For reasons that will be discussed in Section 6.4.2, two different detectors in this series were used in the imaging system, the final choice being a TSL 252.

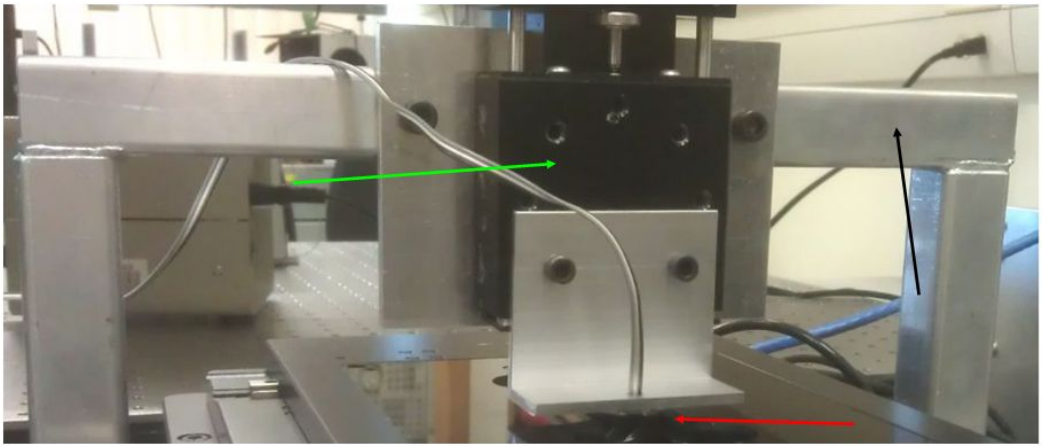

Figure 6.7: Image of the aluminium bridge with the micrometer and sensor attached. The bridge is indicated with the black arrow, the micrometer the green arrow and the detector the red arrow. The detector is hidden underneath the aluminium plate that holds it horizontal.

6.3 System Integration

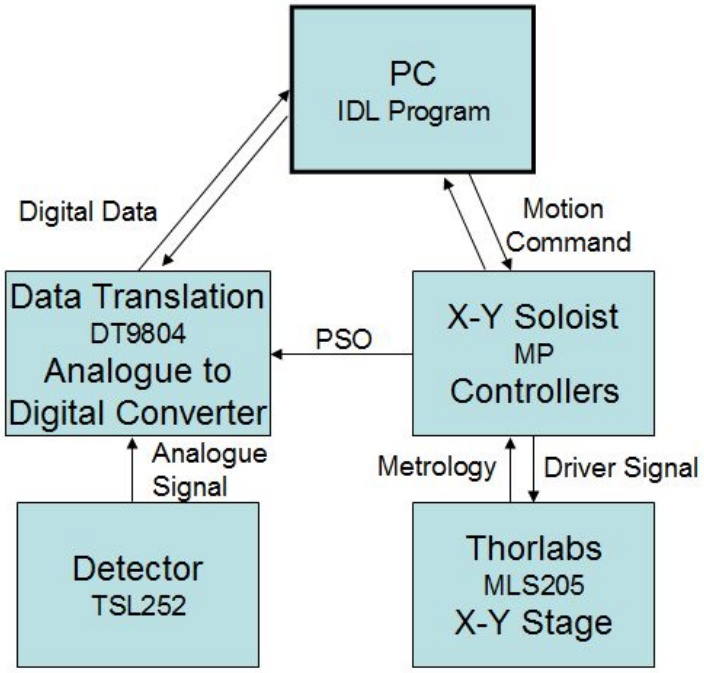

Figure 6.8: A box schematic showing the physical components and connections included in the optical imaging apparatus. The Data Translation devise is only connected to the PSO output of one axis at any time.

All the components of the system were integrated as shown in Figure 6.8. Programs to run the stage via the Soloist controller were written in IDL by myself using the existing IDL library. Figure 6.8 shows the analogue to digital converter module which converts the analogue signal into a readable digital format upon triggering by the PSO pulses. The analogue signal from the detector is digitized by the Data Translation DT9804 analogue to digital converter (ADC) data collection device triggered by the PSO signal produced by the Soloist controller [79]. In a typical sequence, having set the range and step size for the MLS203 stage motion, the motion controller starts the raster pattern, see Figure 6.10, and at each increment of motion generates a PSO pulse triggering the DT9804 ADC to collect a data point and store it in memory until the end of the motion. The digital data is subsequently retrieved by the software and saved in the image array.

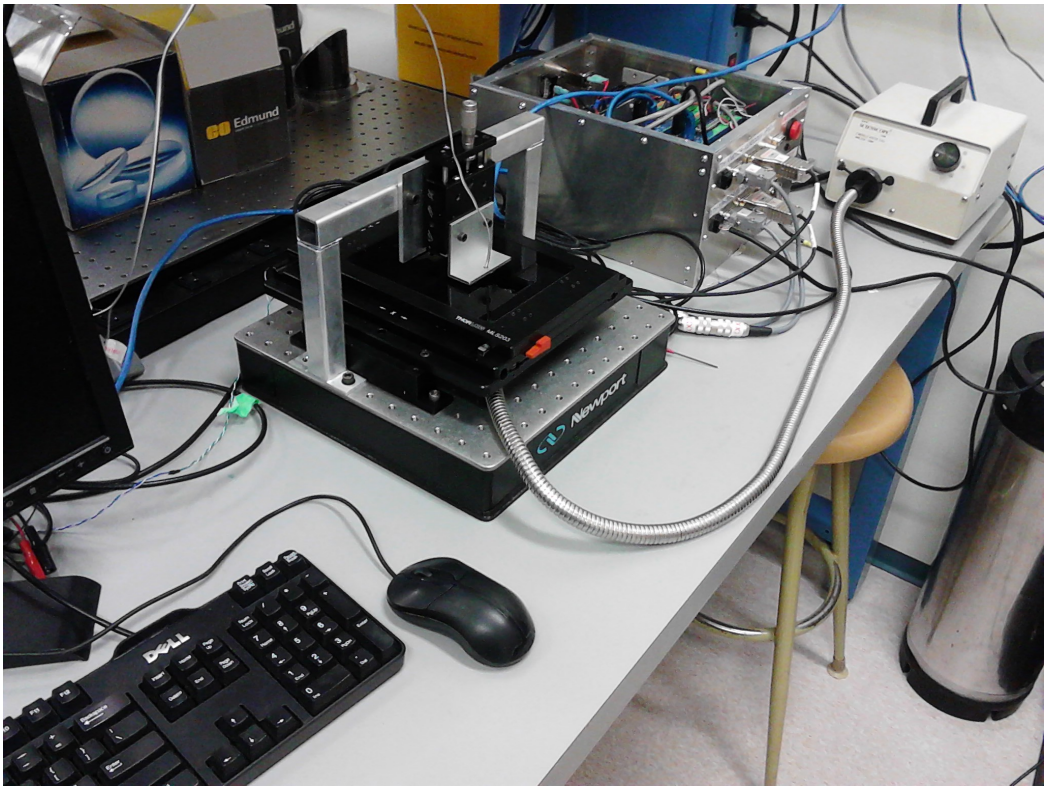

Figure 6.9: Image of the optical imaging system showing all components except the DT9804 ADC, which is sitting on the computer.

6.3.1 Stage Motion

One area in which significant improvement was expected, through transferring the knowledge of interferometry contained within the AIG, was to reduce the data acquisition time in two ways. First, the Thorlabs stage is light weight in both travelling axes which allows for high speed and acceleration. Second, the union of the Soloist controllers and the Thorlabs MLS203 X-Y stage enabled the use of the PSO option for data collection during stage motion, which was not possible with the Thorlabs controller.

For efficient data collection using the PSO, the stage was programmed to move in a raster pattern. This motion, depicted in Figure 6.10, consists of a long motion in the y-direction followed by a short motion in the x-direction and, subsequently, another long motion in the negative y-direction. By moving the stage in such a manor, data can be

	Parameters	Units
Acceleration X	1000	$\frac{mm}{s^2}$
Acceleration Y	2000	$\frac{mm}{s^2}$
Velocity X	99	$\frac{mm}{s}$
Velocity Y	145	$\frac{mm}{s}$
Pulse Width	10	μs

Table 6.1: Parameters used for translation stage motion and PSO pulse width for optical imaging.

collected during the long motions by utilizing the PSO triggering mechanism.

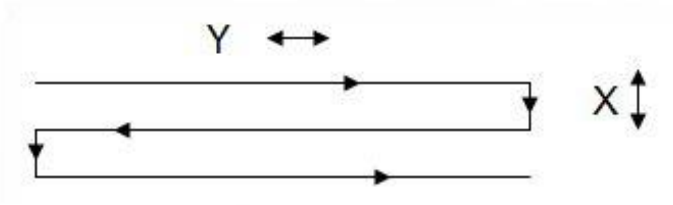

Figure 6.10: Example of the raster pattern that the stage goes through when taking images.

The MLS203 translation stage is a two axis stage in which the y-axis stage sits on top of the x-axis stage. The acceleration of the stage depends upon the force, which is determined by the current, and the mass of the stage. Since the x-axis stage carries approximately twice the weight that the y-axis stage carries, the acceleration response for a given force is roughly half for the x-axis stage as is it for the y-axis stage [80]. Since the current limit defined by the windings on the motor was 4 A, the y-axis stage was capable of greater acceleration than the x-axis stage because of the lower mass being displaced [75]. The maximum acceleration for each stage was set by default parameters within the Soloist while the stage velocity could be changed through the IDL software and are shown in Table 6.1.

6.3.2 Acquisition Programming

I developed the IDL program which controlled the stage motion and data acquisition. Within the program are parameters which control the stage, the PSO from the Soloist and the Data Translation DT9804 ADC. For the stage, the software allows for the image start

and end points of the y motion, the raster displacement in the x direction and the speed of the motion, see Figure 6.10, to be set by the user. For the PSO option, the width of the pulses (pulse width) and the distance the stage moves between pulses (pulse distance) must be defined. To ensure that PSO pulses are not missed, the pulse width in time must be less than the pulse to pulse period. It was found that 10 μs was sufficient to prevent pulse overlap. The pulse distance was set within the range of 10 - 100 μm to test the resolution capability of the apparatus.

Data acquisition with the DT9804 ADC involves collection of information while the stage is in motion, which is stored in internal memory buffers and can, subsequently, be downloaded into the software. The DT9804 ADC can be run in either continuous or finite mode, which affects how data are retrieved. In continuous mode it is important to set the buffer size and number of buffers so that there will be ample room allowed for data storage. After data collection are completed all data points can then be retrieved by the software regardless of whether the last buffer was filled. In finite mode this is not the case. The default buffer size, in finite mode, is 32 data points and the final buffer must be filled if all data points are to be available for retrieval. For this reason the distance that the stage travelled had to be adjusted such that the final number of data points were an integer multiple of 32. Once the data were collected and retrieved by the software they were saved '.sav' file for later processing.

6.4 Initial Optical Imaging Results

6.4.1 Image Capture Time

After the system was constructed and operational and the software had been written, the parameters were optimized to determine the minimum scanning time required to image a 10 mm x 10 mm area with a 100 μm sampling distance to allow direct comparison with the Chiu *et al.*, group. With the parameters from Table 6.1, we were able to acquire an image in 19.6 seconds. As can be seen from Table 6.2, this is three times faster than the most recent

Year	Time (sec)	Detector	Reference
2009	3000	Golay Cell	[16]
2011	90	Schoktty diode	[50]
2013	60	Schoktty diode	[26]
2014	60	Schoktty diode	[51]
2015	60	Schoktty diode	[52]
2015	19.6	Schoktty diode	Trimboli 2015

Table 6.2: Table recording the year of the paper, the time required to image a 10 mm x 10 mm area with 100 μm resolution, and the citation.

report from Chen *et al.* [51], and moreover, a full two orders of magnitude faster than their 2009 image acquisition time [16]. This justifies our assertion that an imaging system which can acquire an image in less time than was previously reported could be built.

6.4.2 Initial Images

The initial images acquired exhibited a strange pattern that was apparent in the direction of the y-axis motion of the MLS203 X-Y stage, see Figure 6.11 (a). Initially it was thought that this pattern was due to the Soloist not providing accurate PSO pulses as a function of velocity and acceleration. Although the AIG have years of experience working with Aerotech Soloist controllers and the PSO option in their work with Fourier transform spectrometers (FTS), these systems run relatively slowly, such that the acceleration phase is completed quickly and most data are acquired while the single axis stage is moving at a constant velocity. In the case of the microscope, since the imaging area is very small, 10 mm x 10 mm, the stage is accelerating through its entire motion. It was surmised that the PSO option was incapable of working under these conditions.

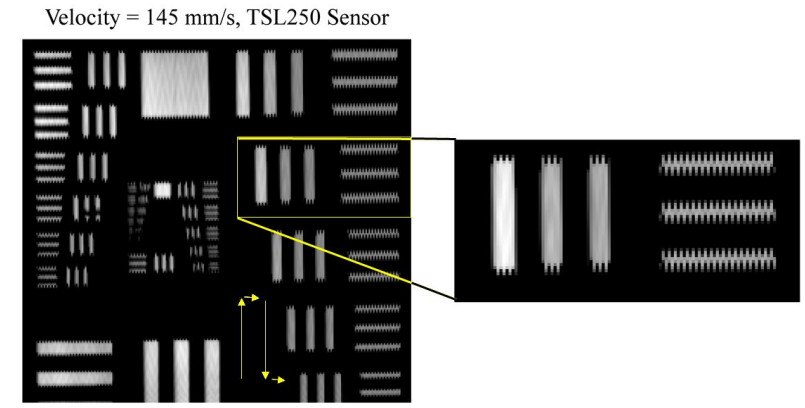

(a)

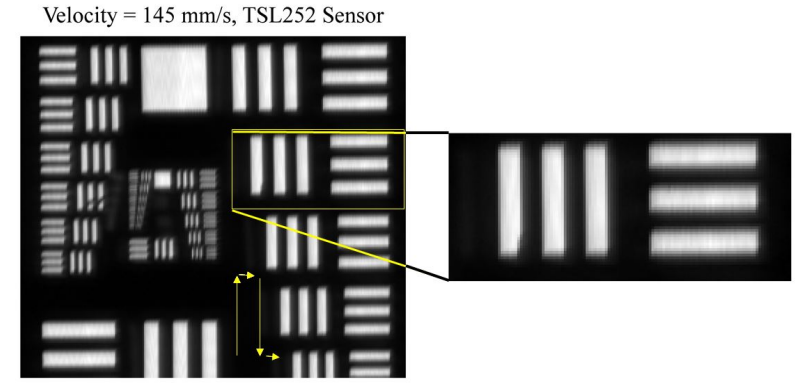

(b)

Figure 6.11: Example images of US Air Force calibration target taken with the TSL250 detector (a) and TSL252 detector (b). Note that the overshoot seen in (a) is not present in (b). This showed that the time constant was the cause of the overshoot. Red arrows show raster pattern motion.

To test the accuracy of the PSO, an oscilloscope was used to visually inspect the PSO pulses as a function of distance. Upon visual inspection, it was determined that the pulse rate varied according to the speed of axis travel as was expected. Images taken of an US Air Force calibration target, see Table 6.3 for specifications, showed artefacts that were thought to confirm that the PSO was not providing the accuracy required for our system [2]. Figure 6.11(a) shows the image of the calibration target exhibiting an apparent overshoot in the direction of y-axis motion that seemed to confirm the concern about the PSO. This

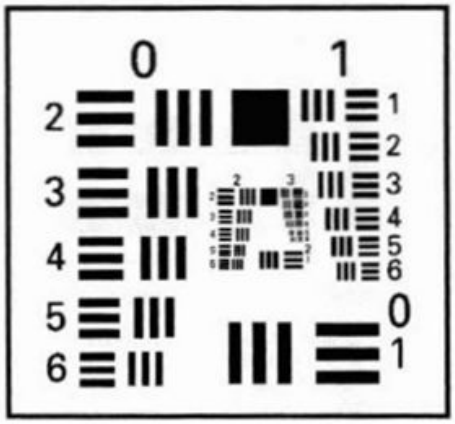

$\frac{lp}{mm}$[μm]	0	1	2	3
1	1.00 [500]	2.00 [250]	4.00 [125]	8.00 [63]
2	1.12 [446]	2.24 [223]	4.49 [111]	8.98 [56]
3	1.26 [397]	2.52 [198]	5.04 [99]	10.08 [50]
4	1.41 [355]	2.83 [177]	5.66 [88]	11.31 [44]
5	1.59 [314]	3.17 [158]	6.35 [79]	12.70 [39]
6	1.78 [281]	3.56 [140]	7.13 [70]	14.25 [35]

Table 6.3: Specifications for the US Air Force calibration target used for optical and THz imaging [2].

overshoot is not seen in the x-direction, which is the direction of lower velocity and could be explained by the PSO frequency lagging behind the stage during acceleration.

Since the PSO is integral to our system design it was decided to eliminate all other potential causes of the overshoot prior to removing the PSO from the design. One potential cause was the speed of response of the detector. Initially, a TSL250 silicon photo-diode made by Texas Instruments with identical rise and fall time constants of 360 μs [78] was used. Upon examination of the apparatus it was determined that the pulse frequency from the PSO at the maximum velocity of the stage was close to the time constant of this detector, see equation 6.3.

$$v = 145 \quad (\text{mm/s}) \quad (6.1)$$

$$d = 0.1 \quad (\text{mm}) \quad (6.2)$$

$$t = \frac{0.1}{145} = 0.0006897 \quad s \qquad = 690 \quad \mu s \tag{6.3}$$

This analysis shows that the total time constant for the photo-diode to rise and fall is 720 μs which is greater than the time between PSO pulses. Thus the lag of the photo-diode increases as the stage accelerates, resulting in the overshoot seen in the image, see Figure 6.11 (a). To test this conclusion the detector was replaced with a TSL252, another photo-diode of the same family, which has a total time constant of 14 μs (7 μs each for rise and fall). Figure 6.11 (b) shows the image acquired with the new detector. As can be seen, there is no longer any overshoot, confirming that detector speed was the issue rather than the PSO.

Chapter 7

Optical Image Processing

7.1 Introduction

THz imaging has significant potential as a tool for cancer diagnostics due to its ability to differentiate between cancerous and non-cancerous tissues [13]. Ashworth *et al.*, reported on the absorption coefficients of cancerous, fibrous (normal), and fatty breast tissue over the THz spectrum [6]. These authors showed that the greatest difference in the absorption coefficients of cancerous and fibrous tissue occurs $\sim$0.3 THz [6, 49]. The work of Chiu *et al.*, which uses radiation of 0.312 THz, see Section 3.5.2 and 6.2, was taken as a starting point for constructing a THz imaging system for breast cancer detection [16]. The system employs a plasmonic lens to increase transmission through a sub-wavelength aperture which improves the spatial resolution of the images so that it is sufficient for tumour margin determination, see Chapter 4.4. An optical analogue system, described in Chapter 6, was constructed for hardware and software development during the time required for designing, fabricating and testing of the plasmonic lens.

Single frequency THz imaging, discussed in Chapter 3, is an absorption imaging technique where the final intensity of the radiation is related to the thickness and absorption coefficient of the material through which the radiation passes. The incident and detected intensities (I_0 and I respectively) are related by the Beer-Lambert law

$$I = I_0 e^{-\alpha x} \tag{7.1}$$

where α is the absorption coefficient and x is the thickness of the sample [20]. Tissue differentiation can be accomplished by rearranging equation 7.1 to solve for α.

$$\alpha = -\frac{1}{x} ln(\frac{I}{I_0}) \tag{7.2}$$

Image acquisition by the optical imaging system is described in Section 6.3. The data acquired by the optical analogue imaging system were used for development of image processing software that would be used to analyse the data acquired by the THz system as well. In addition, computer generated image arrays, and digital images provided by Lucy Swift at the Cancer Cell Laboratory, headed by Dr. Roy Golsteyn from the University of Lethbridge, were used during software development as processing templates. This chapter will discuss the image processing steps required for cancer margin determination using the three types of images just described, an example of each is shown in Figure 7.1. All software was written by myself within the IDL environment and utilized the IDL library. Theory for this Chapter was taken from *Digital Image Processing* (3rd ed.) by Gonzalez and Woods [81].

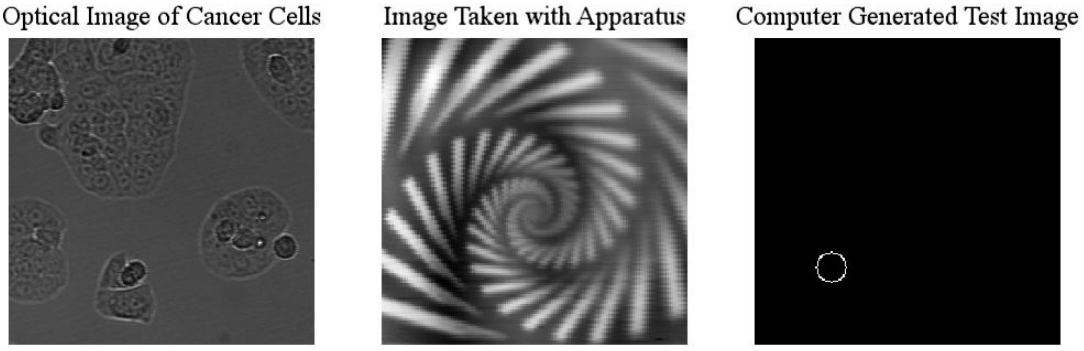

Figure 7.1: Examples of each type of image used while developing the image processing software. Left: Optical image of cancer cells taken with an optical camera, provided by the Cancer Cell Laboratory. Middle: Image taken with imaging apparatus. Right: Computer generated example image.

7.2 Processing Steps

Analysis of THz images requires that the image be ingested into the software, smoothed to remove noise from the imaging system, thresholded to remove any zero or negative values, and be transformed into absorption coefficient space. At this point edge detection techniques to determine tissue boundaries must be applied. These processing steps have been simplified for ease of explanation, though the imaging system is more fully described in Section 8.2 and requires that reflection due to boundaries and absorption due to all materials be considered. Images provided by the Cancer Cell Laboratory were large, so cropping was used to achieve an image of a similar size to those that would be obtained by the THz imaging apparatus.

Image Ingestion

Since several image formats were used while developing the image analysis software, the software was written to be flexible and allow ingestion of a range of different image formats into the IDL programming. Optical imaging data acquired with the optical imaging system were saved in an IDL '.sav' file format making ingestion simple. The images provided by Dr. Golsteyn's lab were of two different file formats, gif or jpeg. Since these are not IDL file types, they must be ingested using functions from the IDL library and converted from a 24-bit colour image to grey-scale.

Cropping

After the provided image has been ingested into IDL, the region of interest must be selected. For the small images taken with our apparatus, or generated by the program, the entire image is the region of interest. For larger images, such as those produced by Dr. Golstyen's lab, a smaller sub-area of the image array, encompassing the region to be studied, is selected and copied into another array of appropriate size. This is known as cropping, see Figure 7.2a and 7.2b.

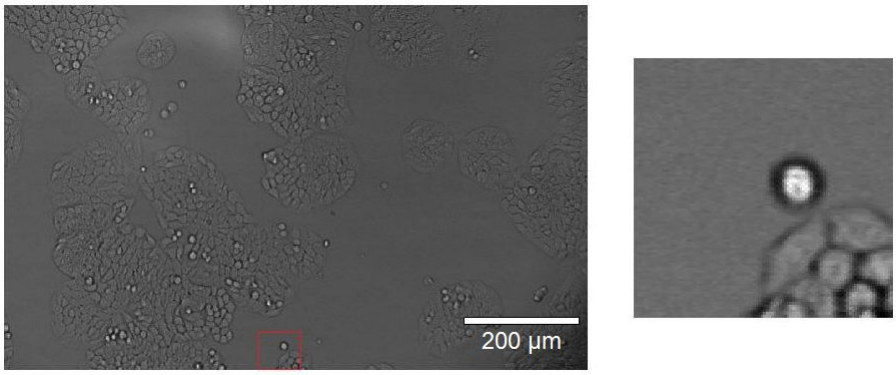

Figure 7.2: Left: Image provided by Cancer Cell Laboratory. Red boxed area is the cropped section shown in Right image.

Thresholding

Once the image has been cropped down to the region of interest the resulting image can be analysed. Before the logarithm can be taken of the image, to bring it into absorption coefficient space, any pixels that are negative or zero valued must be removed. The process of removing any potential problem elements in the image array is called thresholding, since it can be applied with user defined upper and lower limits.

Smoothing

Smoothing is used to improve the signal to noise ratio by removing extraneous noise from the initial image. There are several methods that can be used for smoothing the image which will be discussed in Section 7.3.1.

Coefficient Space

After the image is thresholded and smoothed, the entire image, expressed in the Cartesian plane as $I(x,y)$, is divided by the initial intensity of the source, I_0, and the logarithm taken. After which, all that is required to bring the image into coefficient space is to divide by the thickness of the sample. With the image in coefficient space, it is now possible to use edge detection techniques to find the boundaries of the different tissue types. The goal

is to determine the presence of cancerous tissue according to absorption coefficient range.

7.3 Image Filtering

Image filtering, which encompasses both smoothing and edge detection, can be accomplished in either the spatial or frequency domain. Spatial filtering involves convolving the filtering kernel with the image. Convolution is defined as

$$w(x,y) \star I(x,y) = \sum_{s=-a}^{a} \sum_{t=-b}^{b} w(s,t) I(x-s, y-t) \tag{7.3}$$

where $w(x,y)$ is the spatial filtering kernel and $I(x,y)$ is the image being filtered [81].

Frequency filtering requires that the image be first Fourier transformed into frequency space. The Fourier transform is defined as

$$\mathscr{I}(\mu,\nu) = \frac{1}{\sqrt{2\pi}} \int_{-\infty}^{\infty} \int_{-\infty}^{\infty} I(x,y) e^{-i(\mu x + \nu y)} dx dy \tag{7.4}$$

where $I(x,y)$ is the image [81]. The inverse transform, which returns the image to the spatial domain, is defined as [81]

$$I(x,y) = \frac{1}{\sqrt{2\pi}} \int_{-\infty}^{\infty} \int_{-\infty}^{\infty} \mathscr{I}(\mu,\nu) e^{-i(\mu x + \nu y)} d\mu d\nu. \tag{7.5}$$

The convolution theorem, from Fourier analysis, states that convolution in one domain is equivalent to multiplication in the corresponding domain [72].

$$\mathscr{F}[f \star g] = \mathscr{F}[f] \mathscr{F}[g] \tag{7.6}$$

Once Fourier transformed, the data contained in the image is expressed in terms of amplitudes and spatial frequencies rather than spatial position and intensity. For example, low frequencies in frequency domain correspond to broad regions in the spatial domain and

high frequencies to narrow. Frequency domain filtering allows for particular frequencies, or range of frequencies (ie. band pass filtering), to be filtered out of the image. Since the THz image will be taken by using raster motion by the imaging apparatus, see Section 6.3.1 for further explanation, there is the potential of frequency artefacts being left in the image. These artefacts can be removed by using frequency filtering on the image.

7.3.1 Smoothing

The algorithms used for smoothing an image differ depending on whether accomplished in the spatial or frequency domain.

Spatial Averaging

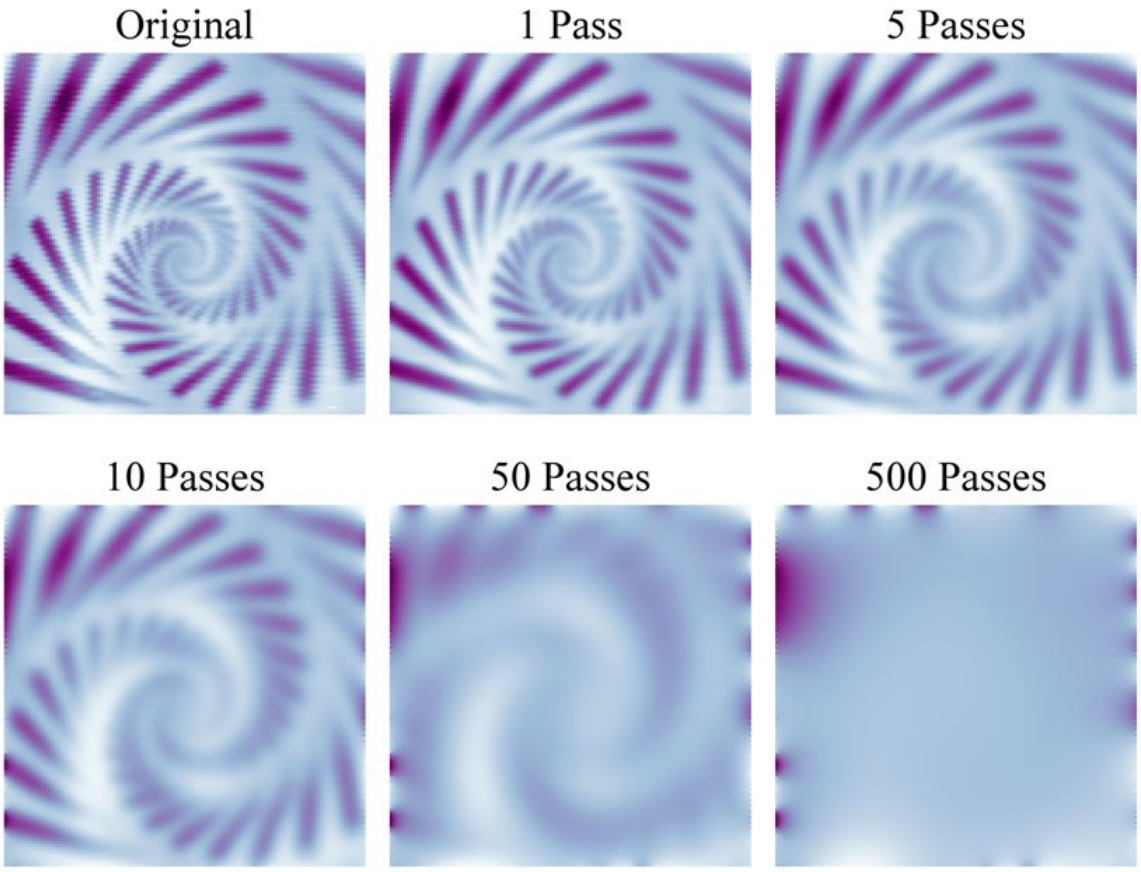

Figure 7.3: Figure showing the effect of a 3x3 spatial averaging filter on an image when applied multiple times. Edge effects may be ignored.

In the spatial domain, smoothing involves the application of an averaging filter to the image. As can be seen from Figure 7.3, the use of an averaging filter removes the sharp edges from the image. Repeated use of such a filter will result in each pixel in the image assuming the mean value of the image, as shown in the bottom right-hand image in Figure 7.3. An example of a 3 x 3 averaging filter is written as

$$\begin{aligned} R(x,y) = &\frac{1}{9}[I(x-1,y-1)+I(x,y-1)+I(x+1,y-1) \\ &+I(x-1,y)+I(x,y)+I(x+1,y) \\ &+I(x-1,y+1)+I(x,y+1)+I(x+1,y+1)] \end{aligned} \tag{7.7}$$

$R(x,y)$ is subsequently set equal to $I(x,y)$ and the process is repeated through the entire image [81]. Larger averaging filters will cause this effect to occur much more quickly.

Edge Effects

When applying any filter in the spatial domain, one must be careful not to cause aliasing [81]. This occurs when a filter is improperly applied to the edge of an image. Take a 3x3 smoothing matrix as an example, see Figure 7.3. If the smoothing filter is applied incorrectly, then zeros will be assumed for the pixels not in the image that must be included when taking the average for an edge pixel. To apply the filter properly, this must be taken into account by use of techniques such as assuming the image is periodic or by truncating the edges such that the edge of the filter never moves beyond the edge of the image.

Low-Pass Filter

Smoothing can also be accomplished in frequency space. Since, low frequencies correspond to the broad regions of a spatial domain image removing high frequencies corresponds to smoothing of narrow features in the image when displayed in the inverse transform. In my analysis, three frequency domain filters were investigated: ideal, Butterworth and Gaussian. Each are explained below.

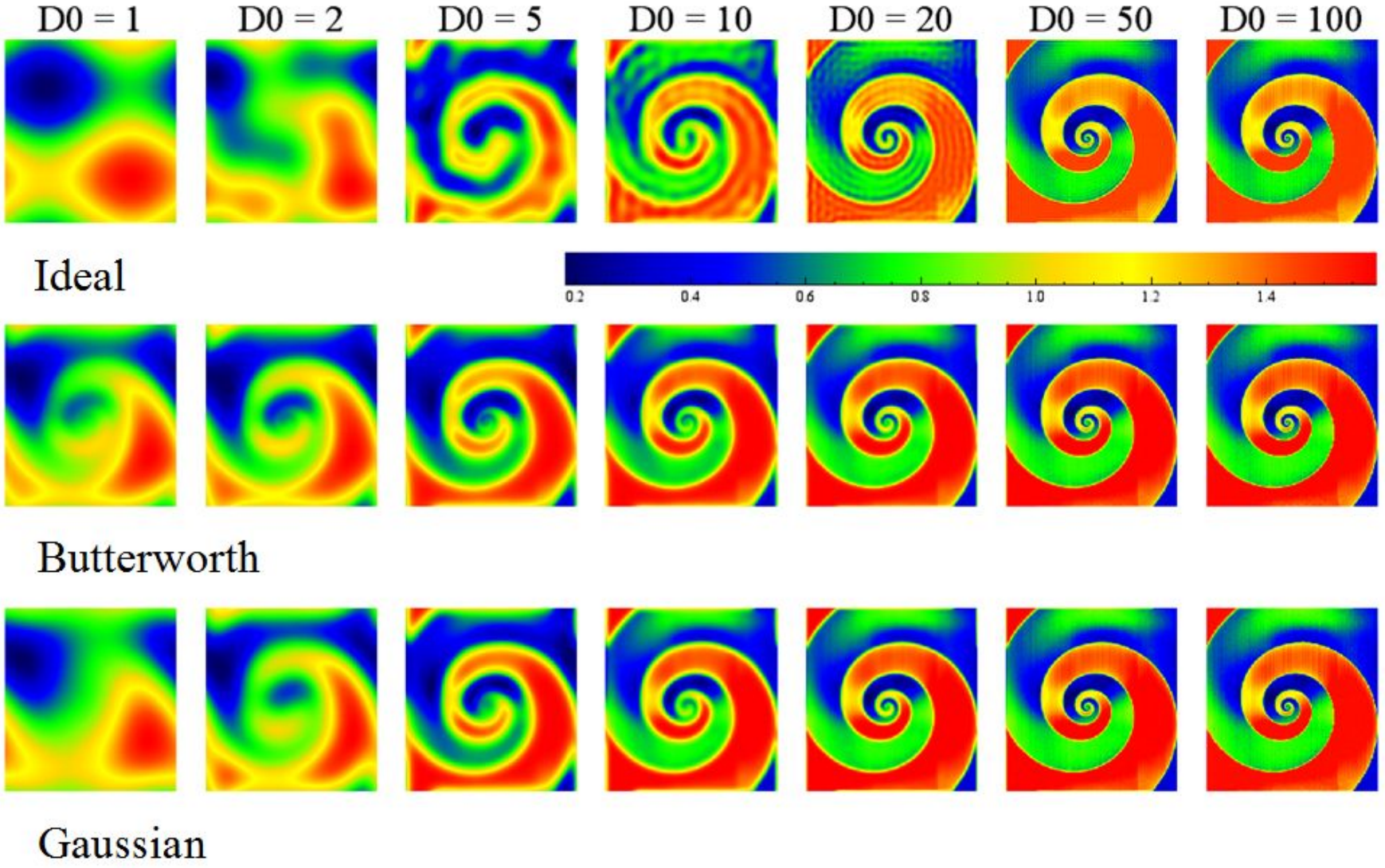

Figure 7.4: Figure showing the effect of ideal (top row), Butterworth (middle row), and Gaussian (bottom row) low-pass filters. The columns show how the filters effect changes as the cut-off frequency (D_0) increases. A small D_0 causes significant smoothing of the image, as can be seen in the $D_0 = 0$ column. The effect of the low-pass filter decreases and the cut-off value increases and more frequencies are passes by the filter.

Ideal Filter The ideal filter is expressed mathematically as

$$L(\mu,\nu) = 1\, if\, D(\mu,\nu) \leq D_0 \tag{7.8}$$

$$L(\mu,\nu) = 0\, if\, D(\mu,\nu) \geq D_0 \tag{7.9}$$

where

$$D(\mu,\nu) = [(\mu - \frac{P}{2})^2 + \nu - \frac{Q}{2})^2]^{\frac{1}{2}}, \tag{7.10}$$

D_0 is the cut-off frequency of the filter and P and Q are the dimensions of the image [81]. This filter is a two dimensional Heaviside-step function centred at the frequency cut-off, D_0, and is very easy to implement. The ideal filter was inappropriate for THz image processing due to the artefacts that are introduced by its use.

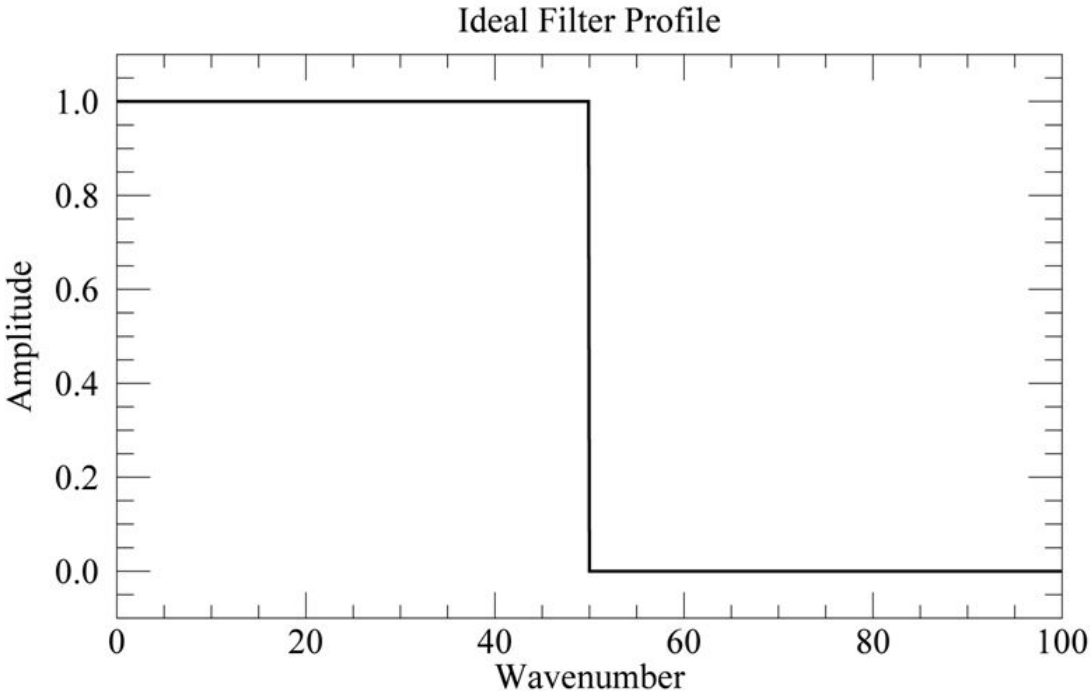

Figure 7.5: Profile of a one dimensional ideal filter with at frequency cut-off (D_0) at 50 wavenumbers. To expand this into two dimensions one need to have the boundary form a circle of radius D_0 with the origin as the center.

The Fourier transform of a rectangular function, $\Pi(x)$ is a Sinc function [82].

$$\mathscr{F}[\Pi(x)](\mu) = sinc(\pi\mu) = \frac{sin(\pi\mu)}{\pi\mu} \tag{7.11}$$

The profile for the sinc function is

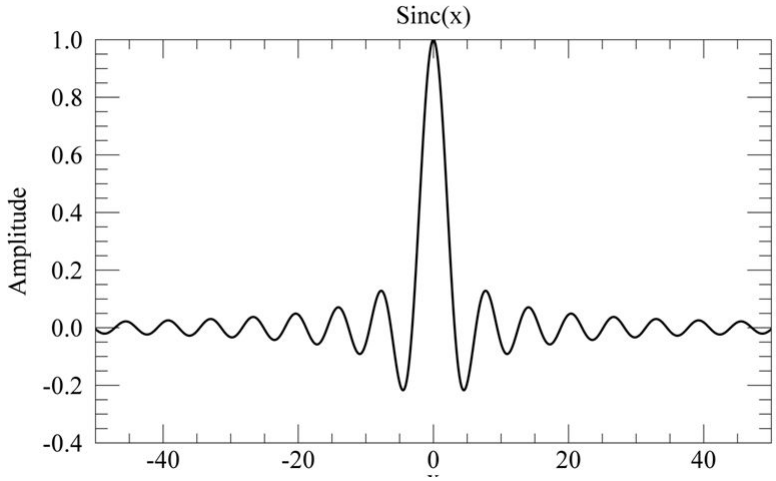

Figure 7.6: Profile of the Sinc(x) function, which results from the Fourier transform of the rectangle function.

The oscillations caused by the convolution of the sinc function with the image results in 'ringing', see Figure 7.4 image D0 = 20, which is the reason that this filter finds limited use.

Butterworth Filter The Butterworth filter is defined as

$$L(\mu,\nu) = \frac{1}{1+[\frac{D(\mu,\nu)}{D_0}]^{2n}} \tag{7.12}$$

where $D(\mu,\nu)$ is the same function used for the ideal filter, D_0 is the cut-off frequency and n is the order of the function [81]. This filter is useful because it does not produce as significant 'ringing' as the ideal filter. Moreover, the slope can be adjusted by the user through changing the order (n) of the filter, see Figure 7.7(b), which allows for a sharper

cut-off than is possible with the Gaussian filter, discussed in the next Section.

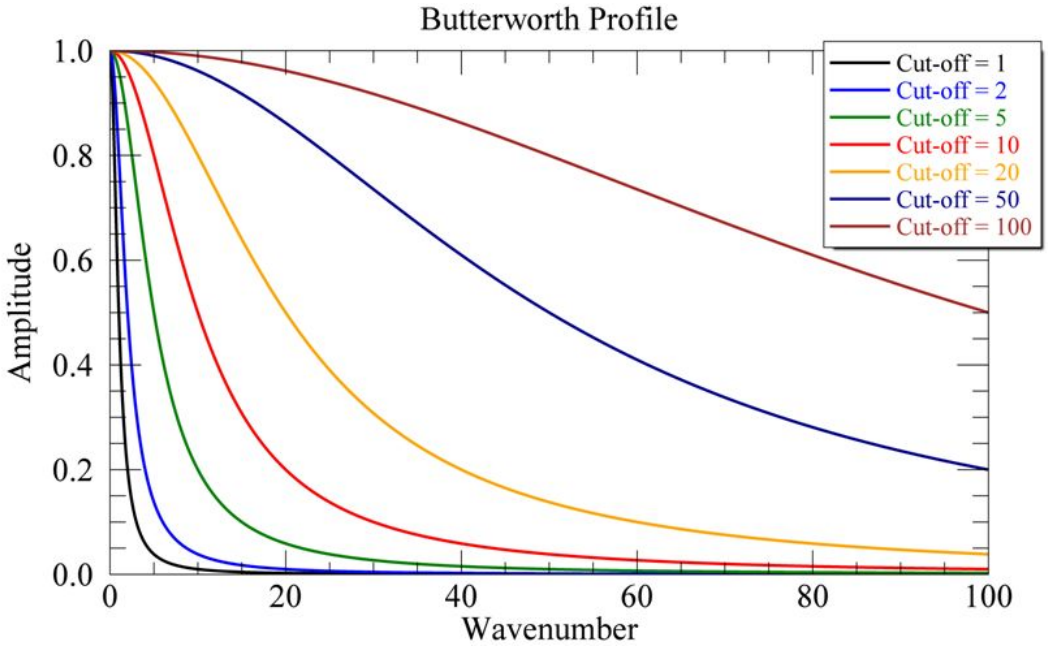

(a)

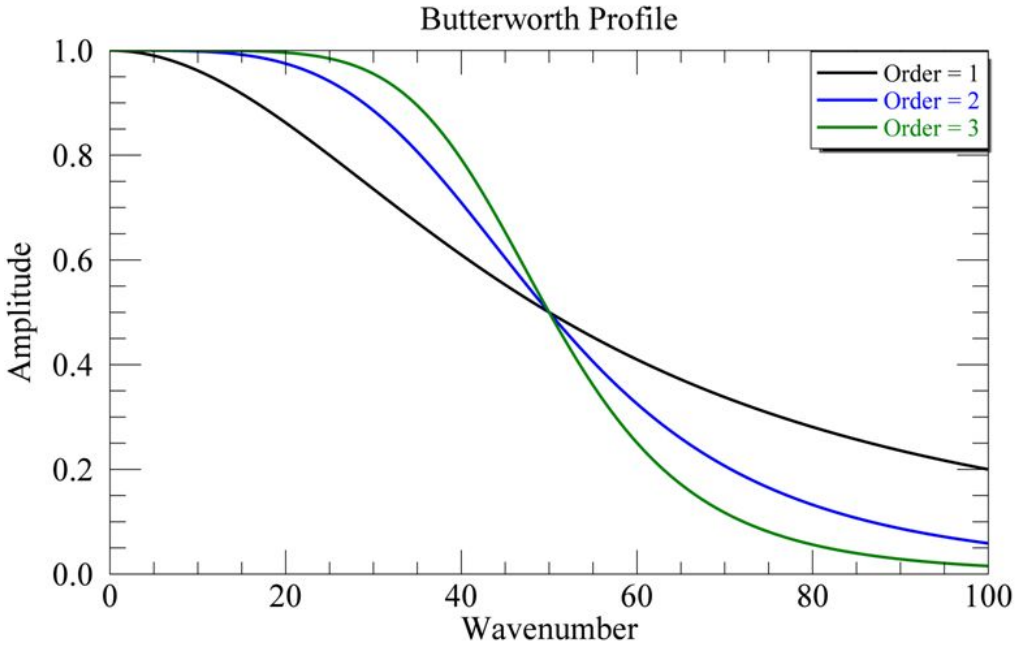

(b)

Figure 7.7: (a) Example of the Butterworth profile with D_0 = 1, 2, 5, 10, 20, 50, and 100. (b) Butterworth filter profiles for n = 1 ,2, and 3. As is shown, the angle of the curve depends upon both the cut-off frequency and the order of the function.

The images shown in Figure 7.4 were produced using the first order Butterworth filter. As can be seen when comparing with the other filters which were used for Figure 7.4, the Butterworth has a softer effect on the image when D_0 is small, but gives comparable results when D_0 is large.

Gaussian Filter The Gaussian filter applies a two-dimensional Gaussian profile as the boundary used for frequency removal. It is defined as

$$L(\mu, \nu) = e^{-\frac{D^2(\mu,\nu)}{2D_0^2}} \tag{7.13}$$

where $D(\mu, \nu)$ is the same function as was used for the ideal filter, and D_0 is the cut-off frequency [81]. In this case, D_0 acts as the standard deviation of the function, which defines the width of the distribution.

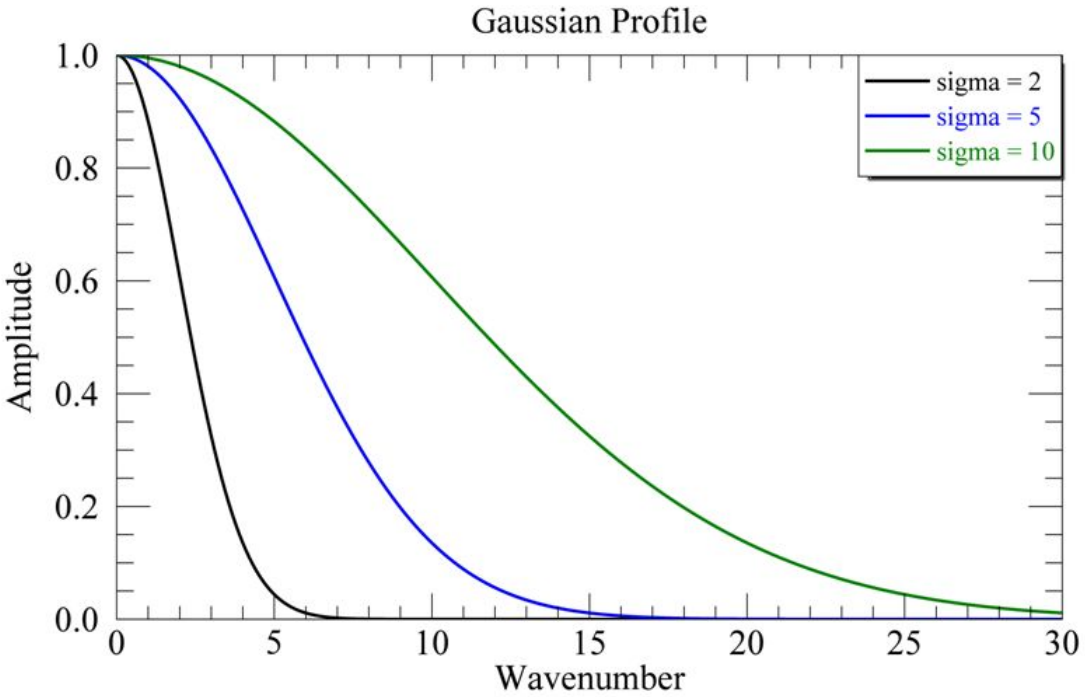

Figure 7.8: Gaussian low-pass filter profile for frequency cut-off (D_0= sigma) of 2, 5, and 10.

Unlike other filters used for frequency domain filtering, the Gaussian filter does not cause 'ringing' in the image or other artefacts. This is because the Fourier transform of a Gaussian function is also a Gaussian function. Instead of being a very sharp transition, the Gaussian filter removes unwanted frequencies with a smooth Gaussian shaped transition, see Figure 7.8.

7.3.2 Edge Detection

To differentiate tissue types, the edges of the regions with absorption coefficients within the correct boundaries must be ascertained. Several methods of edge detection were explored while developing the image processing software. Like smoothing filters, edge detection filters can be applied in either the spatial or the frequency domain.

Derivatives

In the spatial domain, edge detection involves the use of derivatives. In image processing, the standard first order derivative, $\frac{\partial f(x)}{\partial x}$, is written as

$$\frac{\partial f(x)}{\partial x} = f(x+1) - f(x) \tag{7.14}$$

and the second order derivative is written as

$$\frac{\partial^2 f(x)}{\partial x^2} = f(x+1) + f(x-1) - 2f(x). \tag{7.15}$$

Since images are two dimensional, the derivative must be taken in both dimensions. The four methods explored for finding the first derivative while developing the software were: gradient, Roberts, Prewitt and Sobel. The Laplacian was also implement to show the effects of taking the second derivative. These methods are described mathematically as [81]:

Gradient

$$R(x,y) = |I(x+1,y) - I(x,y)| + |I(x,y+1) - I(x,y)|. \tag{7.16}$$

Roberts

$$R(x,y) = |I(x+1,y+1) - I(x,y)| + |I(x,y+1) - I(x+1,y)|. \tag{7.17}$$

Prewitt

$$\begin{aligned} R(x,y) =& |[I(x-1,y+1) + I(x,y+1) + I(x+1,y+1)] \\ & -[I(x-1,y-1) + I(x,y-1) + I(x+1,y-1)]| \\ & +|[I(x-1,y+1) + I(x,y+1) + I(x+1,y+1)] \\ & -[I(x-1,y-1) + I(x,y-1) + I(x+1,y-1)]| + \\ & +|[I(x+1,y-1) + I(x+1,y) + I(x+1,y+1)] \\ & -[I(x-1,y-1) + I(x-1,y) + I(x-1,y-1)]|. \end{aligned} \tag{7.18}$$

Sobel

$$\begin{aligned} R(x,y) =& |[I(x-1,y+1) + 2I(x,y+1) + I(x+1,y+1)] \\ & -[I(x-1,y-1) + 2I(x,y-1) + I(x+1,y-1)]| \\ & +|[I(x-1,y+1) + 2I(x,y+1) + I(x+1,y+1)] \\ & -[I(x-1,y-1) + 2I(x,y-1) + I(x+1,y-1)]| + \\ & +|[I(x+1,y-1) + 2I(x+1,y) + I(x+1,y+1)] \\ & -[I(x-1,y-1) + 2I(x-1,y) + I(x-1,y-1)]|. \end{aligned} \tag{7.19}$$

Laplacian

$$R(x,y) = I(x+1,y) + I(x-1,y) + I(x,y+1) + I(x,y-1) - 4I(x,y). \tag{7.20}$$

To determine which method would be most useful for edge detection, each of these filters were applied to several images of different types, as is shown in Figure 7.9, which include computer generated (top row), optical data obtained by the analogue imaging system (middle row) and JPEG image provided by the Cancer Cell Laboratory (bottom row). Colour was added to the images to enhance the differences between the edge detection

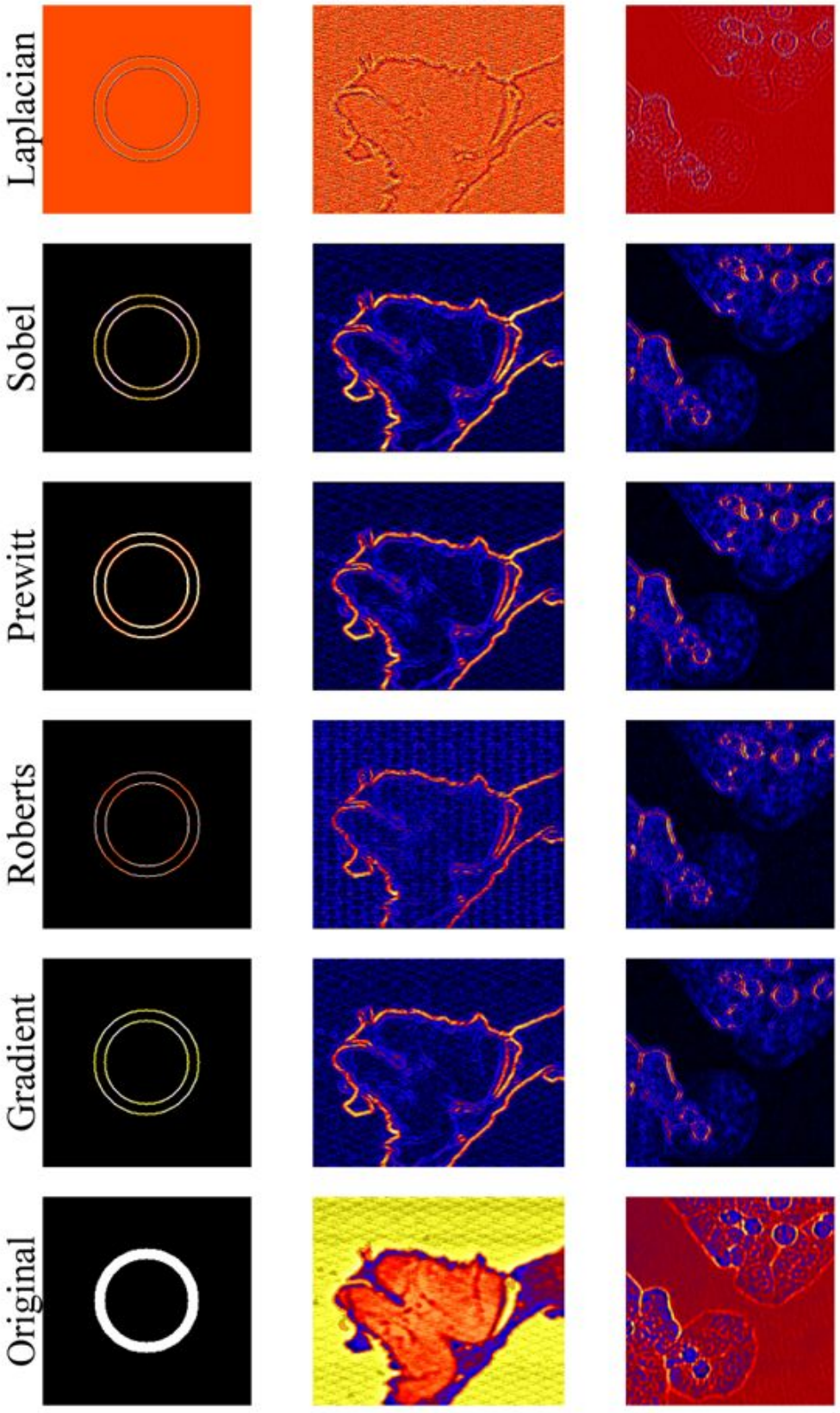

Figure 7.9: Figure showing the effect of the gradient, Roberts, Prewitt, Sobel and Laplacian on spatial edge-detection filters on three different image types. The top row is a computer generated ring. The middle row is an optical image of a paraffin embedded rat brain sample cut and mounted by myself at Dr. Jeff Dunn's lab at the University of Calgary. The bottom row is JPEG image of living cancer cells provided by Dr. Roy Golsteyn's lab.

techniques. As can be seen, the Roberts technique transfers the most noise, while the Sobel allows for the greatest definition with the least noise (this is most obvious from the middle row and the definition of the rat brain) [81].

High-pass filter

The ideal, Butterworth and Gaussian low-pass filters, described in Section 7.3.1, can be converted into high-pass filters by simply defining a new function [81].

$$H(\mu,\nu) = 1 - L(\mu,\nu) \tag{7.21}$$

As the name suggests, high-pass filters allow the high frequency components of the image to remain while filtering out the low frequencies. Figure 7.10 shows the application of the three frequency domain high-pass filters. As can be seen, the edges become much more defined as the cut-off frequency increases due to the removal of all low frequencies from the images, leaving only the sharp transitions.

Of the three Fourier filters which were investigated, it was determined that the ideal filter caused significant artefacts in the images after its use. Between the Butterworth and Gaussian filters, while the Butterworth filter allows for a greater range options for the abruptness of the boundary used, for this application the Gaussian filter was determined to be the best since it does not introduce artefacts to the final image. The Sobel filter was used for edge detection, for the reasons previously stated, and the Gaussian low-pass filter was used for smoothing in the final image processing software.

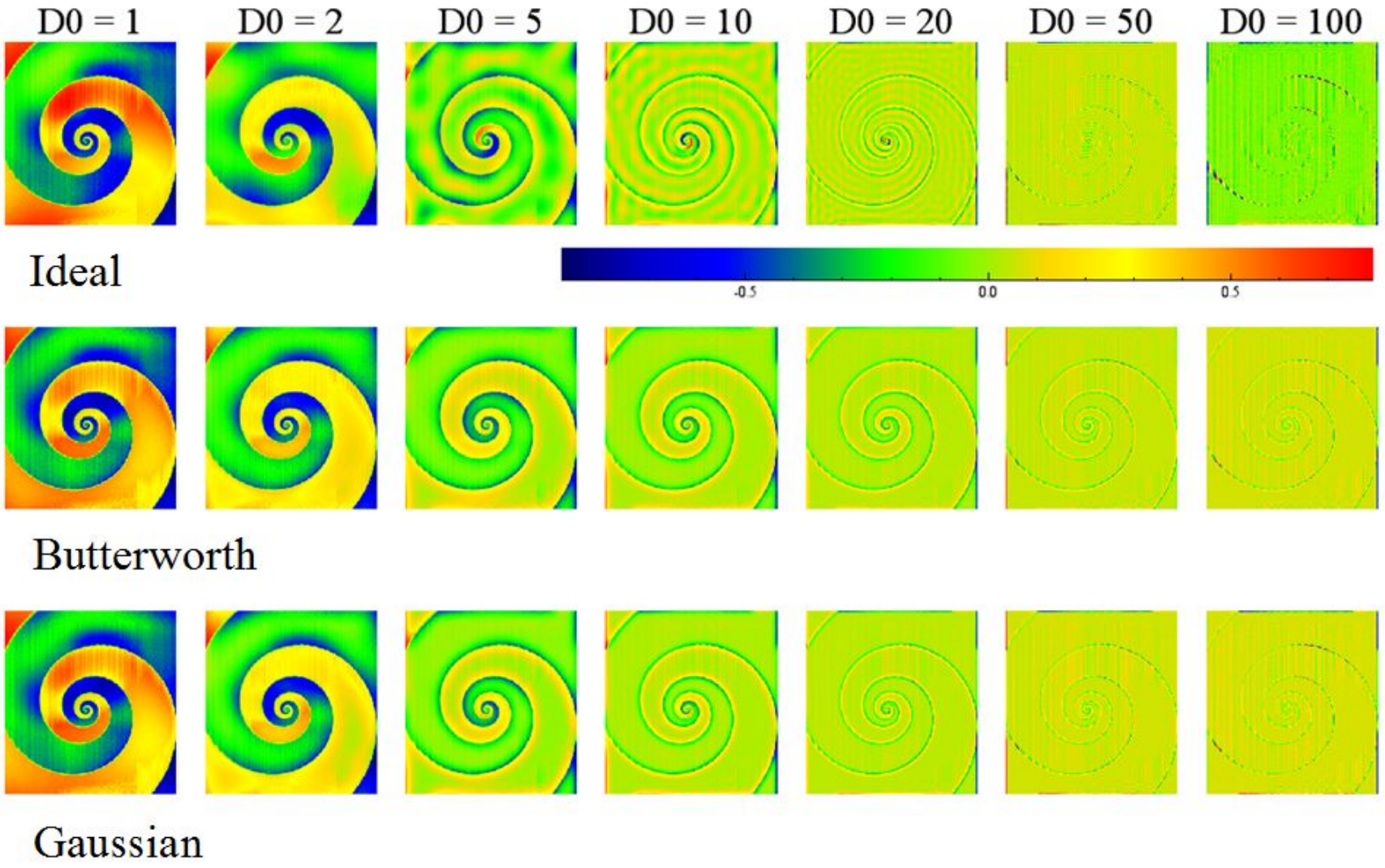

Figure 7.10: Figure showing the effect of ideal (top row), Butterworth (middle row), and Gaussian (bottom row) high-pass filters on a white circle in a black background.

Chapter 8

TeraHertz System and Results

8.1 Introduction

As discussed in Chapter 3, the region around 0.3 THz shows a significant difference in the absorption coefficients of cancerous and non-cancerous breast tissue [6, 49]. To be useful to a pathologist, any method of detecting cancer must have sufficient spatial resolution for margin determination. Since spatial resolution is generally about the order of the wavelength of light, it is poor at THz frequencies [20]. Use of a sub-wavelength aperture in the near-field can improve spatial resolution making it dependent upon the aperture diameter rather than the wavelength, but this comes at a cost of low transmission. By the use of a plasmonic lens, however, transmission can be enhanced making THz imaging more feasible.

For this project, a THz imaging apparatus was designed for breast cancer detection. Unfortunately, due to time constraints, we were not able to image human tissue samples. However, measurements were made to determine the spatial resolution and sensitivity that will be attainable with the system. Spatial resolution was verified by analysing THz images of the US Air Force calibration target, see Section 6.3 for specifications [2]. Specificity was determined by analysing THz images of distilled water to determine its absorption coefficient, α, and an estimate the uncertainty on α, and THz images of a plain glass coverslip to determine the signal-to-noise ratio of the system. In addition to this, THz images of paraffin embedded rat brain, sectioned and mounted by myself at Dr. Jeff Dunn's lab at the University of Calgary, were acquired and used for boundary determination in absorption

coefficient space using the software developed in Chapter 7, as well as analysed for spatial resolution.

8.2 THz System Design

The work of Chiu *et al.*, (Section 3.5.2), along with the original designs provided by our industrial partner Blue Sky Spectroscopy Inc., and the specifications of the Thorlabs stage (Section 6.2.1) and plasmonic lens (Section 4.4) were used in the design of the THz imaging system to optimize its performance [16]. Similar to the analogue optical imaging system, see Chapter 6, which was developed for troubleshooting and software development, the main components of the THz imaging system consist of a source, defining aperture, two-axis translation stage and detector. Figure 8.1(a) shows the basic configuration of these components, while Figure 8.1(b) shows the CAD drawing of the system which was made prior to fabrication and integration.

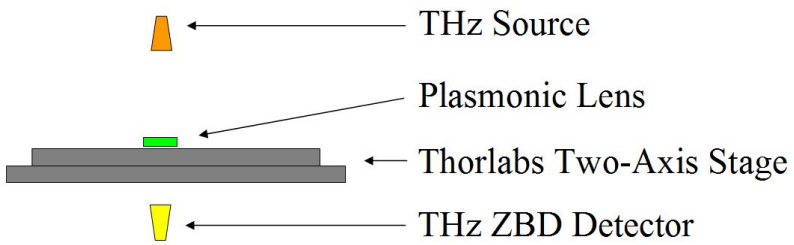

(a)

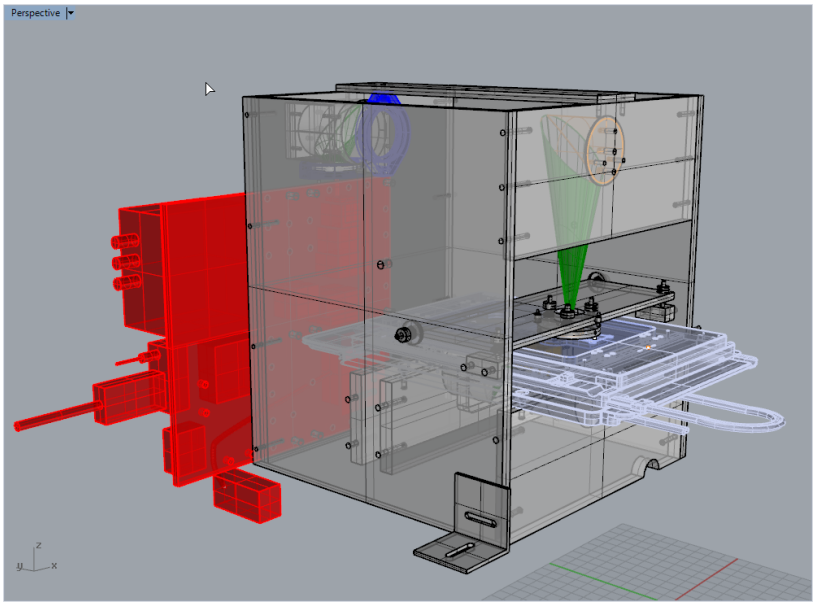

(b)

Figure 8.1: (a) Schematic showing the four main components of the THz imaging system: THz source, plasmonic lens, two-axis stage and THz ZBD detector. (b)Design of the THz system initially drawn in CAD software. Design shows the positions of the THz source (coloured red), the plasmonic lens holder, the two-axis stage, the 90^o off-axis parabolic mirrors and the quarter wave plate. The lower 90^o off-axis parabolic mirror, a second quarter wave plate, and the zero-bias detector are included in the drawing, but are not visible from this perspective as they are hidden by the two-axis stage.

The THz source used was the same Virginia Diodes Inc. (VDI) line source which was used for the THz knife edge test measurements, see Section 5.5.1 [73]. The beam profile of the source was predominately Gaussian and was frequency tunable within 0.32 - 0.33 THz

(wavelengths of $908 - 937$ μm). The source was modulated with a 5 KHz square wave and the signal detected by a lock-in amplifier to increase the sensitivity of the measurements [1]. The THz source had a maximum power output of $\sim$ 10 mW, although power output was frequency dependent (see Heggie 2014 [1] for more information about the line source). As is shown in both Figure 8.1(b) and Figure 8.2, the VDI line source was mounted such that the beam propagated vertically upwards.

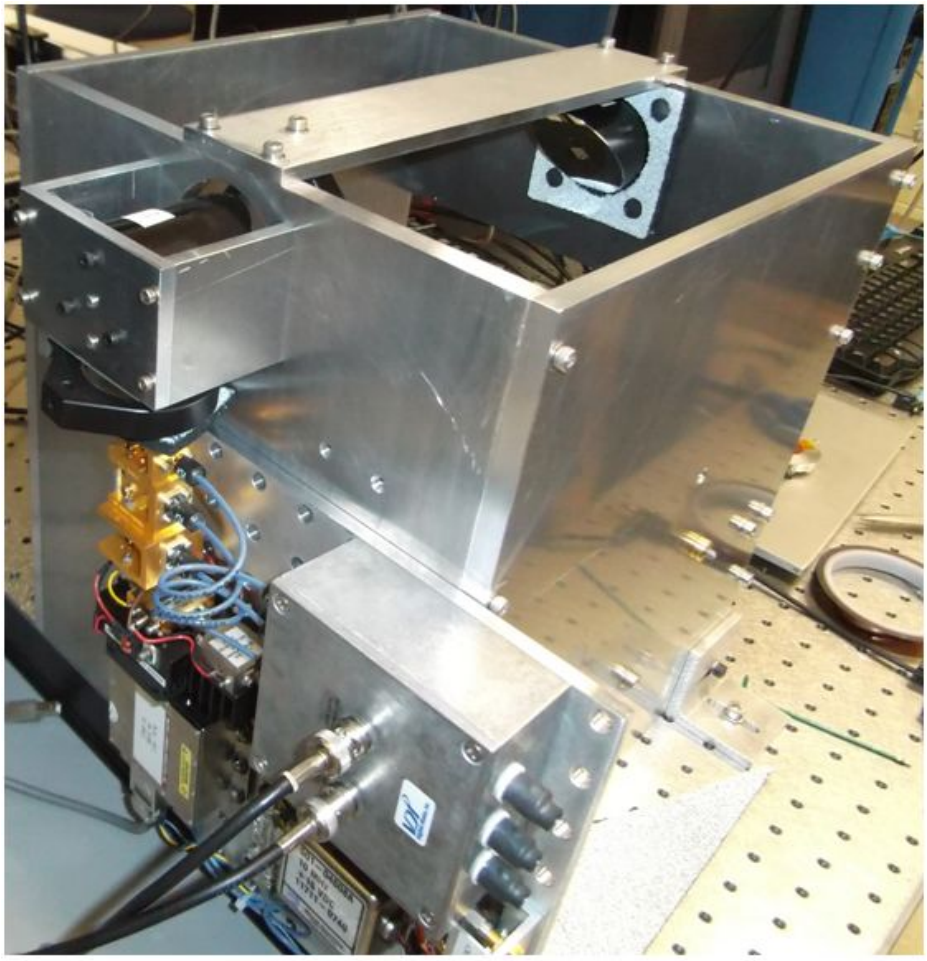

Figure 8.2: Image showing the position of the THz line source mounted vertically along the side of the THz imaging system.

The horn of the VDI source was placed at the focus of an 90^o off-axis parabolic (OAP) mirror (f/1) [83]. The horizontally polarized beam first travels through a wire polarizer, which helps to mitigate resonant cavities and reduce the effect of standing waves which in-

troduce artefacts in the system, before being collimated by the first OAP (f/1). After the first OAP (f/1), the resulting collimated beam propagates through a quarter wave plate (QWP) which changes the polarization of the beam from horizontally to circularly polarized. The first OAP (f/1) is paired with a second OAP (f/3) which reflects and focuses the beam down onto the plasmonic lens in such a way as to illuminate several rings.

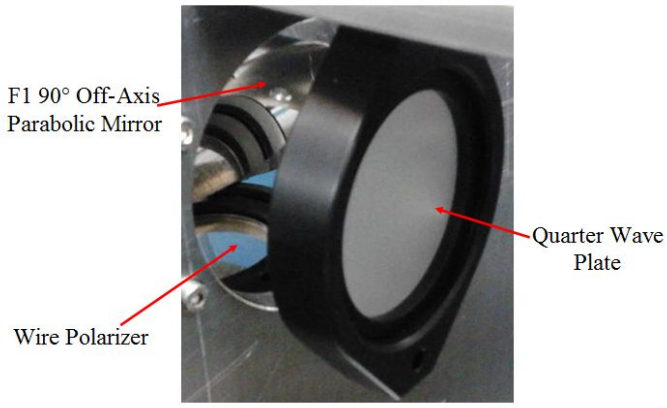

Figure 8.3: Image of the configuration of the initial OAP (f/1) along with the QWP and the wire polarizer.

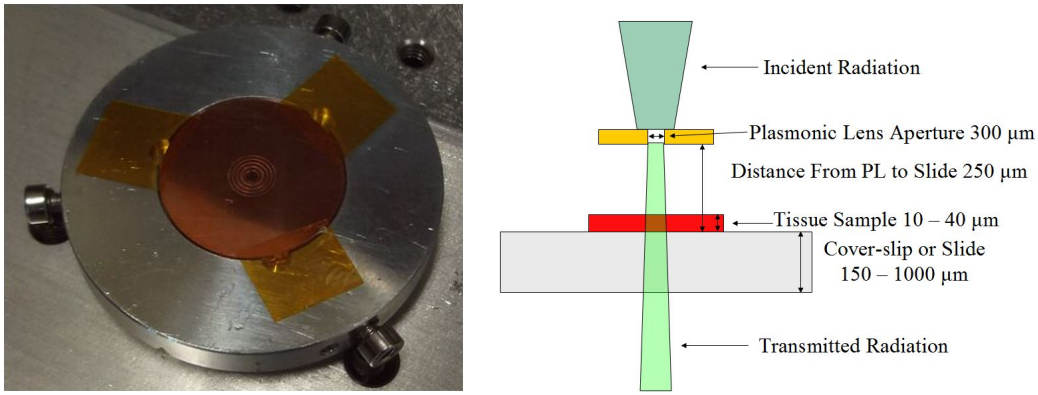

(a) (b)

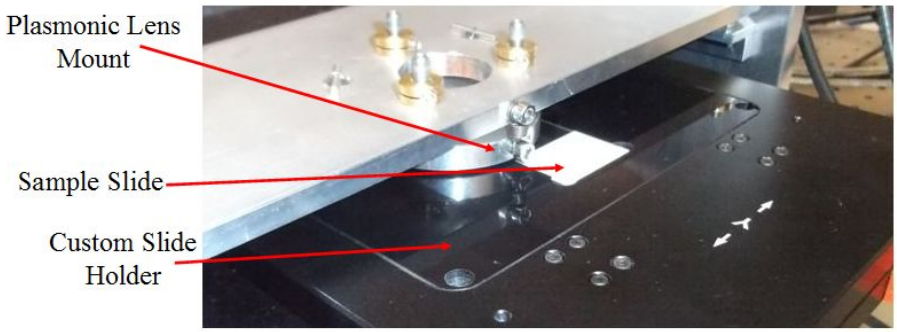

(c)

Figure 8.4: (a) Image showing plasmonic lens in its mount. (b) Diagram of the THz illumination set-up showing dimensions of the plasmonic lens aperture, sample, and cover-slip. (c) Image showing the plasmonic lens mounting mechanism and approximate distance from the two-axis stage and slide holder required for THz imaging.s

The plasmonic lens, see Table 4.2 for design parameters, allows for sub-wavelength near-field imaging. To ensure the best resolution, it is important that the sample be as close to the aperture as possible, see Figure 8.4(b). The plasmonic lens is delicate and to provide some margin of error in the mounting of samples, it was chosen to mount the lens within 250 μm ($\sim 1/4\ \lambda$) of the surface of the samples under investigation, which is within the near-field. Moreover, to ensure the sample is closest to the aperture the beam first passes through the sample before transmitting through the cover slip, as shown in Figure 8.4(b).

After the beam passes through the sample the radiation is collected by a third OAP (f/1)

placed such that its focus is at the plasmonic lens. The subsequent parallel beam is reflected and focused by a fourth OAP (f/1) through a second QWP (not installed) to the horn of the Schottky diode zero biased detector (ZBD).

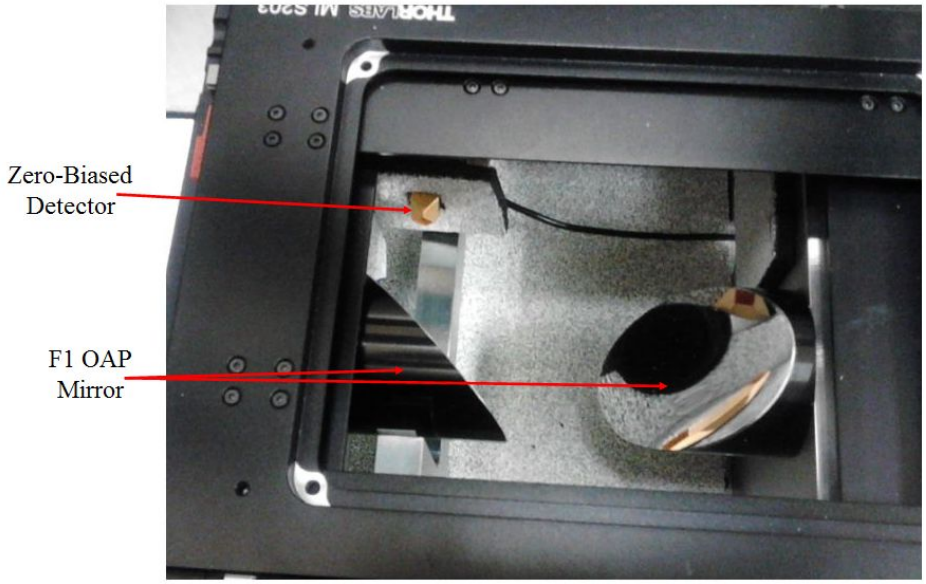

Figure 8.5: Image showing the final two OAP (f/1) mirrors which collect, collimate and focus the beam into the ZBD. The beam will also pass through a second QWP, not shown, to restore the beam to horizontal polarization.

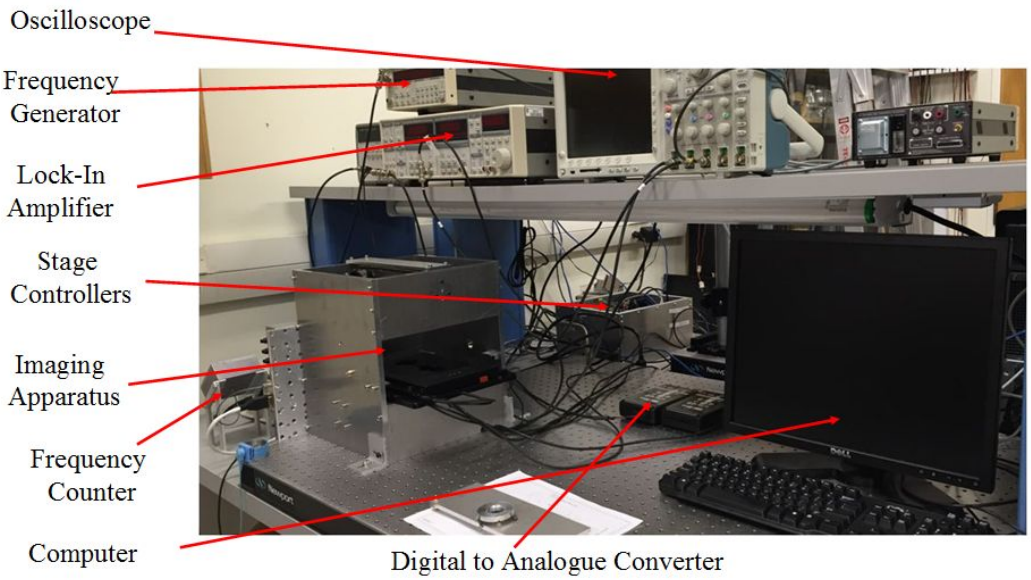

Figure 8.6: Image of the entire THz imaging system.

8.3 THz System Results

Time constraints did not allow for imaging of cancer samples. Spatial resolution was determined by imaging the US Air Force calibration target, see Table 6.3 for specifications [2]. In addition, images were taken of different configurations of water and glass slides and cover slips, to ascertain the sensitivity of the system with respect to measuring the absorption coefficient of water.

8.3.1 Spatial Resolution

Images of the US Air Force calibration target were taken to determine the spatial resolution which the THz imaging system was capable [2]. The calibration target was chosen because it is a clear path, not constructed out of glass, and is designed for far-infra-red optics. The target is electro-formed nickel and is 12 μm thick [2]. Table 6.3 shows the specifications for the slit widths within the target. Figure 8.7 shows an optical image of the calibration target alongside a THz image of the calibration target.

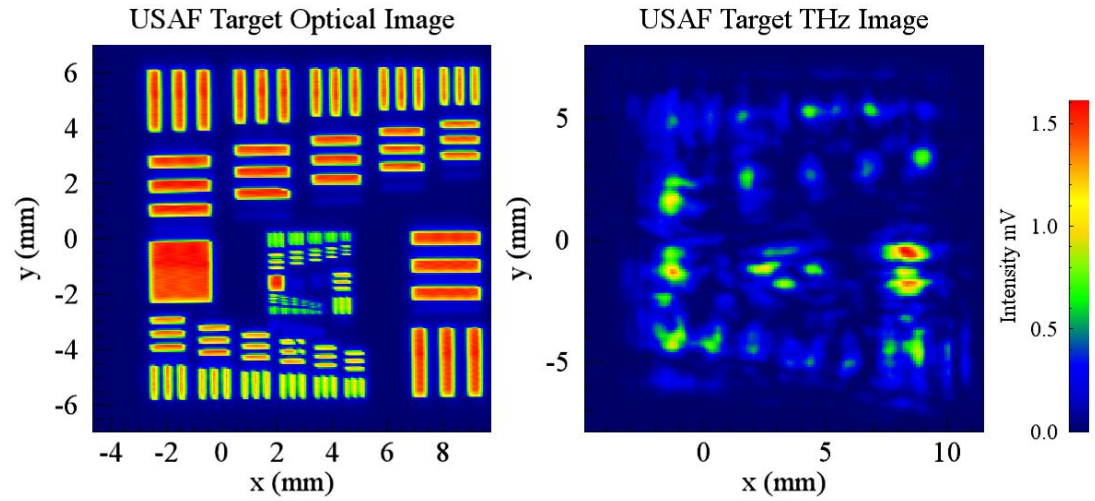

(a)

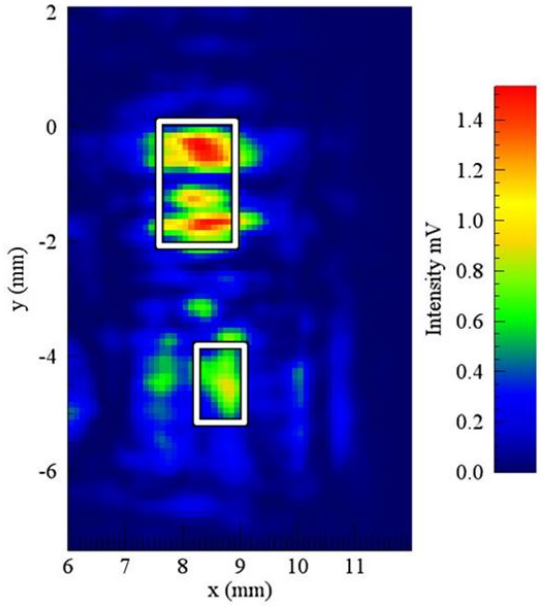

(b)

Figure 8.7: (a) Optical image of the US Air Force calibration target taken with the TSL252 silicon photo-diode detector and THz image of the full field of the same calibration target taken with the THz microscope. (b) THz image of the calibration target analysed to determine the spatial resolution of the system. Black box indicates the region fitted for the FWHM for the horizontal slit and the white box indicate region fitted for the vertical slit.

Spatial resolution was determined by analysing intensity profiles of the image data taken

across the 500 μm wide slits. Analysis involved fitting a Gaussian profile to the intensity curves and determining the full-width at half-maximum (FWHM) of each curve fit. Figure 8.8 shows Gaussian fits for several intensity plots for slits running in either the horizontal (a) or vertical (b) directions and Table 8.1 shows the FWHM values obtained from each of these fits.

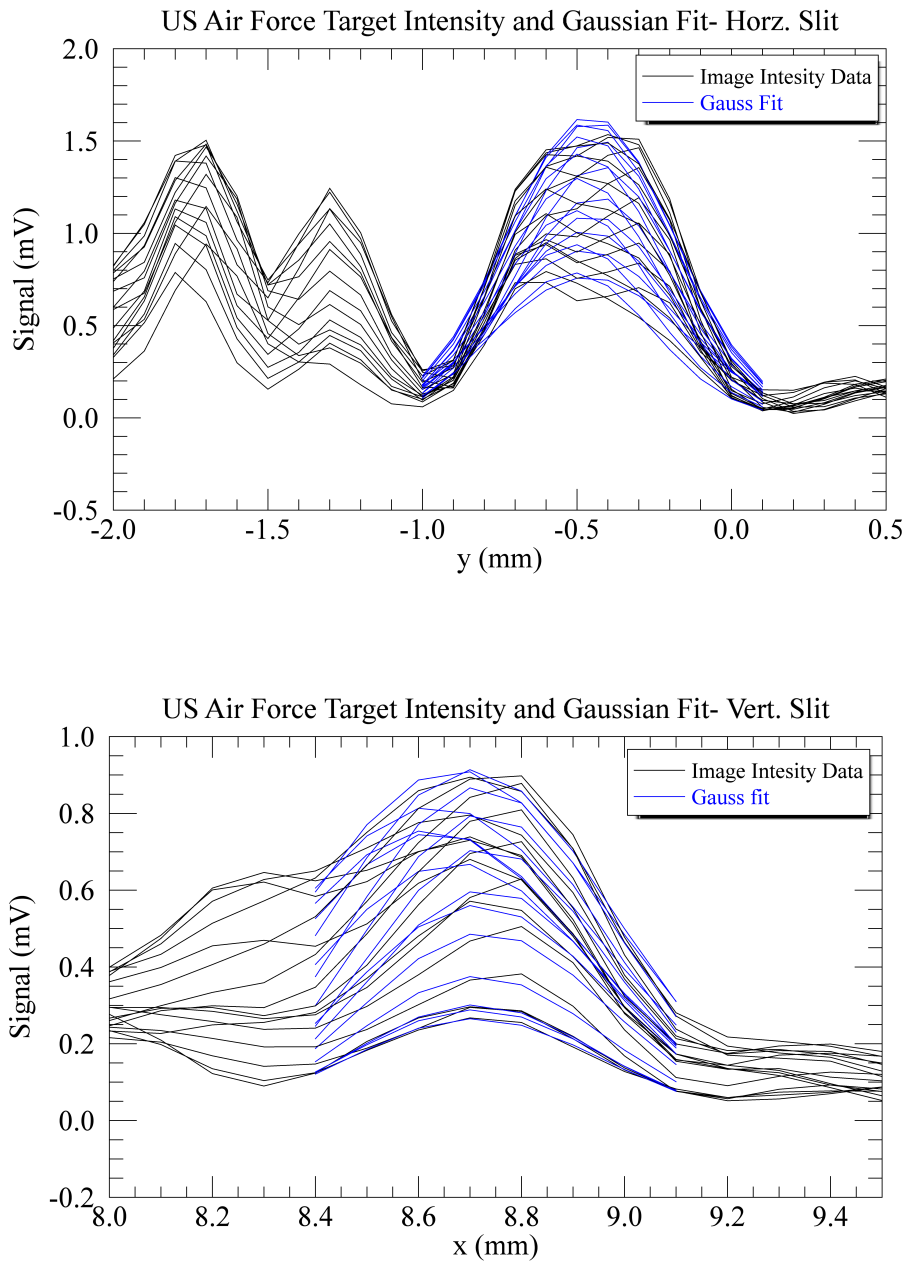

Figure 8.8: Plots of image intensity data and Gaussian fit to find FWHM of horizontal (a) and vertical (b) slit. Finding the FWHM of the slits gives the resolution of the THz imaging system. Regions fitted are indicated in Figure 8.7(b).

Sub-wavelength spatial resolution depends upon the size of the object and the diameter

Horz. Fit 1	Horz. Fit 2	Vert. Fit 1	Vert. Fit 2
590	597	728	774
636	609	693	724
662	635	657	685
690	661	627	648
711	690	611	618
689	704	595	610
634	681	603	616
583	635	621	633
553	588	637	645
539	555	638	657
546	544	628	648
561	549	614	632
561	557	602	630
570	563	607	632
581	586	610	637
552	584	594	622
603 $\pm$ 58	**609 $\pm$ 53**	**629 $\pm$ 37**	**651 $\pm$ 43**

Table 8.1: Table showing the FWHM results for 16 fits of horizontal and vertical slits taken from THz images of the US Air Force calibration target. The bottom row shows the mean and uncertainties for each column. As can be seen, the horizontal slit FWHM is approximately 600 μm, while the vertical slit FWHM is closer to 630 μm. Both are within one standard deviation of the other. Uncertainties are taken as one standard deviation. All measurements are in μm.

	Horz. 1	Horz. 2	Ver. 1	Vert. 2
Fitted FWHM	603 ± 58	609 ± 53	629 ± 37	651 ± 43
Calculated AD	338 ± 98	347 ± 90	382 ± 55	416 ± 62

Table 8.2: Table showing resolution of the THz imaging system. Calculated values for the aperture diameter lie within one or two standard deviations of the actual aperture diameter. All values are reported in μm.

of the aperture used for imaging. The spatial resolution of the as built plasmonic lens, whose central aperture is 300 μm, was determined from analysis of cross scans of the image of the calibration target, shown in Figure 8.8. Neglecting diffraction and interference effects, the apparent slit width (AW) can be approximate, to first order, by the convolution of the actual slit width (SW) with the aperture diameter (AD).

$$AD = \sqrt{AW^2 - SW^2} \tag{8.1}$$

The results shown in Table 8.2 demonstrate that the THz imaging system has achieved sub-wavelength resolution close to the design value. While there appears to be a slight difference in the spatial resolution in the x and y directions this lies within the experimental error and could be the result of diffraction and interference between the metal of the plasmonic lens and the calibration target, since both act as perfect electrical conductors in the THz regime [1]. Furthermore, in these initial tests, the second QWP was not installed which could lead to some asymmetry in the data acquired. Regardless, these results confirm that sub-wavelength resolution is possible with the THz imaging system. The next step to increase spatial resolution is to integrate a plasmonic lens with a 200 μm aperture.

8.3.2 Absorption Coefficient of Water

Measurements of the absorption coefficient were taken by using a combination of glass slides, glass cover-slips and brass shim stock (25 - 100 μm thick) to encase a sample of distilled water. The initial configuration consisted of two glass slides separated by a brass shim at one end to form a wedge. The gap between the slides was filled with distilled water,

whose thickness change is linear with distance from the shim, see Figure 8.9.

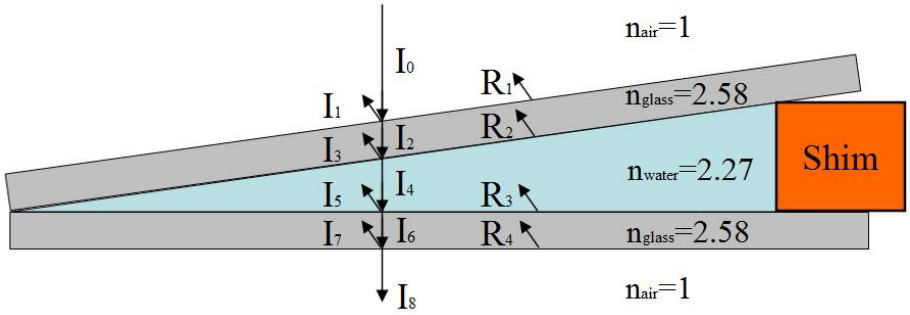

Figure 8.9: Diagram of the intensity of light as it passes through the layers of the water wedge.

Figure 8.10 shows a THz image of such a water wedge configuration. Notice that the transmitted intensity decreases as the thickness of water increases.

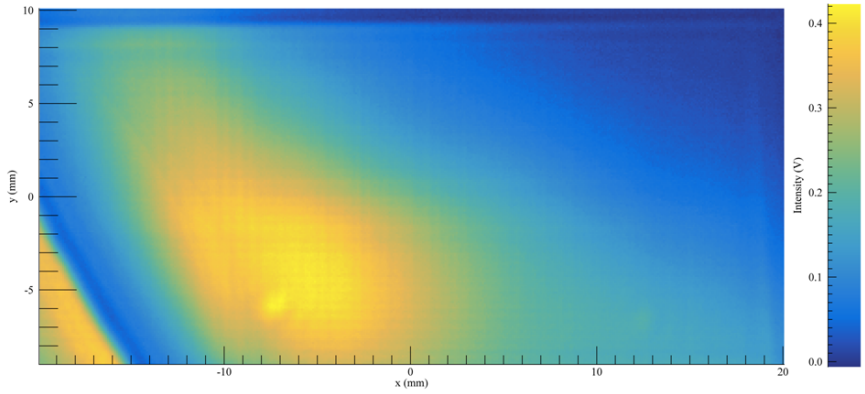

Figure 8.10: Diagram of the intensity of light as it passes through the layers of the water wedge. Note the air bubble in the bottom left corner of the image and the spot at (-7.5,-6).

In order to determine the absorption coefficient of the water contained in the wedge it is important to take into account all sources of loss, such as losses due to reflections at the interfaces and absorption in both glass and water. By analysing Figure 8.9, we can see that transmission intensity will be lost from reflections at each material boundary where the refractive indices differ, shown as R_1-R_4. Since R_1, R_4 and R_2, R_3 are boundaries of

the same materials, we can assume that $R_1 = R_4$ and $R_2 = R_3$. From this, we can find the relationship of the intensities for I_1, I_3, I_5 and I_7 from the Figure.

$$I_1 = I_0(1 - R_1) \tag{8.2}$$

$$I_3 = I_2(1 - R_2) \tag{8.3}$$

$$I_5 = I_4(1 - R_3) = I_4(1 - R_2) \tag{8.4}$$

$$I_7 = I_6(1 - R_4) = I_6(1 - R_1) \tag{8.5}$$

where R is the reflectance, which at normal incidence, is given by

$$R = |\frac{n_1 - n_2}{n_1 + n_2}|^2 \tag{8.6}$$

and n_1 and n_2 are the refractive indices of the materials forming the interface numbered in the order the light moves through them [20]. For the situation illustrated in Figure 8.10 there are three materials to consider: air, glass and water. The refractive indices of these material were taken to be 1 (air), 2.1 (glass [84]) and 2.5 (water [8]).

I_2, I_4 and I_6 each obey the Beer-Lambert law, see Equation 7.1, so they can be written as follows:

$$I_2 = I_1 e^{-\alpha_g x_{g1}} \tag{8.7}$$

$$I_4 = I_3 e^{-\alpha_w x_w} \tag{8.8}$$

$$I_6 = I_5 e^{-\alpha_g x_{g2}} \tag{8.9}$$

where α_g is the absorption coefficient of glass, x_{g1} and x_{g2} are the thickness of the glass slide or glass cover-slip and x_w is the thickness of the water which depends on position. If two glass slides are used then $x_{g1} = x_{g2} = x_g$. The absorption coefficient of the glass slides was taken to be 0.9 mm^{-1} [53]. For this situation, if I_7 is the intensity of the beam after the

final reflection, then $I_7 = I_8$.

From this analysis the dependence of I_8 on the initial intensity of the beam, I_0 can be extracted.

$$I_8 = I_0(1-R_1)^2(1-R_2)^2 e^{-2\alpha_g x_g} e^{-\alpha_w x_w} \tag{8.10}$$

By rearranging and taking the natural logarithm one arrives at

$$\alpha_w x_w = -ln\left(\frac{I_0}{(1-R_1)^2(1-R_2)^2 e^{-2\alpha_g x_g}}\right) \tag{8.11}$$

By plotting $\alpha_w x_w$ against the thickness of the water in the wedge (x_w) the absorption coefficient of water can be found as the slope of the line of the data, shown in Figure 8.11.

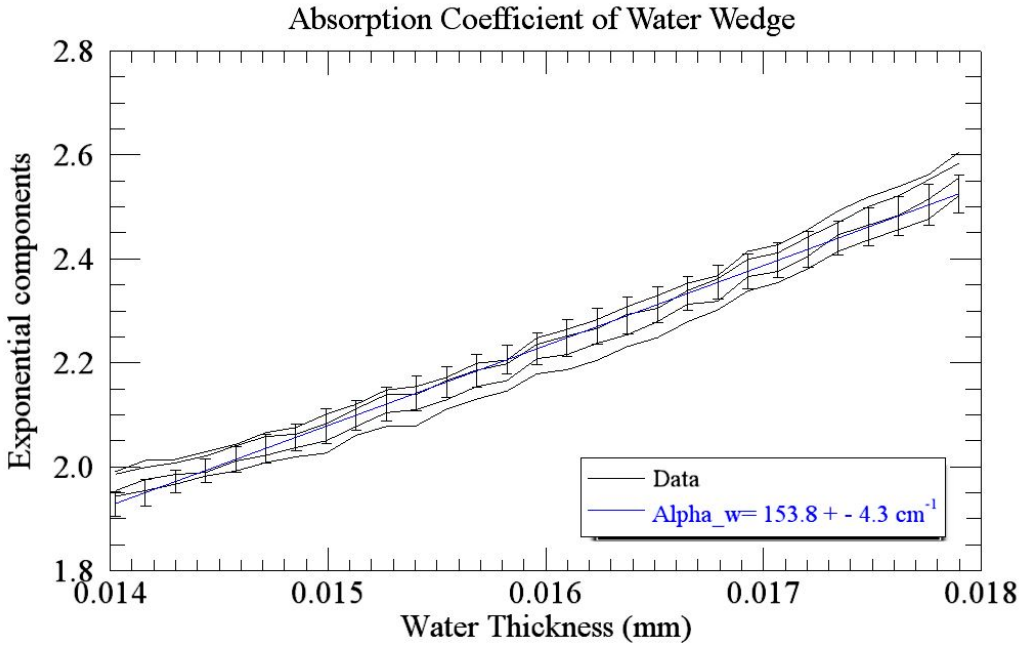

Figure 8.11: Figure of the exponential components of the Beer-Lambert law plotted against the thickness of water within the wedge. The absorption coefficient of water is found by finding the slope of the line.

From this analysis, it was found that the absorption coefficient of the water within the water wedge apparatus was 153 ± 3 mm^{-1}. While this number is different from the values

reported in the literature,123 - 135 mm^{-1} [8, 85], it is calculated on the assumption that the absorption coefficient and refractive indices of the glass are well know. Also, although distilled water was used, residual impurities remaining in the water could have an effect its absorption coefficient. Nonetheless, these first results show that the apparatus is capable of measuring the absorption coefficient of a liquid in a controlled setting.

Figure 8.12, taken from [8], present results of the absorption coefficient and refractive index of water taken over a range of instrumentation. The blue dots on the upper plot, Figure 8.12, are measurements taken with a free electron laser, a device which costs over a billion dollars [9]. The absorption coefficient was able to be measured with the simple system, described in Figure 8.9, and our, relatively, inexpensive apparatus. Considering the simplicity of our measuring, the initial result for the absorption coefficient of liquid water is very promising. Further investigation into the optical properties of the glass slides used will allow for determination of this value with greater accuracy.

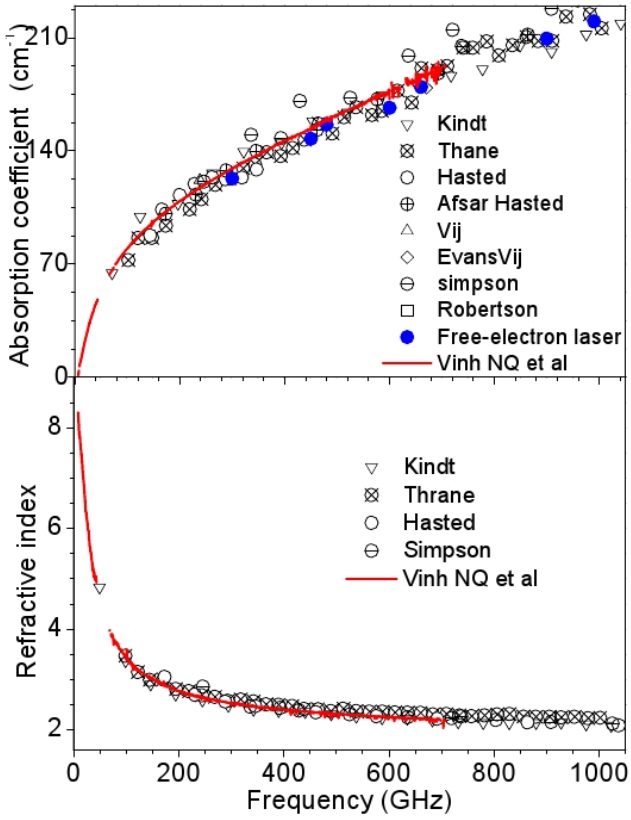

Figure 8.12: Plot showing measurements of the absorption coefficient and refractive index of water in the THz range [8, 9].

Analysis of Transmitted Intensity Through Glass

Although the absorption coefficient of water was determined by the analysis of the water-wedge system, understanding of the sensitivity of the system is difficult to obtain from that approach. In order to ascertain the sensitivity of the system the signal to noise ratio was determined for transmitted THz radiation through glass. Images were obtained, see Figure 8.13, through both a glass cover-slip and a glass microscope slide. From the Beer-Lambert law, Equation 7.1, it is understood that the intensity of transmitted radiation through a material depends upon both the absorption coefficient and the thickness of the material.

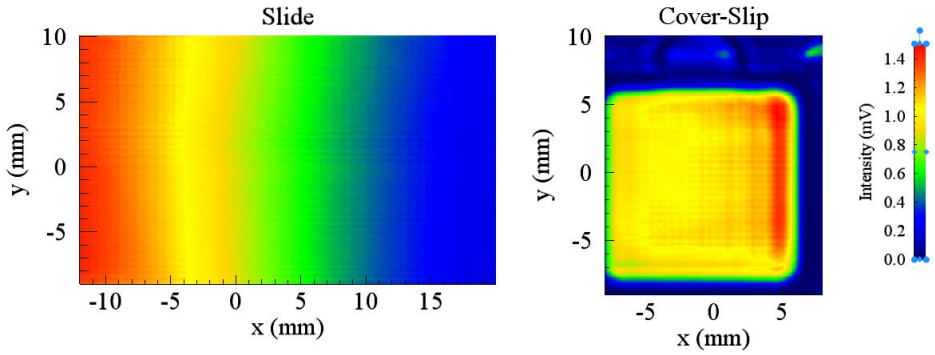

Figure 8.13: Images of THz image of bare cover-slip (right) and microscope slide (left). As can be seen from the change in transmitted intensity through the slide, the cover-slip has a much smaller change in thickness than does the slide.

The change in intensity seen as the microscope slide is scanned along its long axis is believed to be due to the thickness variation of the slide; the slide is likely slightly wedge shaped. To investigate this further, a precision cover-slip (Zeiss Thickness No.: 1.5 High performance 18 mm x 18 mm) was measured, whose thickness is 0.170 +/- 0.005 mm (or the variance is $\lambda/200$). The thinner cover slip results in greater transmission and more precise geometry should result in a more uniform image as can be seen in the right image of Figure 8.13. This image has been analysed to determine its uniformity, expressed in its signal to noise.

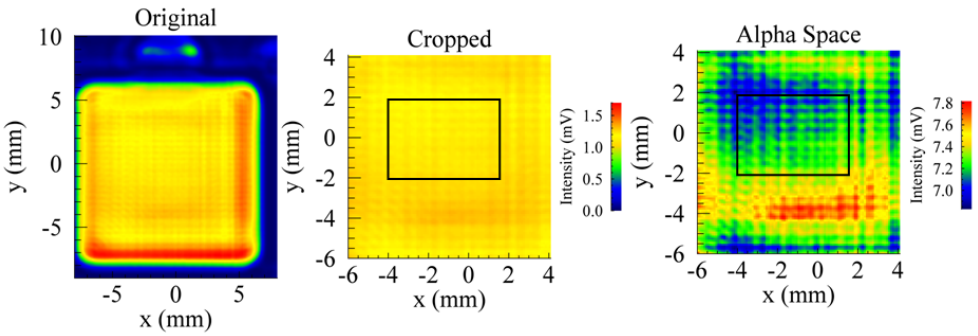

Figure 8.14: 'Original' is the raw image taken by the THz imaging system. 'Cropped' shows the region selected for study. A plane, fitted to the intensity gradient seen in the image, was subtracted to arrive at the variance and the image brought into absorption coefficient space, shown in 'Alpha Space'. The region used to determine the S/N is indicated by the black box.

Determination of the S/N was accomplished by finding the average and standard deviation of the transmitted intensity in a sub-region of the cover-slip image, which was determined to have the least variance in the thickness of the glass, and dividing them.

$$\frac{S}{N} = \frac{AverageIntensity}{StandardDeviation} \tag{8.12}$$

The signal to noise in this simple preliminary measurement, in which the configuration was not optimized, was determined to be 122. From Figure 3.3, the necessary S/N required to differentiate cancerous tissue from healthy tissue can be determined. There is a 4% change in the intensity of light which passes through 20 μm sample of cancerous tissue when compared to normal breast tissue of the same thickness, see Figure 3.3. Since this corresponds to a required S/N of 25, this measurement shows that we have met the minimum sensitivity required for tissue differentiation. Calculations based upon detector noise-equivalent-power (NEP) indicate that there is the potential for significant improvements in S/N.

8.3.3 Rat Brain

A paraffin embedded rat brain sample was made in the Dunn Lab at the University of Calgary and sectioned, 20 μm thick, and mounted on a cover-slip by myself. The rat brain was placed into the THz imaging system and scanned with the imaging data stored in an IDL '.sav' file The image was processed using the software described in Chapter 7, where a 5x5 spatial averaging filter was employed for smoothing and the Sobel derivative function was used for edge detection. The top left-hand image of Figure 8.15 shows the original THz image. Contrary to the expected reduction in imaging intensity after passing through the rat brain sample, when compared to the cover-slip alone, the regions of the image where the radiation passed through paraffin show increased intensity, which will be explained below.

Figure 8.15 shows six images which include the raw image ('Original'), cropped area of interest ('Cropped') and the cropped image after a smoothing filter reduced extraneous noise ('Smoothed'). Next, the smoothed image after the natural logarithm transferred the image into absorption coefficient space ('Natural Log'), the image after a Sobel derivative filter enhanced the edges ('Derivative') and an optical image taken with a DSLR camera of the rat brain slide cropped to approximately the same area ('Optical Image').

From a comparison of the 'Natural Log' and 'Derivative' THz images of the rat brain with the 'Optical Image', from Figure 8.15, it can be seen that the outer boundary seen in the THz images conforms with the outer boundary of the rat brain section. Although the 'Derivative' image has suggestions of features within the rat brain sample, a visual comparison with the 'Optical Image' does not confirm this. The region within both the 'Natural Log' and 'Derivative' images from Figure 8.15 show peak intensity in the area of (-5,-1.5) which may result from lensing effects due to increased paraffin thickness in that region of the rat brain slide.

As can be seen in Figure 8.15, the signal is highest at the location of the sample (and pieces paraffin wax). The observed increase in transmission can be easily explained by the paraffin embedded tissue acting as an anti-reflection coating on the higher refractive

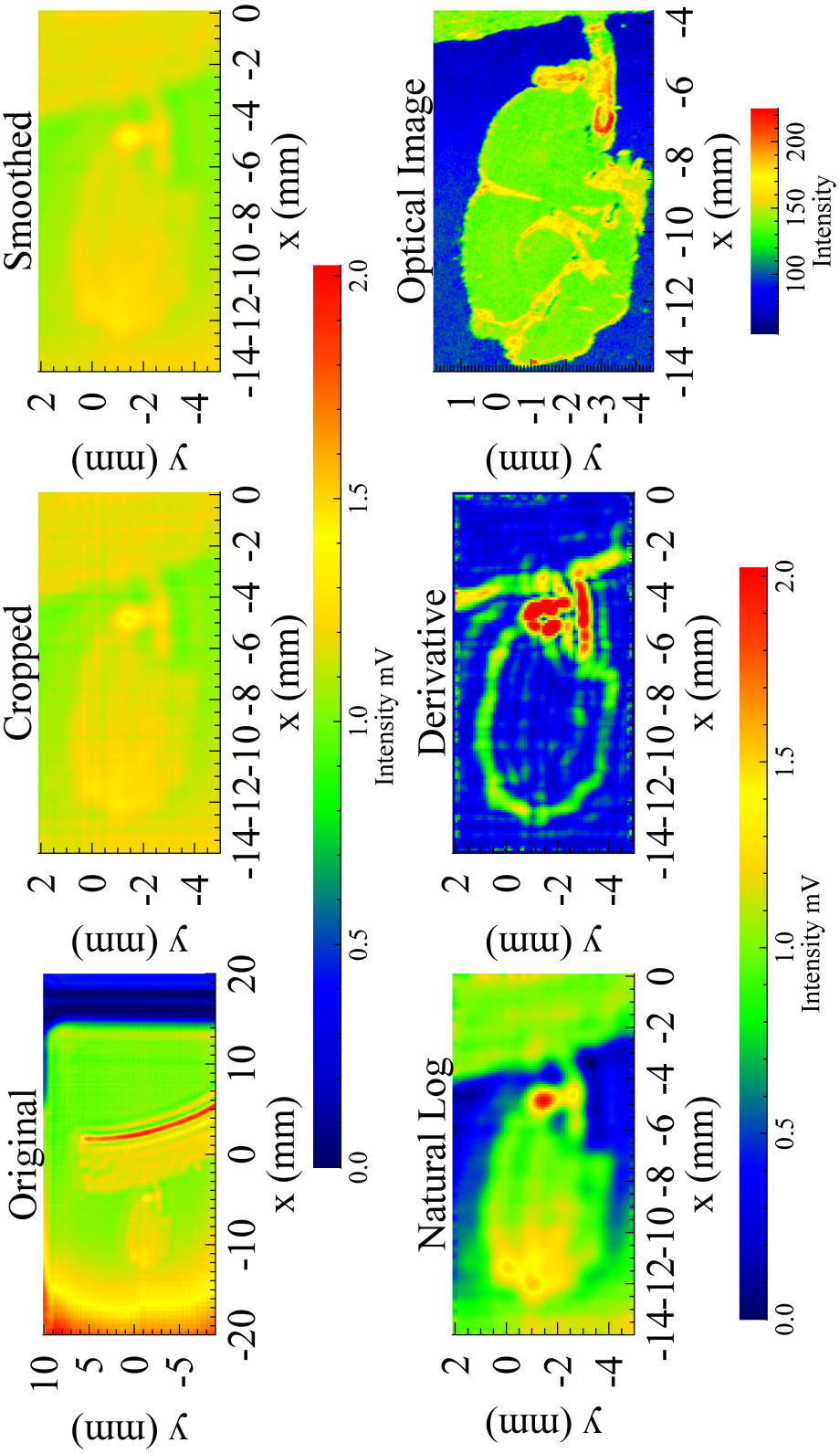

Figure 8.15: Images of 20 μm paraffin embedded rat brain sample, see the text for details.

index glass, thereby allowing a greater fraction of the incident light to penetrate in these areas than the uncoated glass. Further evidence for this is seen in the 'Original' image, in Figure 8.15, where the sweeping arc of high intensity transmission corresponds to a thicker piece of paraffin. To study the effects on this brain tissue would require a knowledge of the reflection coefficient of the paraffin embedded slide. While time precluded accomplishing this, the above plots do show that we have the sensitivity to measure the presence of tissue, the spatial resolution and the software to detect edges and identify features in a sample, as expected.

Resolution with Paraffin Ridge

Since the image of the rat brain contained a very narrow feature, THz scans of this ridge were used for further verification of the spatial resolution. Figure 8.16 shows the raw image of the rat brain slide taken with the THz microscope (left) and optical DSLR camera (right).

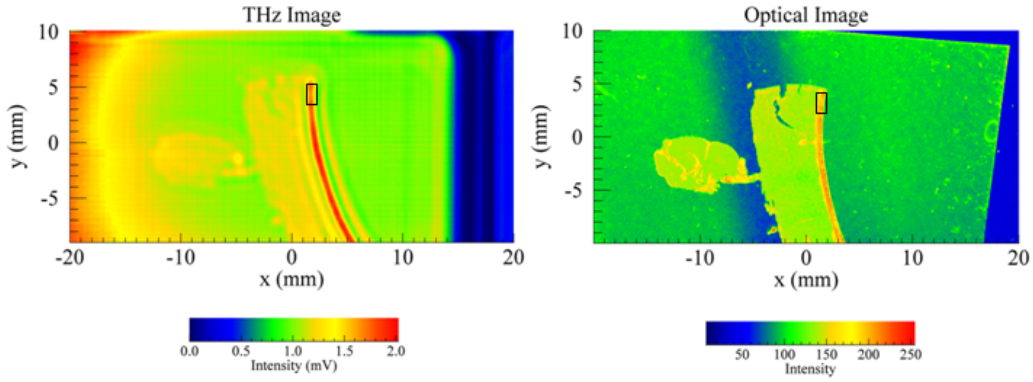

Figure 8.16: Raw images of the rat brain slide in both the THz (left) and optical (right). Regions used for Gaussian fit are indicated with a black box.

The FWHM were found for the regions indicated in Figure 8.16 using the same procedure that was used on the image of the calibration target. Figure 8.17 shows the raw intensity data (black) and the Gaussian fits (blue).

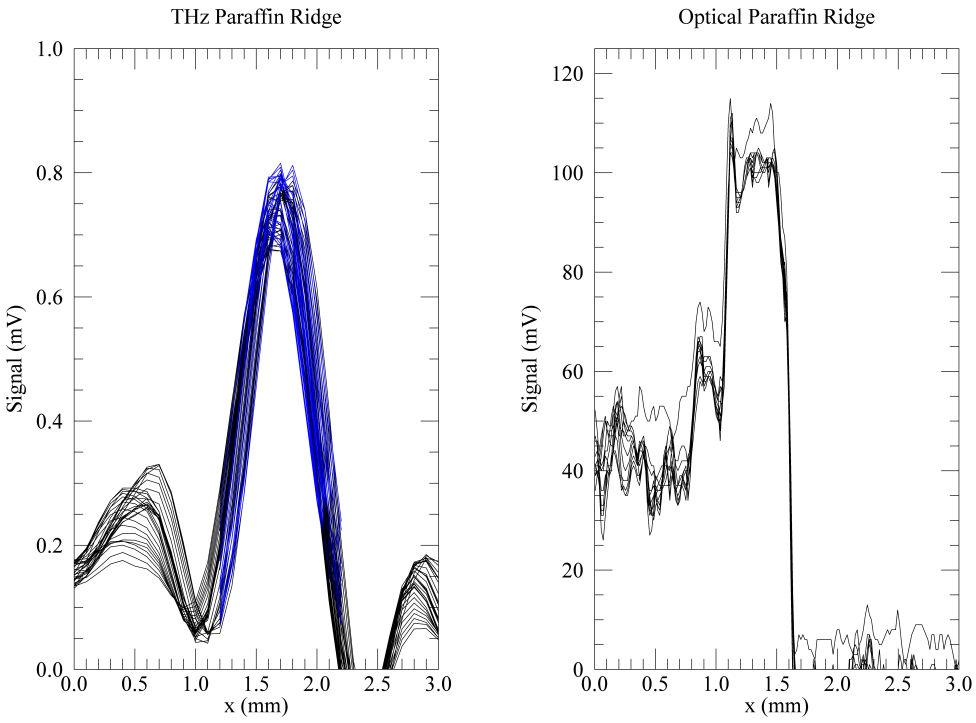

Figure 8.17: Plots of image intensity (black) from the THz (left) and optical (right) images from the regions indicated in Figure 8.16 plotted with the Gaussian fits (blue).

From the fits shown in Figure 8.17 the average FWHM for the THz image of the paraffin ridge was found to be 638 $\pm$ 28 μm. By using the Sobel derivative function, the thickness of the paraffin ridge was determined by determining the separation between the maxima which correspond to the rise and fall of the ridge. The thickness was found in this was to be 497 $\pm$ 41 μm. Using the diameter of the aperture, 300 μm, the measurement of the ridge thickness to determine the theoretical thickness of the ridge in the THz image to compare with the value found from the image. Calculation of the diameter of the aperture with this value gives 697 $\pm$ 50 μm. Again showing that in a real microscope slide the designed spatial resolution was retained when looking through the paraffin and cover-slip.

Chapter 9

Conclusions

Breast cancer is one of the highest diagnosing cancers in Canada and world-wide [10]. The incidence of morbidity due to breast cancer has decreased in Canada over the past 30 year as early detection has been encouraged [3]. Currently breast cancer is diagnosed by use of optical microscopy on tissue samples obtained via biopsy of surgical means. These diagnoses require considerable time, for sample preparation, and a pathologist with great skill, to prevent misdiagnosis [12, 32]. Significant improvement could be achieved by the development of an imaging technique which exploits the properties of the cancerous tissue to differentiate from healthy tissue. TeraHertz imaging (Chapter 3), around 0.325 THz, has been shown to be sensitive to the presence of cancerous breast tissue due to a difference in its absorption coefficient as compared to the absorption coefficient of healthy breast tissue [49]. This thesis set out to show the development and use of a THz imaging system designed for breast cancer detection and margin determination in slide mounted tissue samples.

Although THz imaging has been shown to be sensitive to cancer, achieving sufficient spatial resolution for tissue differentiation and margin determination has been notoriously difficult due to the long wavelength of the light ($\sim$ 1 mm) [20]. A Bullseye structure plasmonic lens (Chapter 4), designed to function at approximately 0.325 THz increase the trasmitted power through a sub-wavelength aperture, was fabricated and integrated into the THz imaging system. The knife-edge test (Chapter 5) is an optical test which was developed to verify the performance of the plasmonic lens prior to its use in the THz imaging

system. Design and testing of the plasmonic lens were the subject matter of Mr. Tanner Heggie's thesis [1]. Prior to integrating all components into the final THz system, an optical analogue imaging system (Chapter 6) was designed and constructed to provide the opportunity for resolution testing of the two-axis translation stage, trouble shooting and software development (Chapter 7).

An optical test, known as the knife-edge test, was adapted for use to determine the beam profile and divergence of the THz beam, both incident on and resulting from the plasmonic lens. The technique was verified by beam profile measurements of a single-mode Helium-Neon laser.

The work of Chiu *et al.*, was used as the starting point for the design of the THz imaging system [16, 26, 46, 50, 52]. It was surmised that an imaging system could be designed to acquire images of an area of 10 mm x 10 mm with 100 μm step size in less time than was required by the Chiu apparatus (minimum 60 sec). It was ascertained that with the combination of the Thorlabs MLS203 X-Y translation stage integrated with the Aerotech Solist motion controllers capable of the PSO option that an image of this area and resolution could be acquired in 19.6 sec. This is an improvement of three times the best imaging time that the Chiu *et al.*, group was able to accomplish (2015) and is an improvement of two orders of magnitude over their original image acquisition time (2009).

The THz microscope was used to determine the specificity and the spatial resolution which the system was capable. THz images acquired with the microscope of a water wedge test system and US Air Force calibration target were used for specificity and spatial resolution determination [2]. Analysis of the water wedge system resulted in a measurement of the absorption coefficient of water of 153 ± 3.27 cm^{-1}. This result is reasonable for an initial result and will require further testing to improve the measurement. Spatial resolution was determined by fitting a Gaussian profile to the regions of the THz image of the calibration target which corresponded to the 500 μm slit, both vertical and horizontal, finding the full-width at half-maximum and determining the radius of the aperture which would be

required to achieve this resolution. The plasmonic lens had an aperture of 300 μm and it was found though this analysis that the calculated aperture diameter was 337 $\pm$ in the x direction and 382 $\pm$ μm in the y direction. This difference may be due to diffraction effects or interaction with the plasmonic lens and the lack of the second quarter-wave plate from the apparatus for the initial tests. Regardless, these results confirm that the microscope has achieved sub-wavelength imaging at THz frequencies.

Final testing of the apparatus was accomplished by imaging a sample or rat brain mounted on a glass cover slip. The sample was paraffin embedded and was 20 μm thick. Unexpectedly, the THz image of the regions of the glass cover slip where the sample of rat brain or paraffin film had adhered had a higher intensity than those regions which the THz light was incident on bare glass.

Having validated the performance of the THz microscope the next steps are to produce a plasmonic lens with a 200 μm aperture and image a series of breast cancer samples currently being prepared by Dr. Doug Demetrick at the University of Calgary to investigate and compare properties of paraffin embedded, deparaffinized and frozen tissue sections.

Bibliography

[1] T. J. Heggie, "Subwavelength imaging using plasmonic lenses at terehartz frequencies," Master's thesis, University of Lethbridge, 2014.

[2] www.edmundoptics.com, *Clear Optical Path USAF Target*.

[3] www.cancer.ca, "Canadian cancer statistics: 2013," May 2013.

[4] www.cancer.gov, "Getting Your Mammogram Results." Internet, Mar 2014.

[5] "Ultrasound images," Apr 2015.

[6] P. C. Ashworth, E. Pickwell-MacPherson, S. E. Pinder, E. Provenzano, A. D. Purushotham, M. Pepper, and V. P. Wallace, "Terahertz spectroscopy of breast tumors," in *Proceedings of IEEE Conference on Infrared and Millimeter Waves and Terahertz Electronics*, pp. 603–605, Sept. 2007.

[7] J. Weiner, "The physics of light transmission through subwavelength apertures and aperture arrays," *Reports on Progress in Physics*, vol. 72, p. 064401, May 2009.

[8] N. Vinh, J. Allen, and K. Plaxco, "Probing the dynamics of biomolecules in liquid water by terahertz spectroscopy," *Bulletin of the American Physical Society*, vol. 56, 2011.

[9] M. E. e. a. Altarelli, "The european x-ray free-electron laser: Technical design report," tech. rep., DESY XFEL Project Group, 2006. ISBN 978-3-935702-17-1.

[10] A. Jemal, F. Bray, M. M. Center, J. Ferlay, E. Ward, and D. Forman, "Global cancer statistics," *CA: A Cancer Journal for Clinicians*, vol. 61, pp. 69–90, Mar 2011.

[11] J. E. Joy, E. E. Penhoet, and D. B. Petitti, eds., *Saving Women's Lives: Strategies for Improving Breast Cancer Detection and Diagnosis*. The National Academies Press, 2005.

[12] N. E. Davidson and D. L. Rimm, "Expertise vs evidence in assessment of breast biopsies: an atypical science," *The Journal of the American Medical Association*, vol. 313, p. 1109, Mar 2015.

[13] E. Pickwell and V. P. Wallace, "Biomedical applications of terahertz technology," *Journal of Physics D: Applied Physics*, vol. 39, pp. R301–R310, Sep 2006.

[14] D. Mittelman, ed., *Sensing with Terahertz Radiation*. Springer, 2003.

[15] E. Pickwell-MacPherson, A. J. Fitzgerald, and V. P. Wallace, *SPIE Proceedings*, pp. 82210M–82210M–6. SPIE - International Society for Optical Engineering, Feb 2012.

[16] C.-M. Chiu, H.-W. Chen, Y.-R. Huang, Y.-J. Hwang, W.-J. Lee, H.-Y. Huang, and C.-K. Sun, "All-terahertz fiber-scanning near-field microscopy," *Optics Letters*, vol. 34, p. 1084, Mar 2009.

[17] R. M. Woodward, B. E. Cole, V. P. Wallace, R. J. Pye, D. D. Arnone, E. H. Linfield, and M. Pepper, "Terahertz pulse imaging in reflection geometry of human skin cancer and skin tissue," *Physics in Medicine and Biology*, vol. 47, pp. 3853–3863, Nov 2002.

[18] S. Sy, S. Huang, Y.-X. J. Wang, J. Yu, A. T. Ahuja, Y.-T. Zhang, and E. Pickwell-MacPherson, "Terahertz spectroscopy of liver cirrhosis: investigating the origin of contrast," *Physics in Medicine and Biology*, vol. 55, pp. 7587–7596, Dec 2010.

[19] P. Doradla, K. Alavi, C. Joseph, and R. Giles, "Detection of colon cancer by continuous-wave terahertz polarization imaging technique," *Journal of Biomedical Optics*, vol. 18, p. 090504, Sep 2013.

[20] E. Hecht, *Optics*. Addison-Wesley, 3 ed., 2002.

[21] S. Freeman, J. C. Sharp, and M. Harrington, *Biological Science*. Toronto: Pearson Benjamin Cummings, 2011.

[22] S. Hunsche, M. Koch, I. Brener, and M. Nuss, "THz near-field imaging," *Optics Communications*, vol. 150, pp. 22–26, May 1998.

[23] H. Bethe, "Theory of diffraction by small holes," *The Physical Review*, vol. 66, pp. 163–182, Oct 1944.

[24] T. W. Ebbesen, H. J. Lezec, H. F. Ghaemi, T. Thio, and P. A. Wolff, "Extraordinary optical transmission through sub-wavelength hole arrays," *Nature*, vol. 391, pp. 667–669, Feb 1998.

[25] T. Thio, K. M. Pellerin, R. A. Linke, H. J. Lezec, and T. W. Ebbesen, "Enhanced light transmission through a single subwavelength aperture," *Optics Letters*, vol. 26, no. 24, p. 1972, 2001.

[26] H. Chen, S.-H. Ma, W.-X. Yan, X.-M. Wu, and X.-Z. Wang, "The diagnosis of human liver cancer by using THz fiber-scanning near-field imaging," *Chinese Physics Letters*, vol. 30, p. 030702, Mar 2013.

[27] www.phac aspc.gc.ca, "Cancer." Internet, May 2014.

[28] www.mayoclinic.org, "Breast cancer: Tests and diagnosis," Apr 2015.

[29] www.cancer.ca, "Screening for Breast Cancer." Internet, 2015.

[30] R. G. Amedee and N. R. Dhurandhar, "Fine-needle aspiration biopsy," *The Laryngoscope*, vol. 111, no. 9, pp. 1551–1557, 2001.

[31] I. Bleiweiss, S. Jaffer, and S. Drossman, *Breast Core Biopsy: A Pathologic-radiologic Correlative Approach*. Saunders Elsevier, 2008.

[32] D. Taatjes and B. Mossman, *Cell Imaging Techniques: Methods and Protocols*. Methods in molecular biology, Humana Press, 2006.

[33] www.cancer.net, "Biopsy." Internet, Mar 2014.

[34] A. Hayat, *Handbook of Immunohistochemistry and in situ Hybridization of Human Carcinomas: Molecular Genetics, Gastrointestinal Carcinoma, and Ovarian Carcinoma*. Handbook of Immunohistochemistry and in Situ Hybridization of Human Carcinomas, Elsevier Science, 2006.

[35] J. Jennette, *Immunohistology in Diagnostic Pathology*. Taylor & Francis, 1988.

[36] D. Murphy and M. Davidson, *Fundamentals of Light Microscopy and Electronic Imaging*. Wiley, 2012.

[37] www.protocolsonline.com, "Haematoxylin Eosin (H&E) staining." Internet, Jul 2012.

[38] www.cancer.gov, "Breast cancer screening: Harms of screening mammography," Apr 2015.

[39] A. Malich, D. Sauner, C. Marx, M. Facius, T. Boehm, S. O. Pfleiderer, M. Fleck, and W. A. Kaiser, "Influence of breast lesion size and histologic findings on tumor detection rate of a computer-aided detection system," *Radiology*, vol. 228, pp. 851–856, Sep 2003.

[40] www.cancer.gov, "Risks of Breast Cancer Screening." Website, May 2013. accessed July 5 2013.

[41] E. Ru and P. Etchegoin, *Principles of Surface-Enhanced Raman Spectroscopy: and related plasmonic effects*. Elsevier Science, 2008.

[42] J.-H. Chen, H. E. Avram, L. E. Crooks, M. Arakawa, L. Kaufman, and A. C. Brito, "In vivo relatation time and hydrogen density at 0.063-4.85 t in rats with implanted mammary adenocarcinomas," *Radiology*, vol. 184, pp. 427–434, 1992.

[43] A. J. Fitzgerald, V. P. Wallace, M. Jimenez-Linan, L. Bobrow, R. J. Pye, A. D. Purushotham, and D. D. Arnone, "Terahertz pulsed imaging of human breast tumors," *Radiology*, vol. 239, pp. 533–540, May 2006.

[44] T. Globus, A. Bykhovski, T. Khromova, B. Gelmont, L. K. Tamm, and L. C. Salay, "Low-terahertz spectroscopy of liquid water," *Proc. SPIE*, vol. 6772, pp. 67720S–67720S–11, 2007.

[45] F. Wahaia, G. Valusis, L. M. Bernardo, A. Almeida, J. A. Moreira, P. C. Lopes, J. Macutkevic, I. Kasalynas, D. Seliuta, R. Adomavicius, and et al., "Detection of colon cancer by terahertz techniques," *Journal of Molecular Structure*, vol. 1006, pp. 77–82, Dec 2011.

[46] H. Chen, W.-J. Lee, H.-Y. Huang, C.-M. Chiu, Y.-F. Tsai, T.-F. Tseng, J.-T. Lu, W.-L. Lai, and C.-K. Sun, "Performance of THz fiber-scanning near-field microscopy to diagnose breast tumors," *Optics Express*, vol. 19, p. 19523, Sep 2011.

[47] M. Hoffmann, *Novel Techniques in THz-Time-Domain-Spectroscopy: A comprehensive study of technical improvements to THz-TDS*. PhD thesis, Albert-Ludwigs-Universitat Freiburg im Breisgau, May 2006.

[48] K.-E. Peiponen, J. A. Zeitler, and M. Kuwata-Gonokami, *Terahertz Spectroscopy and Imaging*. Springer, 2013.

[49] P. C. Ashworth, E. Pickwell-MacPherson, E. Provenzano, S. E. Pinder, A. D. Purushotham, M. Pepper, and V. P. Wallace, "Terahertz pulsed spectroscopy of freshly excised human breast cancer," *Optics Express*, vol. 17, p. 12444, Jul 2009.

[50] H. Chen, T.-H. Chen, T.-F. Tseng, J.-T. Lu, C.-C. Kuo, S.-C. Fu, W.-J. Lee, Y.-F. Tsai, Y.-Y. Huang, and E. Y. Chuang, "High-sensitivity in vivo THz transmission imaging of early human breast cancer in a subcutaneous xenograft mouse model," *Optics Express*, vol. 19, p. 21552, Oct 2011.

[51] H. Chen, X. Wang, T. Zhao, and J. Yang, "Diagnose human tumors by THz near-field imaging," *Twelfth International Conference on Photonics and Imaging in Biology and Medicine (PIBM 2014)*, Sep 2014.

[52] H. Chen, S. Ma, X. Wu, W. Yang, and T. Zhao, "Diagnose human colonic tissues by terahertz near-field imaging," *Journal of Biomedical Optics*, vol. 20, p. 036017, Mar 2015.

[53] S. Gunuganti, "Absorption coefficient of various microscopic slides," tech. rep., Blue Sky Spectroscopy Inc., Aug 2011.

[54] R. Piesiewicz, C. Jansen, S. Wietzke, D. Mittleman, M. Koch, and T. Kurner, "Properties of building and plastic materials in the THz range," *International Journal of Infrared and Millimeter Waves*, vol. 28, pp. 363–371, Mar 2007.

[55] D. Sarid and W. Challener, *Modern Introduction to Surface Plasmons: Theory, Mathematica Modeling, and Applications*. Modern Introduction to Surface Plasmons: Theory, Mathematica Modeling, and Applications, Cambridge University Press, 2010.

[56] W. L. Barnes, A. Dereux, and T. W. Ebbesen, "Surface plasmon subwavelength optics," *Nature*, vol. 424, pp. 824–830, Aug 2003.

[57] S. Maier, *Plasmonics: Fundamentals and Applications: Fundamentals and Applications*. Springer, 2007.

[58] A. K. Azad, *Resonant terahertz transmission of plasmon subwavelength hole arrays*. PhD thesis, Oklahoma State University, May 2006.

[59] D. Griffiths, *Introduction to Electrodynamics*. Prentice Hall, 1999.

[60] O. Mahboub, S. C. Palacios, C. Genet, F. J. Garcia-Vidal, S. G. Rodrigo, L. Martin-Moreno, and T. W. Ebbesen, "Optimization of bulls eye structures for transmission enhancement," *Optics Express*, vol. 18, pp. 11292–11299, May 2010.

[61] www.cmc.ca, "CMC Microsystems," Apr 2015.

[62] D. Malacara, ed., *Optical Shop Testing*. John Wiley & Sons, Inc., 2 ed., 1992.

[63] E. P. Goodwin and J. C. Wyant, *Field Guide to Interferometric Optical Testing*. SPIE, Sep 2006.

[64] D. R. Smith, *Modern Optical Engineering: The Design of Optical Systems*. McGraw-Hill, 2000.

[65] D. A. Naylor, B. G. Gom, and B. Zhang, "Preliminary design of fts-2: an imaging fourier transform spectrometer for scuba-2," *International Society for Optics and Photonics*, pp. 62751Z–62751Z, 2006.

[66] W. S. Holland, E. I. Robson, W. K. Gear, C. R. Cunningham, J. F. Lightfoot, T. Jenness, R. J. Ivison, J. A. Stevens, P. A. R. Ade, M. J. Griffin, and et al., "SCuba: a common-user submillimetre camera operating on the james clerk Maxwell telescope," *Monthly Notices of the Royal Astronomical Society*, vol. 303, p. 659???672, Mar 1999.

[67] www.spectra physics.com, *Stabilized Helium-Neon Laser - Model 117A*. Spectra-Physics Inc., 1335 Terra Bella Avenue Mountain View, CA 94043, 2004.

[68] B. E. A. Saleh and M. C. Teich, *Fundamentals of Photonics*. Wiley-Interscience, 2 ed., 2007.

[69] S. Cornish, "Gaussian beams and the knife-edge measurement," 2012.

[70] www.thorlabs.com, *Si Photodiode: 350-1100 nm*. Thorlabs, Apr 2013.

[71] www.newport.com, *Piezo Motor Driven Components*. Newport, Corp., Irvine, CA, 2009.

[72] K. Riley, P. Hobson, and S. Bence, *Mathematical Methods for Physics and Engineering: A Comprehensive Guide*. Cambridge University Press, 2006.

[73] www.vadiodes.com, "Virginia diodes, inc.." Electronic, Mar 2015.

[74] www.exelisvis.com, "Interactive Display Language," Apr 2015.

[75] www.thorlabs.com, "Thorlabs, inc.."

[76] www.aerotech.com, "Aerotech, inc.."

[77] www.aerotech.com, *Soloist CP Hardware Manual*. Aerotech, 2012.

[78] www.ti.com, *TSL250, TSL251, TSL252: Light to Voltage Optical Sensors*. Texas Instruments, Nov 1995.

[79] www.datatranslation.com, "DataTranslation Inc.," Apr 2015.

[80] H. Young, R. Freedman, and A. Ford, *Sears and Zemansky's University Physics With Modern Physics*. ADDISON WESLEY Publishing Company Incorporated, 2010.

[81] R. Gonzalez and R. Woods, *Digital Image Processing*. Pearson/Prentice Hall, 2008.

[82] www.mathworld.wolfram.com, "Wolfram Mathworld." electronic.

[83] www.edmundoptics.com, "Edmund Optics Wolrdwide," Apr 2015.

[84] M. Naftaly and R. E. Miles, "Terahertz time-domain spectroscopy for material characterization," *Proceedings of the IEEE*, vol. 95, pp. 1658–1665, Aug 2007.

[85] J. Xu, K. W. Plaxco, and S. J. Allen, "Absorption spectra of liquid water and aqueous buffers between 0.3 and 3.72 THz," *The Journal of Chemical Physics*, vol. 124, no. 3, p. 036101, 2006.

Appendix A

Plasmonics Derivations and Principles

A.1 Derivations

To understand the unique properties of SPPs requires a more in-depth treatment of the physics behind them. The reader is referred to [55] and [41] for further detail. Deriving some of the characteristics of SPPs from first principles one can gain a greater understanding of what sets them apart from other electromagnetic waves. One can also learn why they interact with matter in the way that they do. All derivations will considered at interface between a metal film (ε_m) and air (ε_d).

A.1.1 Dispersion Relation

Maxwell's equations for a static charges are:

$$\vec{\nabla} \times \vec{E} = -\frac{1}{c}\frac{\partial \vec{B}}{\partial t} \tag{A.1}$$

$$\vec{\nabla} \times \vec{H} = J + \frac{\partial \vec{D}}{\partial t} \tag{A.2}$$

$$\vec{\nabla} \cdot \vec{D} = \rho \tag{A.3}$$

$$\vec{\nabla} \cdot \vec{B} = 0 \tag{A.4}$$

where $\vec{E}$ is the electric field density, $\vec{B}$ is the magnetic flux density, $\vec{H}$ is the magnetic field density, $\vec{D}$ is the electric flux density, $\vec{J}$ is the electric current density, c is the speed of light, and ρ is the charge density. In matter $\vec{E}$ and $\vec{B}$ are related to $\vec{D}$ and $\vec{H}$ as follows

$$\vec{D} = \varepsilon\vec{E} + \vec{P} \tag{A.5}$$

$$\vec{H} = \frac{1}{\mu}\vec{B} - \vec{M} \tag{A.6}$$

where $\vec{P}$ and $\vec{M}$ are the polarization and magnetization of the material in question and ε and μ are the electric and magnetic permeability of the material.

With reference to Figure 4.3 the electric, and magnetic, field is expressed as

$$\vec{E} = \vec{E}_0 e^{i(k_x x \pm k_z z - \omega t)} \tag{A.7}$$

with $+$ for z $\geq$ 0 (dielectric side) and $-$ for z $\leq$ 0 (metal side) then one can solve for the

dispersion relation of a SPP on a boundary between a metal and a dielectric. Since there is no current flowing through the metal J must equal zero and the metal is assumed have no external charge density and the material is non-magnetic, $\rho = \vec{M} = \vec{P} = 0$. Therefore,

$$\vec{\nabla} \times \vec{H} = \frac{\partial \vec{D}}{\partial t}$$

and

$$\vec{\nabla} \cdot \vec{D} = 0. \tag{A.8}$$

If one starts with the $\vec{H}$ field, then

$$\vec{\nabla} \times \vec{H} = -i\left(\frac{\omega}{c}\right)\varepsilon\vec{E} = -\left(\frac{\partial H_y}{\partial z}\right)\hat{x} + \left(\frac{\partial H_y}{\partial x}\right)\hat{z} \tag{A.9}$$

Looking at each direction of $\vec{H}$ separately gives

$$-\frac{\partial H_y}{\partial z} = -i\left(\frac{\omega}{c}\right)\varepsilon_d E_{x1} e^{i(k_{xd}x + k_{zd}z - \omega t)} \tag{A.10}$$

$$k_{zd} H_{yd} = \left(\frac{\omega}{c}\right)\varepsilon_d E_{xd} \tag{A.11}$$

and

$$\frac{\partial H_y}{\partial x} = -i\left(\frac{\omega}{c}\right)\varepsilon_d E_{zd} e^{i(k_{xd}x + k_{zd}z - \omega t)} \tag{A.12}$$

$$k_{zd} H_{yd} = \left(\frac{\omega}{c}\right)\varepsilon_d E_{zd} \tag{A.13}$$

where $k_{zd} = e^{i(k_{xd}x + k_{zd}z - \omega t)}$.

Similarly,

$$k_{zm} H_{ym} = -\left(\frac{\omega}{c}\right)\varepsilon_m E_{xm} \text{ and } k_{xm} H_{ym} = \left(\frac{\omega}{c}\right)\varepsilon_m x \tag{A.14}$$

is obtained for the other material.

If one assumes that $\mu = 1$ and $\rho = \sigma_s = 0$ together with the standard electromagnetic boundary conditions $E_{xd} = E_{xm}$, $H_{yd} = H_{ym}$, $\varepsilon_d E_{zd} = \varepsilon_m E_{zm}$, $k_{xd} = k_{xm} = k_x$, $(D_{d\perp} - D_{m\perp}) = \sigma_s$, $(B_{d\perp} - B_{m\perp}) = 0$, $(E_{d\parallel} - E_{m\parallel}) = 0$, and $(H_{d\parallel} - H_{m\parallel}) = K$, where K is the surface current density and σ_s is the charge density, then one can write these as follows [59]:

$$\frac{k_{zd}}{\varepsilon_d} H_{yd} + \frac{k_{zm}}{\varepsilon_m} H_{ym} = 0 \tag{A.15}$$

$$\frac{k_{zd}}{\varepsilon_d} = -\frac{k_{zm}}{\varepsilon_m}. \tag{A.16}$$

For the electric field

$$\vec{\nabla} \times \vec{E} = \left(\frac{\partial E_z}{\partial y}\right)\hat{x} + \left(\frac{\partial E_x}{\partial z} - \frac{\partial E_x}{\partial x}\right)\hat{y} - \left(\frac{\partial E_x}{\partial y}\right)\hat{z} \tag{A.17}$$

Considering the dielectric side, $z > 0$, gives

$$\frac{\partial E_{xd}}{\partial z} - \frac{\partial E_{zd}}{\partial x} = \frac{i\omega}{c} H_{yd} e^{i(k_{xd}x + k_{zd}z - \omega t)} \tag{A.18}$$

$$E_{xd} i k_{zd} + E_{zd} i k_{xd} = i \left(\frac{\omega}{c}\right) H_{yd} \tag{A.19}$$

$$E_{xd} = -E_{zd} \frac{k_{zd}}{k_{xd}} \tag{A.20}$$

Similarly, on the metal side, $z < 0$,

$$-E_{xm} i k_{zm} + E_{zm} i k_{xm} = i \left(\frac{\omega}{c}\right) H_{ym} \tag{A.21}$$

$$E_{xm} = E_{zm} \frac{k_{zm}}{k_{xm}} \tag{A.22}$$

Taking into account the boundary conditions $E_{xd} = E_{xm}$, $\varepsilon_d E_{zd} = \varepsilon_m E_{zm}$, and $k_{xd} = k_{xm} = k_x$, the Equations A.20 and A.22 can be equated to solve for k_x in this way.

$$k_x^2 = \varepsilon_d \left(\frac{\omega}{c}\right)^2 - k_{zd}^2 \tag{A.23}$$

$$k_x^2 = \varepsilon_m \left(\frac{\omega}{c}\right)^2 - k_{zm}^2 \tag{A.24}$$

Equating these two equations gives

$$\varepsilon_d \left(\frac{\omega}{c}\right)^2 - k_{zd}^2 = \varepsilon_m \left(\frac{\omega}{c}\right)^2 - \left(-k_{zd} \frac{\varepsilon_m}{\varepsilon_d}\right)^2 \tag{A.25}$$

from which one can solve for k_{zd}.

$$k_{zd}^2 = \left(\frac{\omega}{c}\right)^2 \left(\frac{\varepsilon_d - \varepsilon_m}{1 - (\frac{\varepsilon_m}{\varepsilon_d})^2}\right) \tag{A.26}$$

$$k_{zd}^2 = \left(\frac{\omega}{c}\right)^2 \left(\frac{\varepsilon_d^2}{\varepsilon_d + \varepsilon_m}\right) \tag{A.27}$$

Substituting into either equation A.23 or A.24 gives

$$k_x^2 = \varepsilon_d \left(\frac{\omega}{c}\right)^2 - \left(\frac{\omega}{c}\right)^2 \left(\frac{\varepsilon_d^2}{\varepsilon_d + \varepsilon_m}\right). \tag{A.28}$$

With some simplification this can be written as

$$k_x = \left(\frac{\omega}{c}\right) \sqrt{\frac{\varepsilon_d \varepsilon_m}{\varepsilon_d + \varepsilon_m}}. \tag{A.29}$$

Relabeling k_x so be k_{sp} and $\frac{\omega}{c}$ to be k_0 to gives the dispersion relation below.

$$k_{sp} = k_o \sqrt{\frac{\varepsilon_d \varepsilon_m}{\varepsilon_d + \varepsilon_m}} \tag{A.30}$$

where ε_d is the permittivity of the dielectric and ε_m is the permittivity of the metal. This relation can be illustrated through a dispersion curve, see Fig. 4.4.

From Figure 4.4 one can see that the SPPs will have a longer wavelength than light of the same frequency. This is the cause for the difference in the momentums of the two waves. It is this momentum difference that leads to the requirement of surface structures to bridge the gap between the incident light and the SPP.

A.1.2 Skin Depth

Skin depth is defined as the distance that an electro-magnetic wave can penetrate into the surface of a material before the intensity of the electric field falls to $\frac{1}{e}$ of the original. Mathematically this is defined as $\delta(\omega) = \frac{1}{Im(k_{zm})}$ which is frequency dependent. Our previous derivation of the dispersion relationship gives an equation describing k_{zm}

$$k_{zm} = \sqrt{\varepsilon_m \left(\frac{\omega}{c}\right) - k_x^2} \tag{A.31}$$

It is known that any value can be rewritten in terms of its real and imaginary components, like so

$$k_{zm} = Re(k_{zm}) + iIm(k_{zm}). \tag{A.32}$$

Also,at THz frequencies $\varepsilon_d << \varepsilon_{im}$ and $\varepsilon_{im} > |\varepsilon_{rm}|$. Using the dispersion relation, k_{zm} can be written

$$k_{zm} = \sqrt{\varepsilon_m \left(\frac{\omega}{c}\right)^2 - \left(\frac{\omega}{c}\right)^2 \left(\frac{\varepsilon_m \varepsilon_d}{\varepsilon_m + \varepsilon_d}\right)} \tag{A.33}$$

$$= \left(\frac{\omega}{c}\right) \sqrt{\frac{\varepsilon_m^2}{\varepsilon_m + \varepsilon_d}} \tag{A.34}$$

If $\varepsilon_m >> \varepsilon_d$, then

$$k_{zm} \simeq \left(\frac{\omega}{c}\right) \sqrt{\frac{\varepsilon_m^2}{\varepsilon_m + \varepsilon_d}} = \left(\frac{\omega}{c}\right) \sqrt{\varepsilon_m} \tag{A.35}$$

$$Re(k_{zm}) + iIm(k_{zm}) = \left(\frac{\omega}{c}\right) \sqrt{\varepsilon_{rm} + i\varepsilon im} \tag{A.36}$$

$$= \left(\frac{\omega}{c}\right) \sqrt{i\varepsilon_{im}} \sqrt{1 + \frac{\varepsilon_{rm}}{i\varepsilon_{im}}} \tag{A.37}$$

When $|\varepsilon_{rm}/i\varepsilon_{im}| << 1$ then this can be written as, using a Taylor expansion of $\sqrt{1+x}$,

$$k_{zm} = \left(\frac{\omega}{c}\right) \sqrt{i\varepsilon_{im}} \left(1 + \frac{\varepsilon_{rm}}{i\varepsilon_{im}}\right). \tag{A.38}$$

Using the definition

$$\sqrt{i} = \frac{1}{\sqrt{2}}(1+i) \tag{A.39}$$

one can rewrite this as

$$= \frac{1}{\sqrt{2}}(1+i)\left(\frac{\omega}{c}\right)\sqrt{\varepsilon_{im}}\left(1+\frac{\varepsilon_{rm}}{i2\varepsilon_{im}}\right) \tag{A.40}$$

This can then be written in the form $k_{zm} = Re(k_{zm}) + iIm(k_{zm})$

$$k_{zm} = \frac{1}{\sqrt{2}}\left(\frac{\omega}{c}\right)\sqrt{\varepsilon_{im}}\left(\left(1+\frac{\varepsilon_{rm}}{2\varepsilon_{im}}\right)+i\left(1-\frac{\varepsilon_{rm}}{2\varepsilon_{im}}\right)\right) \tag{A.41}$$

If $|\frac{\varepsilon_{rm}}{2\varepsilon im}| << 1$, then this can be simplified to be

$$= \frac{1}{\sqrt{2}}\left(\frac{\omega}{c}\right)\sqrt{\frac{\varepsilon_{im}}{2}} \tag{A.42}$$

Using the initial definition of the skin depth one can write δ in terms of ε_m

$$\delta = \left(\frac{c}{\omega}\right)\sqrt{\frac{2}{\varepsilon_{im}}} \tag{A.43}$$

Figure 4.5a shows how the skin depth changes depending on which side of the interface the wave is penetrating and how it decays within that material.

A.1.3 Propagation Length

Propagation length is defined as the distance that a surface wave can travel along an interface before it is damped out due to interaction with the material it travels through and is shown as

$$L_x = \frac{1}{2k_x''} \tag{A.44}$$

where k_x is defined as the dispersion relation (1 means dielectric and 2 means metal) and can be written

$$k_x = \left(\frac{\omega}{c}\right)\sqrt{\frac{\varepsilon_d\varepsilon_m}{\varepsilon_d+\varepsilon_m}} = k_x' + ik_x'' \tag{A.45}$$

If $\varepsilon_d = \varepsilon_d' + i\varepsilon_d''$ then the argument of the square root can be manipulated into a useful form, as follows

$$\frac{\varepsilon_d\varepsilon_m}{\varepsilon_d+\varepsilon_m} = \frac{(\varepsilon_d'+i\varepsilon_d'')\varepsilon_m}{\varepsilon_d+\varepsilon_m} \tag{A.46}$$

$$= \varepsilon_m\frac{(\varepsilon_d'^2+\varepsilon_d'\varepsilon_m+\varepsilon_d''^2+i\varepsilon_d''\varepsilon_m)}{(\varepsilon_d'+\varepsilon_m)^2+\varepsilon_d''^2} \tag{A.47}$$

When $\varepsilon_m << \varepsilon_d$

$$\simeq \varepsilon_m \left(\frac{\varepsilon_d^{'2} + \varepsilon_d^{''2} + i\varepsilon_d^{''}\varepsilon_m}{\varepsilon_d^{'2} + \varepsilon_d^{''2}} \right) \tag{A.48}$$

and $\varepsilon_d^{''} > |\varepsilon_d^{'}$

$$\simeq \varepsilon_m \left(\frac{\varepsilon_d^{''2} + \varepsilon_d^{''}\varepsilon_m}{\varepsilon_d^{''2}} \right) = \varepsilon_m \left(1 + i\frac{\varepsilon_m}{\varepsilon_d^{''}} \right) \tag{A.49}$$

$$\left(\frac{\varepsilon_d \varepsilon_m}{\varepsilon_d + \varepsilon_m} \right) = \sqrt{\varepsilon_m \left(1 + i\frac{\varepsilon_m}{\varepsilon_d^{''}} \right)} \tag{A.50}$$

Again, when $|\varepsilon_{rm}/i\varepsilon_{im}| << 1$ then a Taylor expansion in the form of $\sqrt{1+x}$ can be used to give

$$\simeq \sqrt{\varepsilon_m} \left(1 + i\frac{\varepsilon_m}{2\varepsilon_d^{''}} \right) = \sqrt{\varepsilon_m} + \frac{i\varepsilon_m^{3/2}}{2\varepsilon_d^{''}} \tag{A.51}$$

$$k_x = k_x^{'} + ik_x^{''} = \left(\frac{\omega}{c} \right) \sqrt{\frac{\varepsilon_d \varepsilon_m}{\varepsilon_d + \varepsilon_m}} = \left(\frac{\omega}{c} \right) \left(\sqrt{\varepsilon_m} + \frac{i\varepsilon_m^{3/2}}{2\varepsilon_d^{''}} \right) \tag{A.52}$$

From equation A.44

$$L_x = \frac{1}{2k_x^{''}} = \left(\frac{c}{\omega} \right) \left(\frac{\varepsilon_m^{'} + \varepsilon_d}{\varepsilon_m^{'}\varepsilon_d} \right)^{\frac{3}{2}} \left(\frac{\varepsilon_m^{'}}{\varepsilon_m^{''}} \right)^2 = \left(\frac{c}{\omega} \right) \frac{\varepsilon_d^{''}}{\varepsilon_m^{3/2}} \tag{A.53}$$

For most metals, the propagation length is very large since the properties of the metal approach those of a perfect electrical conductor.

A.2 Conservation of Momentum

As a result of the coupling of an electro-magnetic wave, with momentum $\hbar k_o$, with the surface electrons of a metal the SPP has a different momentum, $\hbar k_{sp}$. The SPP has a different momentum which is related to the electromagnetic wave's original momentum by the dispersion relation equation A.30. This momentum difference, $\hbar k_{sp} \neq \hbar k_0$, must be bridged before a SP can be created on metal-dielectric interface.

As is seen in Figure 4.4 the SPP lies on the larger wave vector side of the light line ($k = \frac{\omega}{c}$) meaning that they have a larger wave vector than that of free electromagnetic waves. As a result SPPs are not created on a surface without specific conditions being present to provide the necessary matching term to conserve momentum. These conditions are essential to allow the coupling of electromagnetic waves with surface plasmons to form SPPs.

There are several main ways that this difference in the momentum of the electromagnetic wave and SPP can be bridged to allow a SPP to be formed. The most common way to provide this matching term for the momentum is to use a Bragg grating.

A.2.1 Grating Coupling

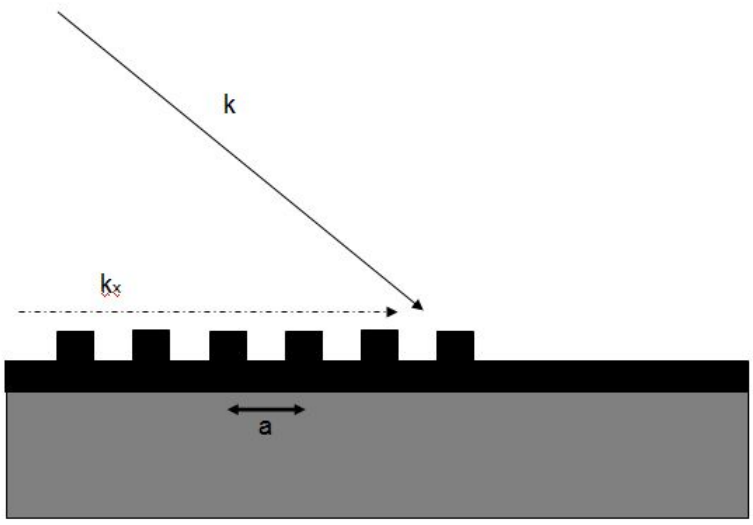

Figure A.1: Diagram of the light wave vectors involved in coupling by means of a Bragg grating.

In the method of grating coupling a metal grating of the correct grating constant is employed to bridge the difference in wave vectors. If radiation of wave vector $k = \frac{\omega}{c}$ incident on a grating with grating constant a, at an angle θ_0, then the component of the incident wave vector on the surface can have wave vector

$$k_{x_{light}} = \frac{\omega}{c} sin\theta_0 \pm nG \tag{A.54}$$

where, n is an integer, and $G = \frac{2\pi}{a}$ is the grating momentum. SPPs can only be formed when $k_{x_{light}}$ equals the surface plasmon wave vector.

$$k_{x_{light}} = \frac{\omega}{c} sin\theta_0 \pm nG = \frac{\omega}{c}\sqrt{\frac{\varepsilon_m}{1+\varepsilon_m}} = k_{sp} \tag{A.55}$$

This shows that by choosing the grating correctly then a situation in which SPPs can be formed can be created.

A.2.2 Periodic Corrugations

Extending the 1-D problem, grating coupling, into two dimensions to deal with a real two dimensional wave front one can use periodic surface structures to allow for scattering of THz radiation that is normally incident to the surface. This scattering by the surface provides the ”pseudo-momentum” [48] required to overcome the difference in momenta. These periodic corrugations act like a Bragg grating to allow for coupling, though coupling can take place even when only one concentric ring is present around an aperture. One of

the most simple implementations of these periodic surface structures is called a bullseye lens. This type of lens consists of a single aperture surrounded by periodic circular grooves which can vary in depth width and period. Changing any of these parameters allows for tuning of the lens' unique properties, such as the wavelength of light which can couple to create SPPs and the phase of the resulting transmitted beam.

Grooves on the side that the light is incident on, the input side, provide the momentum matching properties required to form SPPs. With a plane wave incident on the bullseye lens, all the parameters must be chosen such that all the excited SPPs are in phase to prevent destructive interference with other SPPs excited at other rings. Constructive interference of the SPPs excited at each ring on the lens give an n^2 response from the surface, which means that if there are 3 rings than there is 9 times greater throughput of light possible. This "encourag[es] [a] build-up of signal at a wavelength corresponding to the grating period" [48]. Without any other structures the wave transmitted from the output side will then radiate spherically from the lens, as shown in Figure 4.1.

Periodic grooves on the output side of the metal lens allow the transmitted light to be focused into a more confined beam that lasts for up to several wavelengths. Interaction of the SPPs on the output side with the radiation field and it is the interference from the different rings that give a maximum intensity in a preferred direction. This interaction confines the output radiation making the useful light more intense for imaging purposes.

Appendix B

TeraHerz Source and Detector

Virginia Diodes, Inc.

USER GUIDE

320-330GHz Tx

1 Product Overview

Product List (Quantity)	Serial Number(s)	Order No.	Date / Initials
320-330GHz Transmitter	VDI Tx 148	09comp42	07/31/2009 JTD
		RCR112014ULB	01/05/2015 PJD

Product Description: This VDI product includes one 320-330GHz Transmitter (Tx). This product was returned under RMA# RCR112014ULB for repair of the final two doubler stages, 154R2X2 and D320.

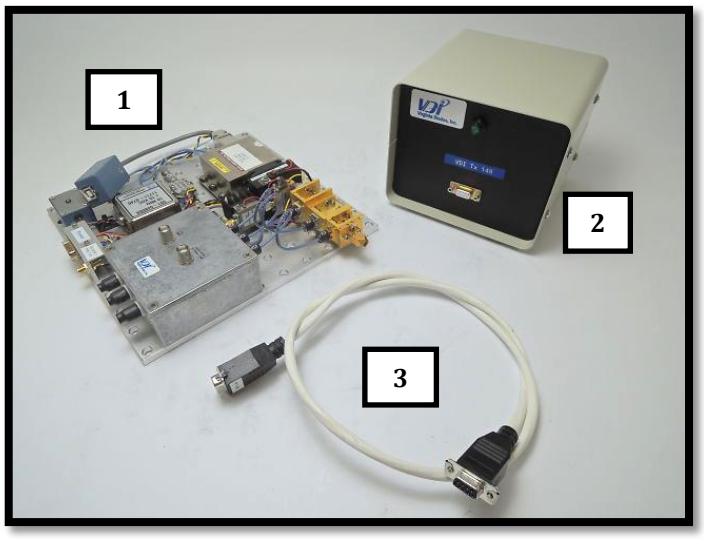

No.	Part Description
1	VDI Tx 148
2	VDI Custom Power Supply
3	DC Power Cable
4	AC Power Cable*
5	USB Cable*
6	Synthesizer Software CD*

**Remained with customer during repair.*

Figure 1: Product photograph and listing is shown.

2 Warning and Caution Statements

WARNING AND CAUTION STATEMENTS	
WARNING	This product can be permanently damaged by Electrostatic Discharge (ESD). It is recommended that engineers and technicians wear a special grounded wrist strap when handling this component. In addition, the work environment around the component should be well grounded.
WARNING	Opening the blocks, parts, or components will damage the internal components. VDI is not responsible for the warranty or guaranty of products damaged as a result of improper handling, testing, biasing, or use by customer.
CAUTION	VDI assumes the customer is familiar with microwave, millimeter wave, and VDI products. The user and customer are expected to understand all safety guidelines, health hazards, and general advisories that may exist and are associated with the use of this device. VDI is not responsible for any human hazards that may exist or may occur while using this device.

3 Product Specifications

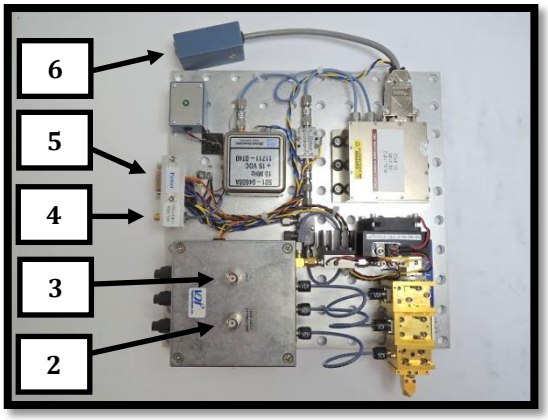

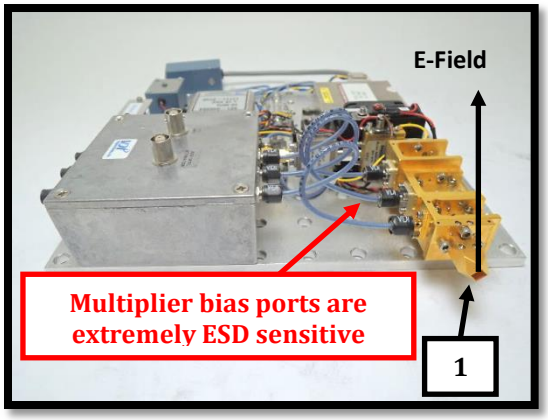

Description		Specification	Connector
RF Output [1]	Frequency Range	320-330GHz	WR2.8 Diagonal Horn
	Output Power (Minimum)	10mW*	
Frequency Monitor [2]	Frequency Range	10.00-10.31GHz	SMA(f)
	Multiplication Factor	32	
DC Input [3]	Compatible with VDI Custom Power Supply	-	9-PIN DSUB
Amplitude Modulation [4]	TTL/AM Input	0-5V, up to ~15kHz	BNC(f)
RF Attenuation [5]	User Controlled Attenuation	0V (full power), 5V (off)	BNC(f)
USB Synthesizer Control [6]	For use with user computer**	-	USB Type B

**See Section 5 for actual system performance.*

***Synthesizer software installation required.*

Figure 2: General product specifications are shown for the VDI Tx 148.

4 General Operating Procedures and Guidelines

VDI assumes the customer is familiar with VDI products, and VDI is not responsible for the warranty or guaranty of products damaged as a result of improper handling, testing, biasing, or use by customer. VDI offers the following general guidelines for using these products and recommends the customer contact VDI at (434) 297-3257 for assistance if needed. The following procedures are a quick guide for turning on and off the product. In each case the individual steps must be followed in the proper sequence to avoid damaging critical components.

4.1 Required Operating Procedures

- DO NOT exceed damage limits listed in Figure 2.
- DO NOT apply any external biases to the system.
- DO NOT tamper with black bias cables. Multiplier bias connections are extremely ESD sensitive.
- DO NOT reflect more than 10% of the output power into the RF output port.

Failure to follow these procedures will damage or destroy the device.

4.2 Additional Guidelines, Limitations, and Recommendations

- The Tx is shipped with waveguide tape attached. Remove before operation.
- Install VDI Synthesizer Control software on computer terminal before connecting the USB Synthesizer Control port to the computer terminal. The software CD was included with the original shipment.

4.3 Synthesizer Control Software Installation

1. DO NOT connect the synthesizer to the computer terminal prior to installing the software.
2. Insert the CD provided with the original shipment. The CD should auto-run *CDM 2.04.06.exe*. If not, run *CDM 2.04.06.exe*.
3. Connect the source to the computer using a USB cable.
4. Follow Section 4.4 to turn on the VDI Tx.
5. Run *Set synthesizer.exe* from *Synthesizer.llb* on the software CD.
6. Enter the serial number (FTDYM3GB) into the “Serial Number” field.

4.4 Turn-On Procedure

1. The user and test bench must be properly grounded and protected against ESD.
2. With the VDI Custom Power Supply turned off, make all necessary connections (i.e. USB cable, AC cable, DC cable).
3. Turn on the VDI Custom Power Supply, set synthesizer frequency and monitor the RF output.
    a. For Amplitude Modulation: use TTL Mod. port (0-5V, up to 15kHz)
    b. For RF Attenuation: use UCA port (0V = no attenuation, 5V = full attenuation) – See Figure 4.

4.4 Turn-Off Procedure

1. The user and test bench must be properly grounded and protected against ESD.
2. Turn off the VDI Custom Power Supply.
3. After completing turn-off procedures described above, it is now safe to turn off all other equipment on user test bench.

Contact VDI with questions or concerns regarding operational procedures and limitations.

5 Product Performance

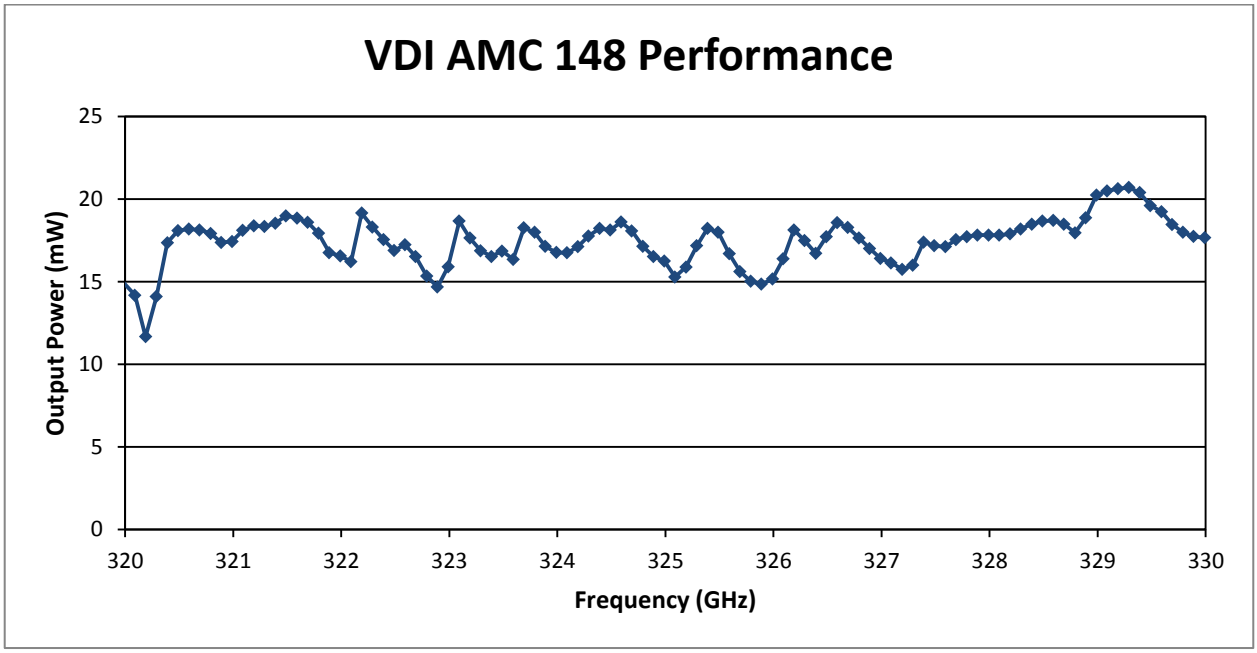

Figure 3: The product performance (maximum output power versus output frequency) is shown for VDI Tx 148. Power measurements were made using an Erickson Power Meter.

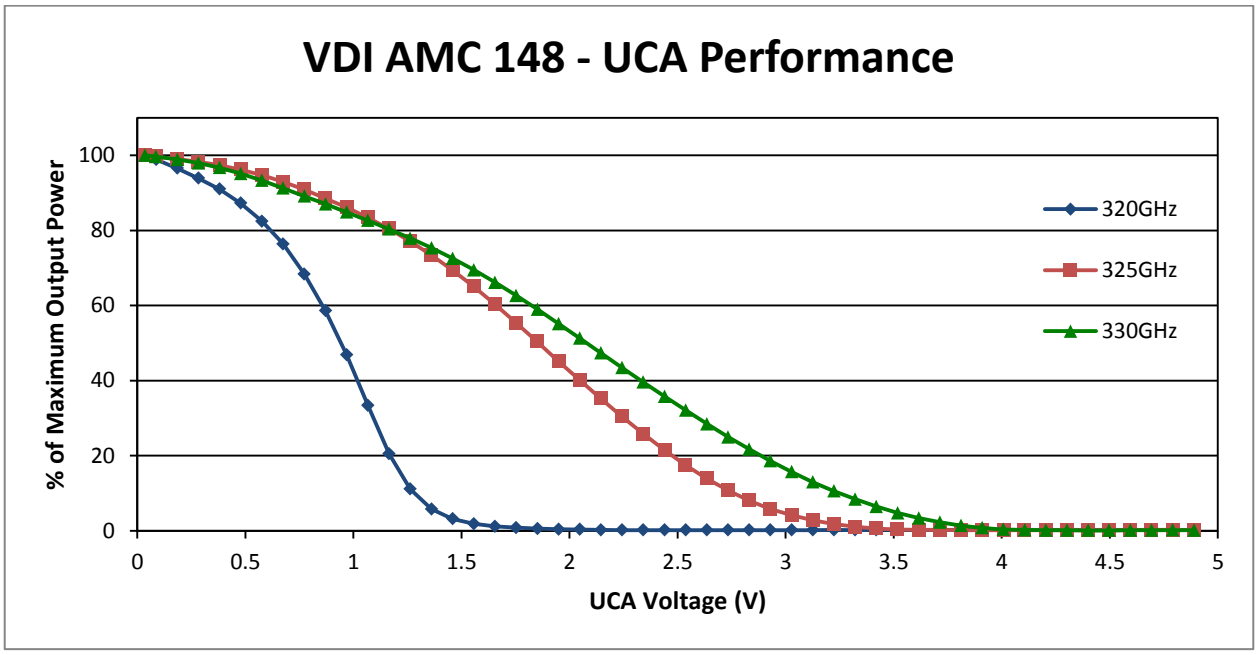

Figure 4: The product performance (output power versus user controlled attenuation input voltage) is shown for VDI Tx 148.

Note: The UCA voltage reduces the amplifier output power. The data presented in this graph was measured by VDI under specific test conditions and is meant as a guide. The exact shape of the curves will vary significantly depending on the measurement conditions, including operating temperature, modulation rate, duty cycle, and load impedance. Also, for large attenuation values the multipliers can become under-pumped and may generate undesired harmonics at increased levels.

6 End of Document

VDI USER GUIDE

Product: WR2.8 Zero Bias Detector with Internal ESD Protection
Serial Numbers: WR2.8R4 1-27; WR2.8H (25) Diagonal Horn 5-20
Virginia Diodes Inc., (434) 297-3257
060712-12133-UNIV LETHBRIDGE-VDI2.8ZBD AND HORN-2
8/21/2012 JHP

Section 1 User Guide Overview

The customer must read the entire user guide prior to handling, testing, biasing, or using this product. This document gives a general description of the product, several important warnings to be considered when using the product, and basic operating instructions. This VDI product includes one WR2.8R4 zero bias detector with internal ESD protection and attached WR2.8 diagonal horn.

Warning: Read the entire VDI user guide for this product prior to operation.

Warning: This product can be permanently damaged by ElectroStatic Discharge (ESD). It is recommended that engineers and technicians wear a special grounded wrist strap when handling this component. In addition, the work environment around the component should be well grounded.

Warning: Opening the blocks, parts, or components will damage the internal components. VDI is not responsible for the warranty or guaranty of products damaged as a result of improper handling, testing, biasing, or use by customer.

Caution: VDI assumes the customer is familiar with microwave, millimeter wave, and VDI products. The user and customer are expected to understand all safety guidelines, health hazards, and general advisories that may exist and are associated with the use of this device. VDI is not responsible for any human hazards that may exist or may occur while using this device.

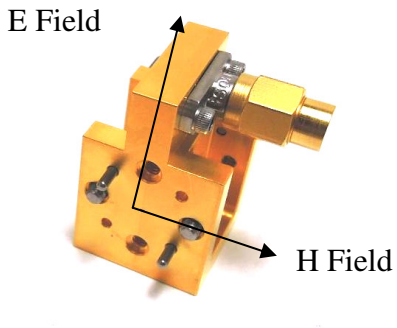

Figure 1: Photograph of a similar WR2.8 zero bias detector is shown (horn not shown).

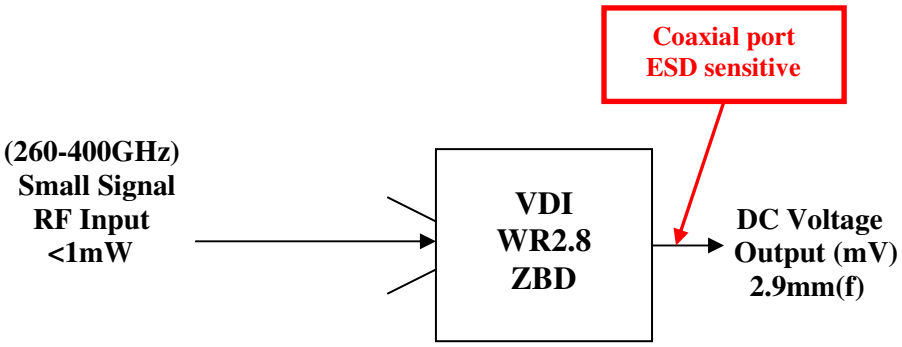

Figure 2: Diagram of the product is shown.

Section 2 General Operating Procedures and Guidelines

VDI assumes the customer is familiar with VDI products, and VDI is not responsible for the warranty or guaranty of products damaged as a result of improper handling, testing, biasing, or use by customer. VDI offers the following general guidelines for using these products and recommends the customer contact VDI at (434) 297-3257 for assistance if needed. The following procedures are a quick guide for turning on and off the product. In each case the individual steps must be followed in the proper sequence to avoid damaging critical components.

Warning: RF drive limitations, voltage bias limitations, and current limitations may exist for this device and are described below. Exceeding these limitations and guidelines may cause permanent damage to the device.

The drive and bias guidelines, limitations, and recommendations for this product are:

- RF input power maximum for safe operation is 1mW. Exceeding 1mW will destroy the device.
- The VDI ZBD does not require bias. DO NOT attempt to bias device.
- The internal ESD protection circuit limits the detector response to ~500kHz into a high impedance load.

- The user is liable for repair costs of detectors damaged by ESD, and the use of stringent ESD precautions is recommended when making connections to the detectors.
- Remove waveguide tape prior to operation.

Contact VDI with questions or concerns regarding the product RF drive limitations, voltage bias limitations, and current limitations.

The following procedure is to be used when turning on the device.

Step A: The user and test bench must be properly grounded and protected against ESD.

Step B: With RF input power off, connect the device to the user system. The detector mV output is monitored from the coaxial port of the detector using a floating voltmeter.

Step C: Turn on the small signal RF input power (<1mW) to the device and monitor the detector output using a floating volt meter. (The linear region for responsivity is 0-10uW).

The following procedure is to be used when turning off the device.

Step A: The user and test bench must be properly grounded and protected against ESD.

Step B: Turn off the RF input power.

Step C: If needed, disconnect the voltmeter from the detector. When detector is not in use, be sure to reconnect the 50Ohm cap provided.

Step D: After completing turn-off procedures described above, it is now safe to turn off any other equipment on the test bench.

Section 3 Product Performance and Guidelines

The product performance is shown below.

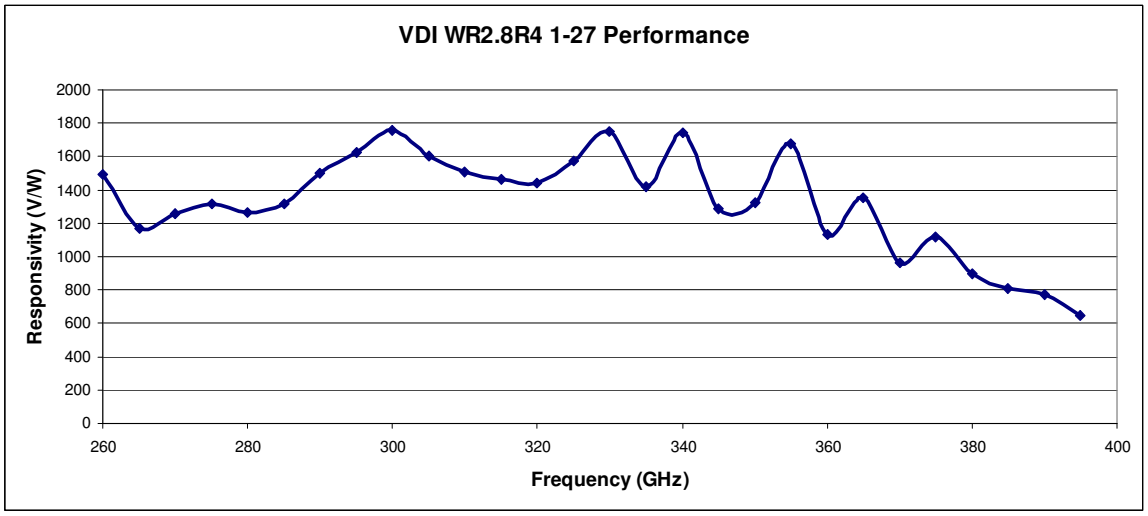

Figure 3: The WR2.8R4 ZBD performance (responsivity in V/W vs. RF input frequency for ~1-10uW RF input power) is shown.

Section 4 End of Document

VDI is not responsible for the warranty or guaranty of products damaged as a result of improper handling, testing, biasing, or use by customer.